Stability analysis and control design of spatially developing flows

by

Shervin Bagheri

May 2008
Technical Reports from
Royal Institute of Technology
Department of Mechanics
SE-100 44 Stockholm, Sweden

Akademisk avhandling som med tillstånd av Kungliga Tekniska Högskolan i Stockholm framlägges till offentlig granskning för avläggande av teknologie licentiatexamen torsdagen den 05 juni 2008 kl 14.00 i D41, Kungliga Tekniska Högskolan, Lindstedtsvägen 17, 1tr, Stockholm.

Universitetsservice US–AB, Stockholm 2008

Stability analysis and control design of spatially developing flows

Shervin Bagheri
Linné Flow Centre, Department of Mechanics, Royal Institute of Technology (KTH)
SE-100 44 Stockholm, Sweden

Abstract

Methods in hydrodynamic stability, systems and control theory are applied to spatially developing flows, where the flow is not required to vary slowly in the streamwise direction. A substantial part of the thesis presents a theoretical framework for the stability analysis, input-output behavior, model reduction and control design for fluid dynamical systems using examples on the linear complex Ginzburg-Landau equation. The framework is then applied to high-dimensional systems arising from the discretized Navier–Stokes equations. In particular, global stability analysis of the three-dimensional jet in cross flow and control design of two-dimensional disturbances in the flat-plate boundary layer are performed. Finally, a parametric study of the passive control of two-dimensional disturbances in a flat-plate boundary layer using streamwise streaks is presented.

Descriptors: Global modes, transient growth, model reduction, feedback control, streaks, Tollmien–Schlichting waves

Preface

This thesis considers the stability and control of spatially developing flows. In the first part a short review of the basic concepts and methods is presented. The second part consists of the following papers:

Paper 1. Bagheri S., Hœpffner J., Schmid P.J. and Henningson D.S., 2008
"Input-output analysis and control design applied to a linear model of spatially developing flows", Accepted for publication in Applied Mechanics Reviews

Paper 2. Bagheri S., Brandt L. and Henningson D.S., 2008
"Input-output analysis, model reduction and control design of the flat-plate boundary layer", Submitted to the Journal of Fluid Mechanics

Paper 3. Bagheri S., Schlatter P. and Henningson D.S., 2008
"The three-dimensional global stability of the jet in crossflow", Internal report

Paper 4. Bagheri S. and Hanifi A., 2007
"The stabilizing effect of streaks on TS-waves: A parametric study", Published in Physics of Fluids, **19**, 078103

Division of work between authors

The research project was initiated by Prof. Dan Henningson (DH) who also acted as supervisor. Co-advisors were Dr. Luca Brandt (LB) and Dr. Philipp Schlatter (PS). Collaborates were Prof. Peter Schmid (PJS), Dr. Ardeshir Hanifi (AH) and Dr. Jérôme Hœpffner (JH).

Paper 1
The code development and calculations were done by SB with feedback from JH. Most of the paper was written by SB with input from PJS, JH and DH. JH wrote the "Stochastic forcing" section, PS wrote parts of the "Input-output behavior" section and the introduction was written by PJS and DH.

Paper 2
The control and model reduction algorithms were implemented by SB with feedback from LB. The computations were done by SB. The mathematical formulation in the paper was done by SB and DH. The paper was written by SB and LB with input from DH.

Paper 3
The eigenvalue solver and the jet in crossflow were implemented by SB with feedback from PS. The simulations were done by SB. The paper was written by SB and PS with input from DH.

Paper 4
The streaks were implemented by SB in a code developed at FOI with feedback from AH. The parametric studies were done by SB. The paper was written by SB and AH.

Contents

Part I

Introduction

CHAPTER 1

Introduction

The combined efforts of scientists and engineers in fluid mechanics have strongly contributed to milestones in technological developments. However, some of these technological successes, such as airplanes and spacecrafts, are also contributing to global warming and the draining of earth's limited resources. For example, the worldwide shipping consumes about 2.1 billion barrels of oil per year (Corbett & Koehler 2003) whereas the airline industry consumes about 1.5 billion barrels per year (Kim & Bewley 2007).

If the existing technological solutions can be improved, it can help to reduce the world's oil consumption and preserve the earth's resources. Engineers have used the physical principles of fluid mechanics, established by scientists in last two centuries, to increase the efficiency of their applications. At the same time a mathematically well-established field, systems and control theory, has emerged which given a set of constraints and an objective, it provides the "best solution". The incorporation of systematic methods from systems and control theory in fluid mechanics can make a significant difference in efficiency of various applications.

However, the complexity of the governing equations of fluid mechanics have until recently hindered the use of many of these methods on a full scale in applications. The Navier–Stokes equations consist of a four-dimensional nonlinear partial differential equation (PDE). Since there exist analytical solutions only for a few flow configurations, these equations are approximated numerically giving rise to well above one million ordinary differential equations. In systems and control theory the most elegant results require the solution of various matrix equations, such as the Riccati or Lyapunov equations. Even with the use of supercomputers it is prohibitively expensive to solve these equations for large systems.

The present thesis is part of a long-term project with the aim of applying stability, systems and control theoretical tools to systems of very large dimension arising from various fluid dynamical situations. The most fundamental tool is a Navier-Stokes solver, which given a flow field at certain time, the solver provides a field at a later time.

CHAPTER 2

Theoretical background

2.1. Hydrodynamic stability theory

The incompressible Navier–Stokes equations given by

$$\frac{\partial \boldsymbol{u}}{\partial t} + (\boldsymbol{u}\cdot\nabla)\boldsymbol{u} = -\nabla p + \frac{1}{\mathrm{Re}}\nabla^2\boldsymbol{u}, \tag{2.1a}$$

$$\nabla\cdot\boldsymbol{u} = 0, \tag{2.1b}$$

$$\boldsymbol{u}(\mathbf{x},0) = \boldsymbol{u}_0, \tag{2.1c}$$

govern the evolution of the flow field $\boldsymbol{u}(\mathbf{x},t) = [u,v,w]^T$ and pressure field $p(\mathbf{x},t)$ in space $\mathbf{x} = (x,y,z)$ and time t. The equations are non-dimensionalized with the characteristic velocity scale U, the length scale L and the kinematic viscosity ν. The Reynolds number is defined as $\mathrm{Re} = UL/\nu$.

In general, hydrodynamic stability theory is concerned with characterizing the behavior of infinitesimal disturbances $\boldsymbol{u}'$ to a base flow $\mathbf{U}$, which is a steady solution to Navier–Stokes equations (2.1). The governing equations of these disturbances are found by inserting $\boldsymbol{u} = \mathbf{U} + \epsilon\boldsymbol{u}'$ and $p = P + \epsilon p'$, where p' is the pressure perturbations, into (2.1) and neglecting the terms of order ϵ^2. The resulting linearized Navier–Stokes equations are,

$$\frac{\partial \boldsymbol{u}}{\partial t} + (\mathbf{U}\cdot\nabla)\boldsymbol{u} + (\boldsymbol{u}\cdot\nabla)\mathbf{U} = -\nabla p + \frac{1}{\mathrm{Re}}\nabla^2\boldsymbol{u}, \tag{2.2a}$$

$$\nabla\cdot\boldsymbol{u} = 0, \tag{2.2b}$$

$$\boldsymbol{u}(\mathbf{x},0) = \boldsymbol{u}_0, \tag{2.2c}$$

where the superscript $'$ of the disturbance fields has been omitted. The base flow in our case is a steady solution to (2.1), but it can also be a time-periodic solution or a time-averaged turbulent flow. To solve equations (2.1) and (2.2) various boundary conditions depending the physical domain can be imposed.

If the PDE (2.2) is discretized in space and projected on a divergence-free subspace it can be approximated by the initial-value problem

$$\frac{\partial \boldsymbol{u}}{\partial t} = A\boldsymbol{u} \tag{2.3a}$$

$$\boldsymbol{u}(0) = \boldsymbol{u}_0, \tag{2.3b}$$

where $\boldsymbol{u}(t)$ now denotes the state vector, compromising the divergence-free amplitude functions of the perturbations. The discretized and linearized Navier-Stokes equations including boundary conditions are represented by the action

of the matrix A on $\boldsymbol{u}$. The solution to (2.3) is given by

$$\boldsymbol{u}(t) = e^{At}\boldsymbol{u}_0. \tag{2.4}$$

The matrix exponential is the key to stability analysis and also to input-output analysis and control design discussed in subsequent sections. However, this function also poses the greatest computational challenge due its dimension. The dimension of the linearized operator depends on the number of non-homogeneous spatial directions of the base flow. In table 2.1 we list the base flows studied in this thesis. They are all spatially developing, *i.e.* the direction which the disturbances travel in is inhomogeneous. We observe that the dimension of A for flows with two or more inhomogeneous directions becomes prohibitively large to allow for an evaluation of the exponential matrix.

Except for one-dimensional base flows the exponential matrix must be approximated. The most common methods (Molder & Van Loan 2003) require that all elements of the matrix can be stored in memory. For fluid systems this requirement cannot always be met. Instead, the recognition that the action of e^{At} simply represents integrating the Navier-Stokes equations in time, the exponential matrix can be approximated with a direct numerical simulation (DNS) code, also referred to as a time-stepper. In what follows the reader should equate $e^{A(t+T)}\boldsymbol{u}(t)$ with a DNS simulation starting with an initial condition $\boldsymbol{u}(t)$ and providing $\boldsymbol{u}(t+T)$. In this so called "timestepper approach", matrices are never stored and storage demands in memory are of the same order as a small number of flow fields.

As time tends to infinity the disturbance approaches the least stable eigenmodes, ϕ_i, of A,

$$A\phi_i = \lambda_i\phi_i. \tag{2.5}$$

Even with iterative methods it is in general not possible to explicitly solve the above eigenvalue problem, since A cannot be stored in memory. Instead we make use of our DNS code and a time-stepper technique (Barkley *et al.* 2002) by noting that the eigenmodes are invariant under the transformation e^{At} (for fixed time t),

$$e^{At}\phi_i = \sigma_i\phi_i, \qquad |\sigma_1| > \cdots > |\sigma_n|. \tag{2.6}$$

The asymptotic stability of disturbances as $t \to \infty$ is determined by the largest magnitude of σ_1,

$$|\sigma_1| > 1 \qquad \text{asymptotically unstable,} \tag{2.7a}$$

$$|\sigma_1| \leq 1 \qquad \text{asymptotically stable.} \tag{2.7b}$$

The eigenvalues of A can be recovered from $\lambda_i = \log(\sigma_i)/t$ in order to obtain the growth rate and frequency of the associated eigenmode ϕ_i.

For many open shear flows where fluid is continuously entering and leaving the physical domain the matrix A is non-normal (Trefethen & Embree 2005)

	Base Flow	Inhomogeneous direction(s)	Dimension of $\boldsymbol{u}(t)$	Storage of A
Ginzburg-Landau	$\boldsymbol{U}(x)$	1D	10^2	1 MB
Blasius	$\boldsymbol{U}(x,y)$	2D	10^5	25 GB
Jet in crossflow	$\boldsymbol{U}(x,y,z)$	3D	10^7	500 TB

TABLE 2.1. Spatially developing flows investigated in this thesis.

($AA^* \neq A^*A$). Here, the superscript * denotes the complex-conjugate operation[1]. As a consequence, the disturbance can experience large transient energy growth, although all eigenvalues λ_i have negative real parts. The amplification of the initial disturbance $\boldsymbol{u}_0$ is then given by,

$$G(t) = \|e^{At}\boldsymbol{u}_0\|^2. \tag{2.8}$$

In particular, if there is an initial condition (with unit norm) that results in the *maximum* energy amplification, this function ϕ_i^o is an eigenmode of $e^{A^*t}e^{At}$ corresponding to the largest eigenvalue of

$$e^{A^*t}e^{At}\phi_i^o = \sigma_i^o\phi_i^o, \qquad \sigma_1^o \geq \cdots \geq \sigma_n^o \geq 0. \tag{2.9}$$

The condition for a short-time energy amplification becomes

$$\sigma_1^o > 1 \qquad \text{transient growth,} \tag{2.10a}$$

$$\sigma_1^o \leq 1 \qquad \text{no transient growth.} \tag{2.10b}$$

The matrix exponential e^{A^*t} is approximated by solving the adjoint Navier-Stokes equations numerically using an adjoint time-stepper.

The most common approach to modern linear stability theory is the quest for eigenmodes of A and A^*A, referred to as global modes and optimal disturbances respectively. The calculation of these eigenmodes is computationally tractable for very large systems using time-steppers (Barkley *et al.* 2002) in combination with Krylov subspace methods. In Paper 3 the global eigenmodes of jet in crossflow are computed using the Arnoldi method (Trefethen & Bau 1997). In Paper 4 optimal disturbances for the Blasius boundary layer are computed using power iterations (Andersson *et al.* 1999).

2.2. Linear systems theory

Under realistic conditions the flow system is continuously forced with external disturbances and entire instantaneous velocity fields are not available for analysis. The natural extension to the previous section is to include inputs and outputs,

$$\begin{aligned} \dot{\boldsymbol{u}} &= A\boldsymbol{u} + Bw, \\ z &= C\boldsymbol{u}. \end{aligned} \tag{2.11}$$

[1]We assume for simplicity that the norm is defined as $\|\boldsymbol{u}\|^2 = \boldsymbol{u}^*\boldsymbol{u}$. See Paper 1 and 2 for other definitions.

The column vector B and the row vector C govern the type and location of the input $w(t)$ and output $z(t)$, respectively. In the context of aerodynamic flows, the input can represent the effects of free-stream turbulence, wall roughness or impingement acoustic waves and the output can represent measurements of pressure or friction at the boundaries of the flow domain.

For a stable system the equations (2.11) have the formal solution

$$z(t) = C \int_0^t e^{A(t-\tau)} B w(\tau)\ d\tau \tag{2.12}$$

where $\boldsymbol{u}_0 = 0$. For input-output analysis it is useful to define a mapping from past inputs to future outputs,

$$(Hw)(t) = C \int_0^\infty e^{A(t+\tau)} B w(\tau)\ d\tau. \tag{2.13}$$

Notice that if the input $u(t) = w(-t)$ for $t < 0$ then the output for $t \to \infty$ will be $z(t) = (Hw)(t)$ (Glover 1999).

Linear systems theory is concerned with the response behavior of the output signal to various input signals. The amplification of the output signal at a certain time is given by $\|Hw\|^2$. In particular, the largest output response is given by the input w_i corresponding to the largest eigenvalue of H^*H,

$$H^*Hw_i = (\sigma_i^b)^2 w_i, \qquad \sigma_1^b \geq \ldots \sigma_n^b \geq 0 \tag{2.14}$$

where σ_i^b are called the Hankel singular values. For an input with unit norm the Hankel singular value gives a measure of how much the output is amplified,

$$\sigma_1^b > 1 \qquad \text{output amplification,} \tag{2.15a}$$

$$\sigma_1^b \leq 1 \qquad \text{no output amplification.} \tag{2.15b}$$

One can associate a sequence of modes, referred to as balanced modes with the sequence of inputs w_i,

$$\phi_i^b = \int_0^\infty e^{At} B w_i. \tag{2.16}$$

If a particular balanced mode ϕ_i^b has an associated Hankel singular value which is zero, $\sigma_i = 0$, this mode does not influence the input-output behavior. This has led to an efficient method of model reduction where the input-output behavior is preserved, called balanced truncation (Moore 1981). Balanced truncation is based on the idea of reducing the dimensions of the original system by removing the redundant states – *i.e.* balanced modes corresponding to $\sigma_i^b = 0$ – and also, in addition, removing the states that have a very weak influence on the input-output behavior, *i.e.* ϕ_i^b corresponding to $\sigma_i^b \ll 1$.

In Paper 1 and Paper 2 a time-stepper approach (Rowley 2005) is used to compute the balanced modes for the Ginzburg-Landau equation and the Blasius boundary layer. It is shown that a few balanced modes can preserve the input-output behavior of the original high-dimensional system.

2.3. Linear control theory

The next step after the analysis of the amplification behavior of a linear system to initial conditions and external excitations is to manipulate the inherent dynamics of a system or to control it. In fact the linear system written in form (2.11) is the starting point for control. One additional input representing the actuator and one additional output representing a sensor result in the system

$$\dot{\boldsymbol{u}} = A\boldsymbol{u} + B_1 w + B_2 f, \tag{2.17a}$$

$$z = C_1\boldsymbol{u} + f, \tag{2.17b}$$

$$y = C_2\boldsymbol{u} + g. \tag{2.17c}$$

Note that the outputs are also forced. The first output z can be regarded as the objective function,

$$\|z\|^2 = \|C_1\boldsymbol{u}\|^2 + \|f\|^2 = \int_0^T (\boldsymbol{u}^* C_1^* C_1 \boldsymbol{u} + f^* f)\,\mathrm{d}t, \tag{2.18}$$

where it is assumed that the cross weighting between the state and control signal is zero (Zhou *et al.* 1999). The second output is forced with noise g to model the uncertainty that may exists in the measurements under realistic conditions. The so called $\mathcal{H}_2$ control problem can be formulated as following:

Find an optimal control signal $f(t)$ based on the measurements $y(t)$ such that the influence of the external disturbances $w(t)$ and measurement noise $g(t)$ on the output $z(t)$ is minimized.

The solution to this control problem is obtained by solving two quadratic matrix equations called the Riccati equations (Zhou *et al.* 1999). However, these equations require the linearized Navier-Stokes operator A which we do not have at our disposal in an explicit form. On the other hand, we can note that the $\mathcal{H}_2$ control design process amounts to the determination of control signal f given the output signal y. Therefore, it is sufficient to capture only a small fraction of the dynamics, namely the relationship between the input and output signals to design an optimal controller. It thus seems prudent to replace the large matrix A in the Riccati equations with a reduced-order matrix $\hat{A}$ obtained by the projection of equations (2.17) onto the balanced modes. Once the control signal is obtained using the reduced-order model it is applied to full Navier-Stokes system.

The solution to the $\mathcal{H}_2$ in a stochastic framework (also known as Linear Quadratic Gaussian) is derived in Paper 1 and applied to Blasius flow in Paper 2 using a reduced-order model.

CHAPTER 3

Numerical codes

3.1. Direct numerical simulations

The system of partial differential equations given in expression (2.2) for boundary-layer flows is solved numerically using spectral methods. The simulation code is described in detail by Chevalier *et al.* (2007) and employed for the simulations presented in Paper 2 and Paper 3. The spatial discretization is based on Fourier expansion in the streamwise and spanwise directions, and an expansion in Chebyshev polynomials in the wall-normal direction. The time is advanced using a four-step low-storage third-order Runge-Kutta method for the nonlinear and forcing terms, and a second-order Crank-Nicholson method for the linear terms. The code is fully parallelized for efficient use on both shared and distributed-memory systems. To retain periodic boundary conditions, which is necessary for the Fourier discretization, a fringe region is added at the end of the computational domain where a forcing is applied so that the flow smoothly changes from the outflow velocity of the physical domain to the desired inflow velocity (Bertolotti *et al.* 1992; Nordström *et al.* 1999).

3.2. Parabolized stability equations

An alternative for solving the Navier-Stokes equations in weakly spatially developing flows is the parabolized stability equations (PSE) (Herbert 1993; Bertolotti *et al.* 1992). They are based on the expansion of the disturbances into Fourier modes in the horizontal directions. However, in the streamwise direction every mode is decomposed into a slowly varying amplitude function and a wave function with slowly varying wave number. The neglect of the small second derivatives of the slowly varying functions with respect to the streamwise variable leads to an initial boundary-value problem that can be solved by numerical marching procedures.

The PSE approach is a relative fast computational method compared to DNS and is employed in Paper 4 of this thesis. The results presented in Paper 4 are calculated using the NOLOT code, developed by Hanifi *et al.* (1995). A fourth-order compact difference scheme is used to approximate the derivative with respect to the wall-normal coordinate. The derivate with respect to the streamwise coordinate is approximated by a first or second order backward Euler finite difference schemes. The nonlinear terms appear as a source on the right hand side of the equations. The calculations start with fundamental

modes initialized only. The higher modes are introduced in the calculations when the corresponding forcing is larger than a predefined threshold.

CHAPTER 4

Summary of papers

Paper 1

Input-output analysis and control design applied to a linear model of spatially developing flows.

This paper presents a review of recent developments in stability, systems and control theory for a linear model of spatially developing flows. The review covers a wide variety of topics, including transient growth of non-normal systems, convective and absolute instability, global modes, linear input-output systems, model reduction, and optimal/robust design of controllers and observers. The concepts are demonstrated on a single canonical problem, the complex Ginzburg-Landau equation, in order to elucidate the theory presented. The complex Ginzburg-Landau equation is an amplitude equation which arises in the context of non-equilibrium systems and is often used to describe the dynamics near the onset of instability (Chomaz 2005). Here, a linearized version of this model is used to mimic the linearized Navier-Stokes equations. The review is divided into four parts. First, the solution of the linear system (2.4) is investigated, where the stability properties of the matrix exponential e^{At}, in terms of global eigenmodes and optimal disturbances are analyzed. The second part deals with the forced solution (2.12), where the notions of controllability and observability are introduced and the response of the system to impulse, harmonic and stochastic forcing is investigated. In the third section, model reduction techniques based on projection of the linear system on an appropriate subspace is discussed. In the last part of the review, the control design of spatially developing flows is reviewed within the $\mathcal{H}_2/\mathcal{H}_\infty$-framework.

Paper 2

Input-output analysis, model reduction and control of the flat-plate boundary layer.

This paper considers the model reduction and control design of the flat-plate boundary layer from an input-output viewpoint. The linearized Navier-Stokes equations are written in the standard state-space form (2.17). The inputs represent external disturbances, measurement noise and actuators and the outputs represent sensors and objective functions. Using matrix-free methods, such as the snapshot method, the most controllable (or energetic) and observable modes of the linear system are computed and analyzed. For the given inputs and outputs it is found that the observable modes are located upstream in the

physical domain, where the sensitivity to forcing is the largest. The controllable modes are on the other hand located downstream in the domain where the response to forcing is the largest. These two sets of modes can be combined in order to obtain the balanced modes. These modes are computed and used for projection basis of the Navier-Stokes equations in order to construct a reduced-order model. It is shown that the reduced-order model is able to reproduce the input-output behavior of the flat-plate boundary layer with few degrees of freedom. An optimal controller within the $\mathcal{H}_2$ framework is designed using the reduced system and applied to the full Navier-Stokes equations. The closed-loop behavior is significantly different compared to the uncontrolled Navier-Stokes equations. The most amplified frequencies of the latter system are efficiently damped by the control.

Paper 3

The three-dimensional global stability of the jet in crossflow.
In Paper 3 the global linear stability analysis of the jet in crossflow to three-dimensional perturbations is numerically investigated. At a velocity ratio $R = 3$, defined as the ratio of jet velocity to free-stream velocity, the flow is found to be globally linearly unstable. In this case, the temporal frequency of the most unstable global mode is in good agreement with the dominant intrinsic frequency associated with the jet shear-layer vortices observed in direct numerical simulation (DNS). In the DNS code described in section 3.1 the jet is enforced as a boundary condition with parabolic velocity distribution. Shear-layer vortices are continuously shed along the jet trajectory with a well-defined frequency. The base flow for the stability analysis is a steady solution of Navier-Stokes, obtained by damping the unstable temporal frequencies using the selective frequency damping method (Åkervik *et al.* 2006). The steady state consists of a dominant counter-rotating vortex pair in the far field emerging from the near field vorticity of the shear layer. The large eigenvalue problem is solved using the ARPACK library (Lehoucq *et al.* 1998) and the linearized DNS as a time stepper. The most unstable mode takes the shape of a localized wavepacket, wrapped around the counter-rotating vortex pair.

Paper 4

The stabilizing effect of streaks on TS-waves: A parametric study.
In Paper 4, the Parabolized Stability Equations described in section 3.2 are modified to account for the algebraic growth of streamwise elongated vortices called streaks. Using these equations, the nonlinear interaction of TS waves and steady streamwise streaks, and the stabilizing effect of the streaks on the mean flow is verified with previous DNS results (Cossu & Brandt 2002). The amplification of the TS waves is calculated in the presence of a set of streaks with varying spanwise wave numbers and fixed maximum streak amplitudes. In this case, it is found that the optimal stabilization effect is obtained for streaks with the location of the maximum amplitude close to neutral point (branch I)

of the TS wave. These streaks generate the largest total mean flow excess in the unstable streamwise region of the TS waves.

CHAPTER 5

Outlook

Flow control based on systematic methods adopted from control theory is becoming a fairly mature field. Model reduction plays an important role in developing effective control strategies for practical applications, since the dynamical systems which describe most flows are discretized partial differential equations with a very large number of degrees of freedom. Balanced truncation was applied to two-dimensional disturbances in the flat-plate boundary layer in Paper 2. The model reduction procedure will be extended to more general three-dimensional disturbances in the flat-plate layer and also to other more complex geometries. The method is applicable primarily to linear systems, although there is an extensive theory on nonlinear balanced truncation (Scherpen 1993). One method of balanced truncation for nonlinear systems has been introduced by Lall *et al.* (2002), but the method is considerably more expensive than the linear method applied in Paper 2. In the future possible extension of the nonlinear method will be examined in order to make it more computationally feasible.

Stability analysis has until recently only been constrained to the most simple flows due its large memory requirements. DNS on the other hand has been performed for various complex three-dimensional flows such as ducts, diffusers, parabolic leading edge *etc.* In Paper 3, the timestepping-technique for stability analysis employed for fully 3D jet in crossflow has a cost which is comparable to direct numerical simulations. The computation of steady-states based on simple filtering techniques instead of Newton iterations is also an important factor that has enabled the extension of stability analysis to complex flows. In the future, the jet in crossflow for higher velocity ratios will be considered, in order to explore the presence of a critical velocity ratio for global instability. Recently (Barkley *et al.* 2008) the timestepper approach has been extended to optimal transient growth analysis. If a convectively unstable configuration of the jet in crossflow is found, a direct optimal growth analysis will be performed using an adjoint simulation code.

Acknowledgements

I would like to thank my supervisor Professor Dan Henningson for his guidance and generosity during these two years. Many thanks to my co-advisors Dr. Philipp Schlatter and Dr. Luca Brandt for sharing their knowledge with me. I have learned a lot from them. Thanks to my collaborators Prof. Peter Schmid, Dr. Ardeshir Hanifi, Dr. Jérôme Hœpffner, Espen Åkervik and Milos Ilak for all the discussions. I appreciate the helpful comments of Fredrik Lundell and Johan Ohlsson on this manuscript. Thanks to my roommates Lars-Uve Schrader and David Tempelmann and the others in the group Qiang Le, Antonios Monokrousos and Stefan Ivanell for making the working atmosphere so friendly. The Swedish Research council (VR) is gratefully acknowledged for the financing the project.

Finally, I like to thank my family for all their support and especially Sara for her love and encouragement.

Bibliography

Åkervik, E., Brandt, L., Henningson, D. S., Hœpffner, J., Marxen, O. & Schlatter, P. 2006 Steady solutions of the Navier-Stokes equations by selective frequency damping. *Phys. Fluids* **18** (068102), 1–4.

Andersson, P., Berggren, M. & Henningson, D. S. 1999 Optimal disturbances and bypass transition in boundary layers. *Phys. Fluids* **11**, 134–150.

Barkley, D., Blackburn, H. & Sherwin, S. 2008 Direct optimal growth analysis for timesteppers. Submitted.

Barkley, D., Gomes, M. G. & Henderson, R. D. 2002 Three-dimensional instability in flow over a backward-facing step. *J. Fluid Mech.* **473**, 167–190.

Bertolotti, F. P., Herbert, T. & Spalart, P. R. 1992 Linear and nonlinear stability of the Blasius boundary layer. *J. Fluid Mech.* **242**, 441–474.

Chevalier, M., Schlatter, P., Lundbladh, A. & Henningson, D. S. 2007 simson - A Pseudo-spectral solver for incompressible boundary Layer flows. *Tech. Rep* TRITA-MEK 2007:07, ISBN 978-91-7178-838-2. KTH Mechanics, Stockholm, Sweden.

Chomaz, J. M. 2005 Global instabilities in spatially developing flows: Non-normality and nonlinearity. *Ann. Rev. Fluid Mech.* **37**, 357–392.

Corbett, J. & Koehler, H. 2003 Updated emissions from ocean shipping. *J. Geophys. Res.* **108** (D20), 4650–4664.

Cossu, C. & Brandt, L. 2002 Stabilization of Tollmien-Schlichting waves by finite amplitude optimal streaks in the Blasius boundary layer. *Phys. Fluids* **14**, L57.

Glover, K. 1984 All optimal Hankel-norm approximations of linear multivariable systems and the L^∞-error bounds. *Int. J. Control* **39**, 1115–1193.

Hanifi, A., Hein, S., Bertolotti, F. & Henningson, D. S. 1995 Nolot – Non-local linear stability equations. *Tech. Rep* FFA TN 1994-54.

Herbert, T. 1993 Parabolized stability equations. In *Progress in Transition Modelling*, pp. 4–1–4–33. AGARD.

Kim, J. & Bewley, T. R. 2007 A linear systems approach to flow control. *Ann. Rev. Fluid Mech.* **39**, 383–417.

Lall, S., Marsden, J. E. & Glavaski, S. 2002 A subspace approach to balanced truncation for model reduction of nonlinear control systems. *Int. J. Robust Nonlinear Control* **12**, 519–535.

Lehoucq, R., Sorensen, D. & Yang, C. 1998 *ARPACK Users' guide: Solution of large-scale eigenvalue problems with implicitly restarted Arnoldi methods*. Philadelphia: SIAM.

Molder, C. & Van Loan, C. 2003 Ninteen dubios ways to compute the exponential of a matrix, twenty-five years later. *Siam Review* **45**, 3–000.

Moore, B. 1981 Principal component analysis in linear systems: Controllability, observability, and model reduction. *Automatic Control, IEEE Transactions* **26** (1), 17–32.

Nordström, J., Nordin, N. & Henningson, D. S. 1999 The fringe region technique and the Fourier method used in the direct numerical simulation of spatially evolving viscous flows. *SIAM J. Sci. Comput.* **20** (4), 1365–1393.

Rowley, C. W. 2005 Model reduction for fluids using balanced proper orthogonal decomposition. *Int. J. Bifurc. Chaos* **15** (3), 997–1013.

Scherpen, J. M. 1993 Balancing for nonlinear systems. *Syst. and Contr. Lett.* **21**, 143–153.

Trefethen, L. & Bau, D. 1997 *Numerical Linear Algebra.* Philadelphia: SIAM.

Trefethen, L. & Embree, M. 2005 *Spectra and Pseudospectra — The Behavior of Nonnormal Matrices and Operators*. New Jersey: Princeton University Press.

Zhou, K., Salomon, G. & Wu, E. 1999 Balanced realization and model reduction for unstable systems. *Int. J. Robust Nonlinear Control* **9**, 183–198.

Part II

Papers

1

Paper 1

Input-output analysis and control design applied to a linear model of spatially developing flows

By Shervin Bagheri[*], Jérôme Hœpffner[†], Peter J. Schmid[‡] & Dan S. Henningson[*]

[*]Linné Flow Centre, Department of Mechanics
Royal Institute of Technology, S-100 44 Stockholm, Sweden

[†]Institut de Recherche sur les Phénomènes Hors Équilibre (IRPHÉ),
CNRS-Université d'Aix-Marseille, F-13384 Marseille, France

[‡]Laboratoire d'Hydrodynamique (LadHyX), CNRS-École Polytechnique,
F-91128 Palaiseau, France

Accepted for publication in Applied Mechanics Reviews

1. Introduction

Whereas stability theory has long occupied a central role in fluid mechanics research, control theory has only recently been applied to fluid systems. Despite its long history, stability theory has undergone remarkable changes over the past decades. The incorporation of short-term instabilities into a traditionally asymptotic stability concept, the equal treatment of stability and response behavior within the same mathematical framework, and use of system-theoretical tools to probe the disturbance behavior of fluid systems have reinvigorated hydrodynamic stability theory and developed it into a modern tool of fluid dynamic research. Especially the formulation of the governing equations in state-space form combined with an input-output viewpoint of the perturbation dynamics has brought the two fields of stability and control theory closer together. Whereas stability theory is concerned with all aspects of the open-loop dynamics of the governing equations, control theory connects the output to the input and focuses on the closed-loop characteristics — including optimal design and performance analysis — of the underlying dynamical system. These two closely related disciplines, and the unifying formulation that connects them, are the subject of this review. Due to the vastness of these two fields, we restrict ourselves to concepts of direct relevance to fluid dynamical systems as well as to a simple model equation. The Ginzburg-Landau equation, a well-known model equation displaying a great variety of phenomena observed in fluid systems, will be used to demonstrate and exemplify concepts and techniques from stability, systems and control theory.

The recognition that short-term instabilities play an important role in fluid dynamical systems can be traced back nearly two decades when scientists searched for disturbances that optimize energy amplification over a finite time span (Farrell 1988; Butler & Farrell 1992; Reddy *et al.* 1993; Reddy & Henningson 1993). These disturbances did not resemble the most unstable eigenvectors of the system which led to the development of a theoretical foundation to describe short-term nonmodal phenomena (Trefethen *et al.* 2005; Farrell & Ioannou 1996; Schmid & Henningson 2001; Schmid 2007). In fact, even if the flow is asymptotically stable, substantial amplification of the input signal (initial condition or external forcing) into an output signal (energy) can occur. By now, the associated theory has matured into an important component for understanding the transition process from laminar to turbulent fluid motion and has been able to explain a variety of observed fluid structures in transitional and turbulent shear flows (Schmid & Henningson 2001). In a further step, an input-output framework has been suggested Jovanovic & Bamieh (2005) which brings the analysis of stability characteristics closer to a system theoretic interpretation, with impulse response, frequency response and transfer functions as the principal tools of investigation.

At the same time, flow control based on control theory has emerged as a new discipline of fluid mechanics (Joshi *et al.* 1997; Bewley & Liu 1998; Lee *et al.* 2001; Högberg *et al.* 2003*a*,*b*; Hœpffner *et al.* 2005; Chevalier *et al.* 2006, 2007; Åkervik *et al.* 2007; Monokrousos *et al.* 2008). Starting with simple feedback control laws and full-state information control, it has progressed toward more realistic configurations by incorporating the estimation problem and partial-state information control. During the control design process, a strategy is determined that feeds information from the measurements (sensors) back to the input signal (actuators) such that a given control objective is achieved. The accompanying theoretical basis, adapted from control theory (Kwakernaak & Sivan 1972; Anderson & Moore 1990; Lewis & Syrmos 1995; Zhou *et al.* 2002), to determine these strategies has evolved substantially, and flow control has advanced into an independent and active field of fluid dynamics. Comprehensive accounts on recent progress in the rapidly expanding field of flow control can be found in Gal-El-Hak (1996); Bewley (2001); Kim (2003) and Kim & Bewley (2007).

The input-output framework provides not only a convenient way of analyzing stability and receptivity characteristics (Hill 1995; Luchini & Bottaro 1998) of fluid systems, it represents the natural starting point for control design. Stability and receptivity analysis as well as control design can thus be accomplished within the same formal setting. This unified analysis shall be exemplified in this review article by investigating the stability and response properties of the Ginzburg-Landau equation and by devising effective control strategies including the evaluation of their efficiency and performance. The Ginzburg-Landau equation has frequently been used as a model for instabilities in fluid systems, see *e.g.* Huerre & Monkewitz (1990) and Chomaz (2005). We will use it here

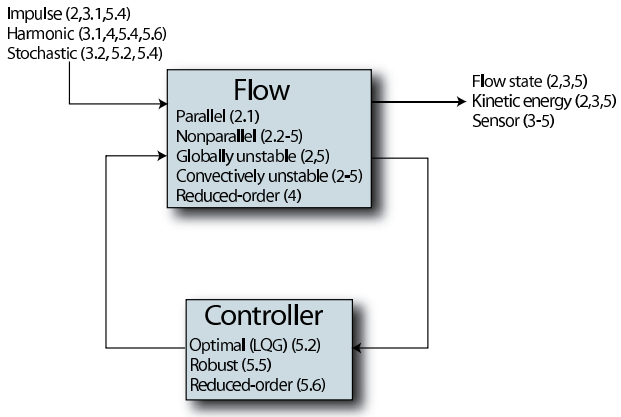

FIGURE 1. Overview of the open-loop and closed-loop analysis performed in this review. The response in terms of the flow state, kinetic energy and sensor signal to impulse, harmonic and stochastic inputs of the parallel, non-parallel, convectively unstable and globally unstable Ginzburg-Landau equation is investigated in Sections 2 and 3. Model reduction of the system is performed in section 4 followed by optimal (LQG), robust ($\mathcal{H}_\infty$) and reduced-order control design in section 5.

with two different sets of parameters: one set to model globally unstable flows (so-called *oscillators*), and another set to describe convectively unstable flows (so-called *noise amplifiers*). The Ginzburg-Landau equation has also been the subject to several flow control studies (Monkewitz 1989; Park *et al.* 1993; Lauga & Bewley 2003, 2004; Cohen *et al.* 2005).

The review is organized as follows (see also figure 1): we start with a summary of stability results for the Ginzburg-Landau equation in section 2 where results for both asymptotic behavior and transient growth will be presented. In section 3 we investigate the input-output behavior of linear systems in general, and the Ginzburg-Landau equation in particular. The response to impulsive, harmonic and stochastic forcing will be considered, and the concepts of controllability and observability will be introduced. In section 4 we review the projection method of model reduction using global eigenmodes, POD modes and balanced truncation. Section 5 deals with the control design for the Ginzburg-Landau equation. We present a detailed derivation of the LQG (Linear Quadratic Gaussian) control framework, raise the important issue of actuator and sensor placement, and conclude by discussing robust control. Concluding remarks and a summary of the presented material are offered in the last section.

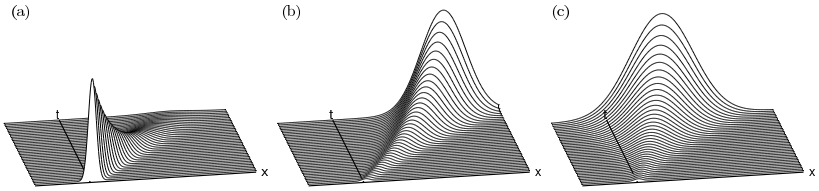

FIGURE 2. Local stability concepts based on the linear response of the parallel Ginzburg-Landau equation to a temporally and spatially localized pulse at $t = 0$ and $x = 0$, displayed in the x-t-plane. (a) stable configuration $\mu_0 \leq 0$: the solution at $t = t_1 > 0$ is damped everywhere; (b) convectively unstable configuration $0 < \mu_0 < \mu_t$: the solution at $t = t_1$ is amplified, but is zero along the ray $x/t = 0$; (c) absolutely unstable configuration $\mu_t \leq \mu_0$: the state is amplified at $t = t_1$ and nonzero along the ray $x/t = 0$.

2. Asymptotic and transient behavior

2.1. *Parallel flows — fundamental concepts*

Before applying modern techniques of hydrodynamic stability theory (Schmid & Henningson 2001) to the full Ginzburg-Landau model describing spatially varying flows, we will first introduce and analyze a simpler version of the Ginzburg-Landau equation. By neglecting the spatial dependence of the flow, thus arriving at the parallel (*i.e.* constant-coefficient) Ginzburg-Landau equation, we will apply concepts of linear stability analysis to describe the growth and decay of disturbances in time and/or space.

The parallel Ginzburg-Landau equation on the infinite interval $-\infty < x < \infty$ reads

$$\frac{\partial q}{\partial t} = \mathcal{A}q = \left(-\nu\frac{\partial}{\partial x} + \gamma\frac{\partial^2}{\partial x^2} + \mu\right) q, \tag{1a}$$

$$q(x,t) < \infty \quad \text{as} \quad x \to \pm\infty, \tag{1b}$$

with initial condition $q(x,0) = q_0(x)$ and $\mathcal{A}$ as the Ginzburg-Landau operator. The solutions $q(x,t)$ are functions in $\mathbb{C}$ with the inner-product defined as $\langle f, g\rangle = \int_{-\infty}^{\infty} g^* f \mathrm{d}x$. We occasionally refer to the this norm as the energy norm. The superscript * denotes the complex conjugate. The convective and the dissipative nature of the modeled flow is represented by the complex terms $\nu = U + 2ic_u$ and $\gamma = 1 + ic_d$, respectively. The above equation is of convection-diffusion type with an extra real-valued term $\mu = \mu_0 - c_u^2$ to model the presence of exponential instabilities. The significance of the complex terms c_d and c_u will become clearer when we decompose the system into wave-like solutions.

We first investigate the linear stability of the parallel Ginzburg-Landau equation, *i.e.* the spatio-temporal evolution of the perturbation $q(x,t)$ about

the basic state $q_B(x,t) = 0$. As introduced by Briggs (1964), this spatio-temporal evolution of perturbations in fluid flow can be described by three basic types of local behavior: (i) stable, (ii) convectively unstable and (iii) absolutely unstable. Our model equation, in fact, has by construction the minimum number of required terms to give rise to a successive transition through the three types of instability.

The three types of disturbance behavior can be probed by computing the response to a spatially and temporally localized pulse as this pulse evolves in space and time. Figure 2 demonstrates the three types of responses that may be observed. First, the amplitude may asymptotically decay in time throughout the entire domain (see figure 2a). In this case, the basic flow is deemed linearly stable. Second, a convectively unstable flow is shown in figure 2b; in this case, the perturbation grows in time, but is convected away from the location at which it was generated, so that the response eventually decays to zero at every spatial location. Finally, for an absolutely unstable flow (see figure 2c) the perturbation is amplified both upstream and downstream of the location it was generated and thus contaminates the entire spatial domain over time.

The response behavior to a δ-function applied at $(x,t) = (0,0)$ is equivalent to the Green's function or impulse response of the complex Ginzburg-Landau equation. We will return to this concept in a subsequent section of this review. In what follows, we will first exploit the homogeneity in space and time and seek solutions in the wavenumber/frequency (Fourier) space. The dispersion relation linking wavenumber and frequency then fully describes the evolution of wavelike (and by superposition) non-wavelike solutions. Criteria for stability or instability of the solutions, as well as the type of instability, follow easily from the dispersion relation.

We express the solutions $q(x,t)$ as a superposition of normal modes

$$\tilde{q}(k,\omega)\exp(ikx - i\omega t) \tag{2}$$

with wavenumber k, frequency ω, and (complex) amplitude $\tilde{q}$. The imaginary part of k and ω determines the stability of the associated solution, whereas the real part describes the oscillatory behavior in x and t, respectively. Introducing this normal mode decomposition into (1) results in the dispersion relation, $D(k,\omega;\mu_0) = 0$, which takes the form

$$\omega = Uk + c_d k^2 + i(\mu_0 - (k - c_u)^2). \tag{3}$$

Within the temporal framework, an initial periodic perturbation with *real* wavenumber k grows exponentially in time when μ_0 in (3) exceeds $(k - c_u)^2$, *i.e.* when exponential growth exceeds diffusion. In this case, $\omega_i(k) > 0$ and the associated normal mode $\tilde{q}$ exhibits exponential temporal growth. Furthermore, we observe a finite interval $k \in [c_u - \sqrt{\mu_0}, c_u + \sqrt{\mu_0}]$ of unstable spatial wavenumbers. A simple criterion for linear stability of the flow can be deduced by considering the growth rate $\omega_i = \omega_{i,max}$ of the most unstable wave $k = k_{max}$ in this interval. For the dispersion relation (3), we observe that $k_{max} = c_u$ and the corresponding growth rate is $\omega_{i,max} = \mu_0$. Thus, the condition for a local

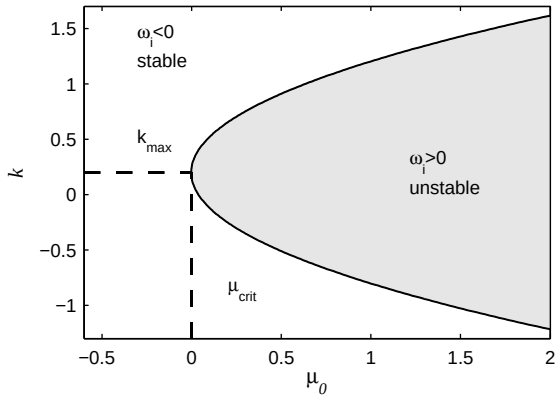

FIGURE 3. The neutral stability curve for the parallel Ginzburg-Landau equation (with $c_u = 0.2$) in the (μ_0, k)-plane.

linear instability becomes,

$$\mu_0 \leq 0 \qquad \text{locally stable,} \tag{4a}$$

$$\mu_0 > 0 \qquad \text{locally unstable.} \tag{4b}$$

In figure 3, the neutral curve, defined by $\omega_{i,max} = 0$, is displayed as a function of μ_0 and k. We see that the range of unstable wavenumbers increases as μ_0 increases.

To further investigate the two types of locally unstable configurations — convectively unstable and absolutely unstable — it is instructive to consider perturbations that consist of a superposition of normal modes near $k = c_u$ which form a travelling wavepacket. From the dispersion relation (3) we conclude that individual wave components of this wavepacket travel at the phase velocity

$$\omega_r/k = U + c_d k, \tag{5}$$

whereas the wavepacket itself, and therefore the perturbation, travels at the group velocity

$$U_{max} = \frac{\partial \omega}{\partial k} = U + 2c_d c_u. \tag{6}$$

In general, the group velocity is complex but carries a physical meaning when it is real, which is always the case for the most unstable wavenumber c_u.

The disturbance behavior in the unstable region depends on the competition between convection and instability. For the Ginzburg-Landau equation we find that the flow is convectively unstable if $U_{max} > 2\sqrt{\mu_0}|\gamma|$, *i.e.*, when the group velocity exceeds the exponential instability of the unstable region (for constant diffusion). This means that, for convection-dominated flows, perturbations grow as they enter the unstable domain but are quickly convected downstream, beyond the unstable region where they decay, and the basic state

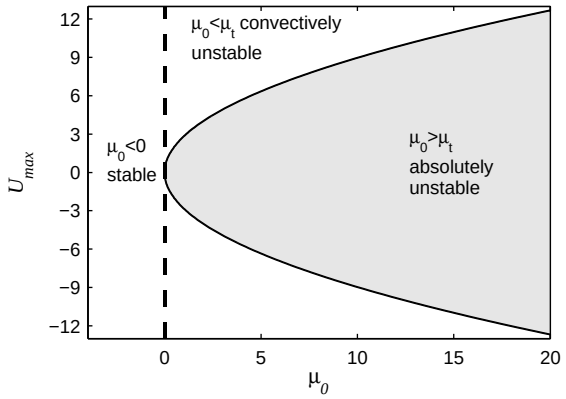

FIGURE 4. The neutral absolute stability curve for the parallel Ginzburg-Landau equation (with $\gamma = 1 - i$) in the $(\mu_0, U_{\max})$-plane.

relaxes back to its original state (see figure 2b). However, when μ_0 exceeds the critical value of

$$\mu_t = \frac{U_{max}^2}{4|\gamma|^2}, \tag{7}$$

there exists an unstable wavelength with zero group velocity. As the perturbation is amplified in the unstable domain, it will gradually contaminate the entire physical domain and render the flow absolutely unstable. In figure 4, the neutral curve, defined by $\mu_t = 0$, is displayed as a function μ_0 and U_{max}. The critical value μ_t is obtained by considering a wavepacket with a zero group velocity $\partial\omega/\partial k = 0$ (see Huerre (2000) for an exact derivation). The associated growth rate $\omega_i = \omega_{i,0}$ is the absolute growth rate. Unlike for our case, the absolute frequency ω_0 for realistic flow configurations can seldom be found in analytic form. Instead, one has to resort to Briggs' method (Briggs (1964), see also Huerre (2000)) which amounts to locating pinch points in the complex k-plane. In addition to the criterion of zero group velocity, one must ensure that the two spatial branches $k^+(\omega)$ and $k^-(\omega)$ (for real ω) in (3) originate from the upper and lower halves of the complex k-plane.

2.2. *Spatially developing flows — a global approach*

Despite the limitations of a parallel flow assumption, the above results carry over to weakly non-parallel flows as described in Monkewitz (1990); Huerre & Monkewitz (1990); Chomaz *et al.* (1991); Le Dizés *et al.* (1996). Within a Wentzel-Kramers-Brillouin-Jeffreys (WKBJ) approximation, one can draw conclusions about the global stability behavior from investigating the dispersion relation locally. Many realistic flows, however, are strongly non-parallel which requires us to resort to a global stability analysis. In this section, we will adopt this global point of view to investigate the stability properties of a simple model

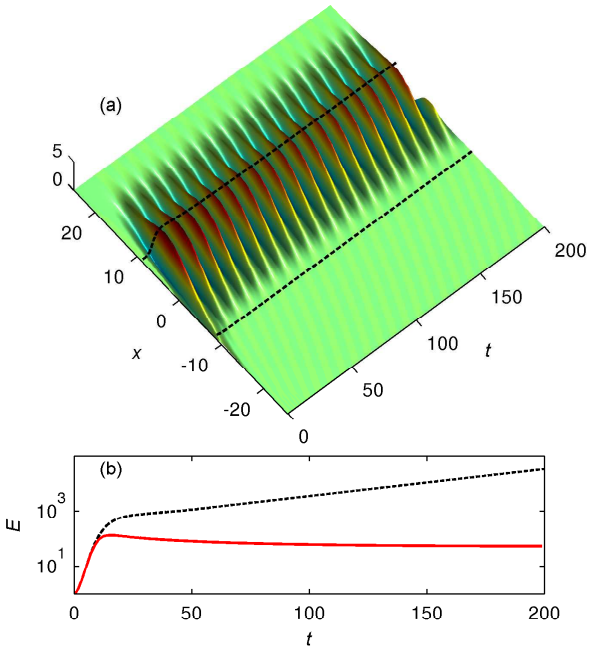

FIGURE 5. (a) The spatio-temporal evolution of a disturbance in a globally unstable flow. The disturbance grows exponentially until the cubic nonlinear term $-|q|^2q$ (see Chomaz *et al.* (1990); Chomaz (2005) for details of the nonlinear Ginzburg-Landau equation) causes the disturbance to saturate and oscillate. (b) The energy that corresponds to the evolution in (a) is shown in red, and the linear exponential growth for the linear Ginzburg-Landau equation is shown in dashed black.

flow which depends on the flow direction x. We will see that a rich disturbance behavior is uncovered which has its roots in the non-normality of the underlying evolution operator (Trefethen 1997; Trefethen & Embree 2005; Davies 2002). As a first step, one solves a global eigenvalue problem. Assuming completeness, any perturbation can then be decomposed into the global eigenfunctions of the governing operator. If there exists an unstable global mode, it is amplified until it saturates due to nonlinearity and may lead to self-sustained oscillations in the flow (figure 5). The short-time, or transient, behavior can also be captured by global modes (Cossu & Chomaz 1997; Henningson & Åkervik 2008), if one considers a superposition of them. For non-normal stability operator with corresponding non-orthogonal global modes a superposition of decaying global modes can result in a large transient amplification of perturbation energy (figure

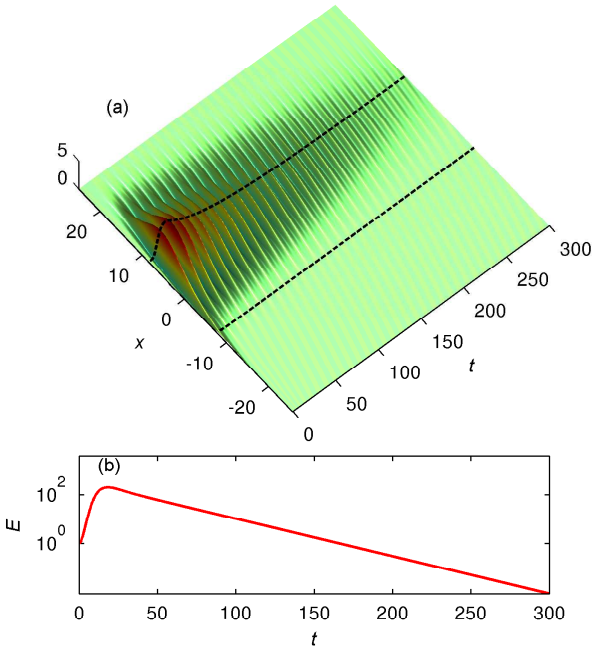

FIGURE 6. (a) Linear transient growth of a perturbation in space and time: an optimal initial perturbation grows as it enters the unstable domain at branch I at $x = -8.2$ until it reaches branch II at $x = 8.2$. The two dashed lines depict branch I and II. (b) The corresponding optimal energy growth of the convectively unstable flow in (a).

6). As demonstrated by Cossu & Chomaz (1997), this transient behavior often corresponds to a localized convective instability when using a local approach.

The linear complex Ginzburg-Landau equation serves as a simple model for capturing both the short-time and long-time evolution of small perturbations $q(x,t)$ in spatially developing flows. We will use this model equation to illustrate fundamental concepts of linear global stability analysis. If the parameter μ, responsible for the local instability in equation (1), is now taken as a function of x, the Ginzburg-Landau equation becomes a variable-coefficient partial differential equation modeling non-parallel flows (Hunt & Crighton 1991). The Ginzburg-Landau equation with μ as a linear function in x can be used to mimic flows on the interval $[0,\infty)$ as shown in Chomaz *et al.* (1988). We will adopt the commonly used quadratic function (Hunt & Crighton 1991; Cossu &

Chomaz 1997),

$$\mu(x) \quad = (\mu_0 - c_u^2) + \mu_2 \frac{x^2}{2}, \qquad\qquad \mu_2 < 0. \tag{8}$$

The flow is now susceptible to instabilities only when $\mu(x) > 0$, which defines a confined unstable region in the x-direction given by $-\sqrt{-2(\mu_0 - c_u^2)/\mu_2} < x < \sqrt{-2(\mu_0 - c_u^2)/\mu_2}$. The upstream and downstream edge of the unstable domain are referred to as branch I and II, respectively, and are indicated by the two black dashed lines in figure 5 and 6. The extent of this region depends on the parameter μ_2 which can be interpreted as the degree of non-parallelism of the flow. The operator $\mathcal{A}$ in (1) with $q(x,t)$ bounded for $x = \pm\infty$ is non-normal if both the term involving μ_2 and the convection term ν are non-zero. As demonstrated in Cossu & Chomaz (1997) and Chomaz (2005) the smaller μ_2 and/or the larger ν the stronger the non-normality of the operator $\mathcal{A}$. The parameter μ_2 thus plays a dual role: for large values of μ_2 the system is strongly non-parallel but weakly non-normal, while for very small values of μ_2 the system represents weakly non-parallel but strongly non-normal flow. For the latter case, a local analysis may be more appropriate as the resulting global eigensystem is rather ill-conditioned (Chomaz 2005; Trefethen & Embree 2005).

A global mode of the Ginzburg-Landau equation is defined as

$$q(x,t) = \phi(x)\exp(\lambda t) \tag{9}$$

and is a solution to the eigenvalue problem

$$\lambda\phi(x) = \mathcal{A}\phi(x) \qquad\qquad \phi(x) < \infty \quad \text{as} \quad x \to \pm\infty, \tag{10}$$

where $\mathcal{A}$ is the operator defined in (1). The flow is globally unstable when the real part of any eigenvalue λ is positive which results in self-excited linear oscillations in the flow of a frequency given by the imaginary part of λ. For the case $\mu_2 \neq 0$ the eigenvalue problem (10) for the Ginzburg-Landau equation (1) can be solved analytically (Chomaz *et al.* 1987). One obtains

$$\lambda_n \quad = \quad (\mu_0 - c_c^2) - (\nu^2/4\gamma) - (n + 1/2)h, \tag{11a}$$

$$\phi_n(x) \quad = \quad \exp\{(\nu/2\gamma)x - \chi^2 x^2/2\} H_n(\chi x), \tag{11b}$$

with $h = \sqrt{-2\mu_2\gamma}$, $n = 0, 1\ldots$ and H_n as the nth Hermite polynomial, scaled with $\chi = (-\mu_2/2\gamma)^{1/4}$. Global instability is determined by the sign of the first eigenvalue ($n = 0$) which yields the criterion for global instability as $\mu_0 > \mu_c$ where

$$\mu_c = \mu_t + \frac{|h|}{2}\cos\left(\frac{\mathrm{Arg}\gamma}{2}\right) \tag{12}$$

and μ_t is the threshold value for absolute instability (7). The term Arg denotes the phase angle of γ. We therefore conclude from (12) that the threshold for a global instability is higher than the one for an absolute instability. Formulated in another way, an absolute instability is a necessary condition for a global instability.

The short-time behavior of a disturbance cannot be predicted by studying individual eigenmodes. Instead, a more detailed analysis of the properties of the stability operator $\mathcal{A}$ is necessary. When $\mu_2 \neq 0$ and $\nu \neq 0$ the Ginzburg-Landau operator $\mathcal{A}$ is non-self-adjoint (Davies 2002), *i.e.*, $\langle q_1, \mathcal{A}q_2\rangle \neq \langle \mathcal{A}q_1, q_2\rangle$. As a consequence, the global modes are non-orthogonal $\langle \phi_n, \phi_m\rangle \neq \delta_{nm}$, and although they may form a complete basis, they are nearly colinear and their superposition may lead to large transient growth (figure 6b). We will study this issue in more detail by considering an expansion in global modes. To this end, we find the adjoint global modes as

$$\psi_n(x) = \exp\{(-\nu^*/\gamma^*)x\}\phi_n^*(x) \tag{13}$$

which satisfy the adjoint eigenvalue problem

$$\lambda_n^*\psi_n(x) = \mathcal{A}^+\psi_n(x), \tag{14}$$

where

$$\mathcal{A}^+ = \nu^*\frac{\partial}{\partial x} + \gamma^*\frac{\partial^2}{\partial x^2} + \mu^*(x) \tag{15}$$

with boundary condition $\psi_n(x) < \infty$ as $x \to \pm\infty$. The superscript * denotes the complex conjugate. The adjoint global modes ψ_n are bi-orthogonal to the global modes (11) according to

$$\langle \psi_n, \phi_m\rangle = N_{nm}\delta_{n,m} \tag{16}$$

with N_{nm} as a normalization factor that we choose such that $\|\phi_n\| = \|\psi_n\| = 1$. The adjoint mode (13) distinguishes itself from its direct counterpart (11b) mainly by the sign of the basic flow convection term ν. This manifests itself by a characteristic separation of the direct and adjoint global mode in space. In figure 7a and b, the two first direct and adjoint global modes of the Ginzburg-Landau equation are shown where the separation in x is seen to increase for higher modes, until the support of the direct and adjoint mode is nearly disjoint. Consequently, $N_{nn} = \langle \phi_n, \psi_n\rangle$ becomes increasingly small, a phenomenon we shall investigate further in what follows.

We continue by stating that a sequence of global modes $\{\phi_n\}_{n=0}^{\infty}$ forms a basis if any solution of the Ginzburg-Landau equation has a norm-convergent expansion

$$q(x,t) = \sum_{n=0}^{\infty}\kappa_n\phi_n(x)\exp(\lambda_n t), \tag{17}$$

where the expansion coefficients κ_n are obtained using the adjoint global modes and the initial condition q_0 according to

$$\kappa_n = \frac{\langle q_0, \psi_n\rangle}{\langle \phi_n, \psi_n\rangle}. \tag{18}$$

The denominator of the above expression, *i.e.* N_{nn}, becomes very small when the direct and adjoint global modes have nearly disjoint spatial support. In this case, the expansion coefficients (18) of q become large. Although the amplitude of all stable global modes decreases monotonically in time, their superposition produces a wavepacket that transiently grows in time as it propagates in space.

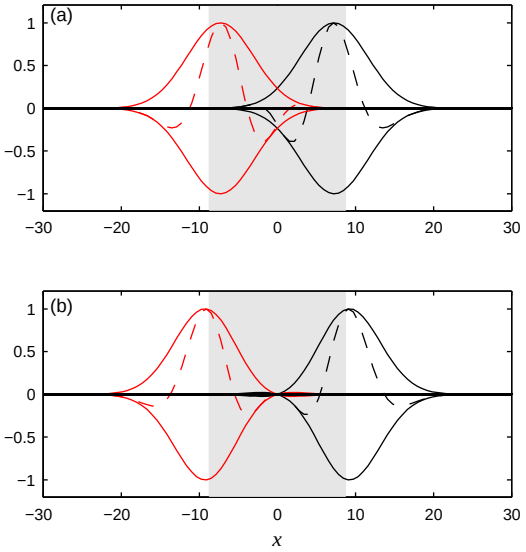

FIGURE 7. The first (a) and second (b) global (black lines) and adjoint eigenmode (red lines) of the Ginzburg-Landau equation with the absolute value shown in solid and real part in dashed. The gray area marks the region of instability

Although it is possible (Ehrenstein & Gallaire 2005; Åkervik *et al.* 2007, 2008; Henningson & Åkervik 2008), in practice the short-time amplification of disturbances is rarely computed using global modes. Instead one computes the norm of the exponential matrix (Trefethen & Bau 1997), $\|e^{At}\|$, as we shall demonstrate next.

2.3. *Optimal energy growth and resolvent norms*

For sufficiently large transient amplifications nonlinear effects can no longer be neglected, and, in real flows, more complex instabilities or transition to turbulence are often triggered. For this reason it seems important to investigate the most dangerous initial condition that results in a maximum energy amplification over a specified time interval (Reddy *et al.* 1993; Reddy & Henningson 1993; Farrell 1988; Corbett & Bottaro 2001; Andersson *et al.* 1999; Luchini 2000).

For simplicity, we will formulate and present results using the *discrete* Ginzburg-Landau operator A. See Appendix A for details of the numerical approximation of the operator $\mathcal{A}$. The continuous approach can be found in Trefethen & Embree (2005). The values of the Ginzburg-Landau parameters used in the computations that follows can be found in Table 1.

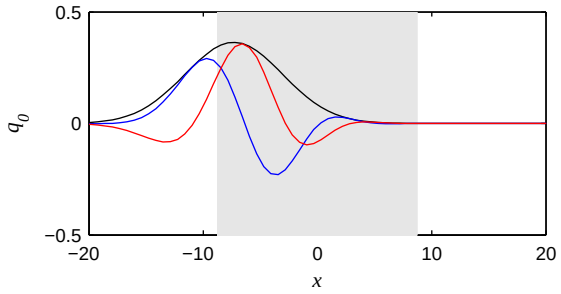

FIGURE 8. Shape of an optimal disturbance with the absolute value shown in black, the real and imaginary part shown in blue and red, respectively. The gray region markes the unstable region, where disturbances grow exponentially. The maximum value of the optimal disturbance is located close to branch I.

The discrete energy norm given by (107) can, after a Cholesky decomposition of the energy weight matrix $M = F^H F$, be related to the standard Euclidean norm of a disturbance by

$$E(t) = \|q\|_M^2 = \|Fq\|_2^2. \tag{19}$$

We can now define the maximum transient growth of the perturbation energy at time t as

$$\begin{aligned} E_{max}(t) &= \max_{\|q_0\|>0} \frac{\|q(t)\|_M^2}{\|q_0\|_M^2} \\ &= \max_{\|q_0\|>0} \frac{\|Fe^{At}q_0\|_2^2}{\|Fq_0\|_2^2} = \|Fe^{At}F^{-1}\|_2^2 = \sigma_1^2 \end{aligned} \tag{20}$$

where σ_1 is determined from a singular value decomposition,

$$Fe^{At}F^{-1} = U\Sigma V^H, \qquad \Sigma = \mathrm{diag}\{\sigma_1, \ldots, \sigma_n\}. \tag{21}$$

The above expression contains an optimization over all possible initial conditions, and the peak value of $\sigma_1^2(t)$ is the maximum energy amplification over time. Optimal initial disturbances can be calculated according to $q_0 = F^{-1}V_1$ where V_1 is the right principal singular vector of the SVD in equation (21). The maximum growth and the corresponding optimal disturbance can also be obtained from power iterations (Andersson *et al.* 1999; Schmid & Henningson 2001).

The optimal initial disturbance of the Ginzburg-Landau equation shown in figure 8 is located at the upstream boundary of the unstable domain. As time evolves it traverses the unstable domain (gray region), where it can exhibit either decay, transient growth or asymptotic exponential growth as illustrated in figure 9 depending on the value of bifurcation parameter μ_0 (*i.e.* the Reynolds number for Navier–Stokes equations). The optimal energy growth curves

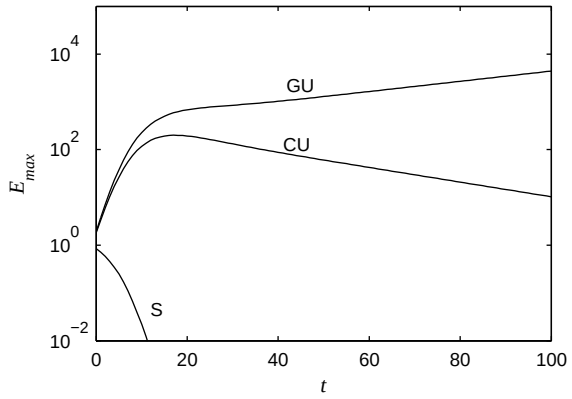

FIGURE 9. Optimal energy growth, E_{max}, as a function of time. (S) stable configuration $\mu_0 < 0$: the perturbation energy decays exponentially for all time; (CU) convectively unstable configuration $0 < \mu_0 < \mu_c$: the perturbation energy is amplified initially but decays to zero asymptotically; (GU) globally unstable configuration $\mu_c < \mu_0$: the perturbation energy grows exponentially asymptotically. The values of the parameters used in the computations are listed in Table 1.

shown in figure 9 corresponds to a stable (S), convectively unstable (CU) and globally unstable (GU) flow configuration. Note that, for both (S) and (CU) configurations, all global modes are stable. However, only for the latter case do we have $\mu_0 > 0$ yielding a locally convectively unstable spatial region. Consequently, a transient energy growth of two orders of magnitude can be observed before asymptotic decay sets in (Cossu & Chomaz 1997).

To conclude this section, we investigate the effect on global modes and on the global spectrum as the operator $\mathcal{A}$ is discretized. The spectrum of $\mathcal{A}$ is displayed in figure 10 by the green symbols using the analytical expression (11). The spectrum of the discretized Ginzburg-Landau operator A is shown by the blue symbols. A characteristic split of the eigenvalue branch is observed which is rather common in finite-precision stability computations of strongly non-normal flows. The reason for this split is the insufficient resolution to accurately capture the increasingly oscillatory behavior of the associated eigenfunctions. These observations are closely related to the notion of pseudospectra (Trefethen & Embree 2005).

It is misleading to assume that if $A\phi \approx s\phi$, then s is close the spectrum of A. If s is taken as an approximate eigenvalue in the sense that $\|A\phi - s\phi\|_M < \epsilon\|\phi\|_M$, we can conclude that, for normal systems, ϵ can be as chosen as small as one wishes. For non-normal systems, however, the minimum value of ϵ can become very large. This observation suggests the definition of the

	Subcritical	Supercritical
$\{\mu_0, \mu_2\}$	$\{0.38, -0.01\}$	$\{0.41, -0.01\}$
$\{\nu, \gamma\}$	$\{2 + 0.2i, 1 - i\}$	$\{2 + 0.2i, 1 - i\}$
$\{x_I, x_{II}\}$	$\{\pm 8.2\}$	$\{\pm 8.2\}$
$\{x_w, x_s, x_u, s\}$	$\{-11, 0, -3, 0.4\}$	$\{-11, 9, -9, 0.1\}$
$\{R, W, G, \gamma_0\}$	$\{1, 1., 0.1/1.0, 9\}$	$\{1, 0.1, 9\}$

TABLE 1. Parameters $\{\mu_0, \mu_2\}, \{\nu, \gamma\}$ of the Ginzburg-Landau equation given in (1) and (8). The critical values for global and absolute stability are $\mu_c = 0.3977$ and $\mu_t = 0.32$, respectively. External disturbances (B_1), sensor (C_2) and actuator (B_2) are Gaussian functions (see equations (108)) with mean given by x_w, x_s and x_u, respectively and a width of $s = 0.4$. Design parameters $\{R, W, G, \gamma_0\}$ for the LQG- and $\mathcal{H}_\infty$-compensators are the control penalty (R), the covariance of the disturbance (W) and sensor noise (G), and a bound on the ∞-norm, (γ_0).

pseudospectrum of A as the sets in the complex plane such that

$$\{s \in \mathbb{C} : \|R(s)\|_M = \|(sI - A)^{-1}\|_M > \epsilon^{-1}\}. \tag{22}$$

The pseudospectrum of A (shown in figure 10) is visualized as a contour plot of the norm of the resolvent

$$\|R(s)\|_M = \|FR(s)F^{-1}\|_2 = \sigma_1(s) \tag{23}$$

where $\sigma_1(s)$ is the largest singular value of $FR(s)F^{-1}$. It is then straightforward to conclude that the eigenvalues of the discretized Ginzburg-Landau operator A are in fact ϵ-pseudoeigenvalues for ϵ equal to machine precision and thus align with the 10^{15}-contour of the resolvent norm in figure 10. For an alternative approach to characterize the system sensitivity see Biau & Bottaro (2004).

The resolvent contours moreover give an indication of the existence of non-normal effects, since the amount by which the contours protrude into the unstable half-plane can be used to estimate the maximum transient growth of energy (Trefethen & Embree 2005; Schmid 2007). We will return to this concept and use the resolvent norm from an input-output viewpoint in the next section, where we generalize the resolvent to transfer functions — one of the most central concepts in the design of control strategies.

2.4. *Stability of supercritical and subcritical flows*

Based on the global and local stability concepts introduced in the previous sections we are now in a position to define two fundamentally different scenarios that model the behavior of disturbances in a large number of flows.

The first model is known as the supercritical case, in which any flow disturbance will grow exponentially until it saturates due to nonlinearities, as shown in figure 5. A global analysis shows at least one unstable eigenmode of $\mathcal{A}$, yielding a globally unstable flow. This type of scenario prevails when

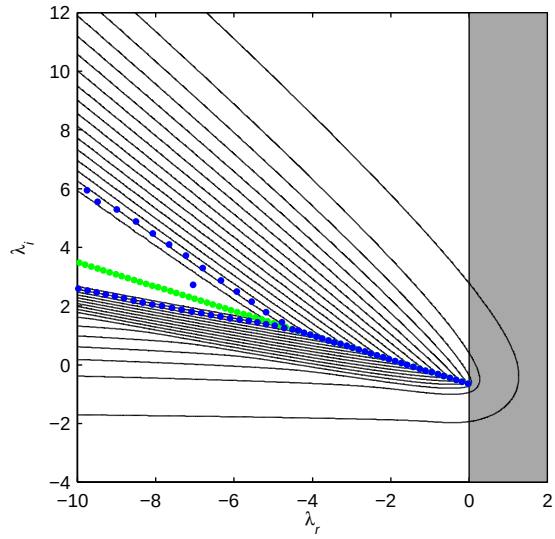

FIGURE 10. Global spectrum of the subcritical Ginzburg-Landau equation (see Table 1), where all the eigenvalues (blue dots) are in the stable half-plane. The unstable domain is in gray and the exact global spectrum is indicated in green. The numerically computed global eigenvalues (blue dots) exhibit a characteristic split, aligning with the resolvent contour that approximately represents machine precision. The resolvent norm contours range from 10^{-1} to 10^{15}.

the bifurcation parameter μ_0 of the Ginzburg-Landau equation is larger than the threshold μ_c. A local analysis confirms an absolutely unstable region since $\mu_c > \mu_t$ in (12) with μ_t as the threshold for a local absolute instability (given by equation (7)). For more details on how the absolutely unstable region acts as a "wavemaker" that sheds waves in the downstream and upstream direction, see Chomaz (2005). Here, we will simply state the fact that linear local stability theory can predict the occurrence of unstable global modes and provide an estimate of the frequency at which these modes oscillate. The Karman vortex street behind a circular cylinder is a generic supercritical flow configuration, and a global and local analysis of the cylinder wake can be found in Pier (2002) and Giannetti & Luchini (2007). It was first shown Provansal *et al.* (1987) that the transition in a wake behind a cylinder close to the critical Reynolds number is described by the Landau equation, *i.e.* the nonlinear Ginzburg-Landau equation without diffusion term. Since then, the Ginzburg-Landau equation (often in its nonlinear form) has been used extensively to model cylinder wakes, see Albarède & Monkewitz (1992); Monkewitz *et al.* (1996); Roussopoulos & Monkewitz (1996); Lauga & Bewley (2004); Cohen *et al.* (2005). Other globally

unstable flow examples that have been investigated as to their self-sustained oscillatory behavior are, among others, hot jets (Lesshafft *et al.* 2006; Nichols *et al.* 2007) and a separated boundary layer flow over a bump (Marquillie & Ehrenstein 2002).

The second model is known as the subcritical case and describes the behavior of disturbances in convectively unstable flows (figure 6). As a result of the non-normality of $\mathcal{A}$, a global analysis reveals the presence of transient energy growth (figure 6b) which cannot be captured by considering individual eigenmodes of the operator $\mathcal{A}$. Instead, one has to consider a superposition of global modes or the norm of the exponential matrix to accurately describe this short-term phenomenon. Transient growth is observed for the Ginzburg-Landau equation when $0 < \mu_0 < \mu_c$. A local analysis shows that this corresponds to a region where the flow is convectively unstable. The wavepacket in figure 6 travels with a group velocity (U_{max}) composed of a dominant wave (c_u) which is associated with the local dispersion relation (3) analyzed in section 2.1. Prototypical convectively unstable flow configurations contain, among others, the boundary layer on a flat plate (Ehrenstein & Gallaire 2005; Åkervik *et al.* 2008), homogeneous jets and mixing layers (Ho & Huerre 1984).

The Ginzburg-Landau parameters $\{\nu, \mu_0, \mu_2, \gamma\}$ for modeling the linear stability of a subcritical or supercritical flow are listed in Table 1. The critical value which delineates the two scenarios is $\mu_c = 0.4$.

3. Input-output behavior

Input-output analysis is a type of analysis of linear systems that is commonplace in systems theory (Kailath 1980). It is concerned with the general response behavior to various excitations of the linear system. In its generality, it goes beyond the concept of classical stability theory commonly practiced in fluid dynamics, as it is not only concerned with issues of stability (*i.e.*, the response to various initial conditions), but also with the short-term dynamics, the response to external (deterministic or stochastic) excitations and the influence of uncertainties in the underlying system (Jovanovic & Bamieh 2005; Schmid 2007). As such, it is thought of as an extension of stability analysis and helps reveal a more complete picture of the behavior of disturbances governed by the linear system.

The temporal response of the Ginzburg-Landau equation to initial conditions (both short-term transient and long-term asymptotic) has been considered in the previous section. In this section, we recast the Ginzburg-Landau model into an input-output framework. The analysis is applied to the convectively unstable case only, since these types of flows are sensitive to forcing and act as noise amplifiers (Huerre 2000). Globally unstable flows behave as *flow oscillators* with a well-defined frequency that is rather insensitive to external forcing.

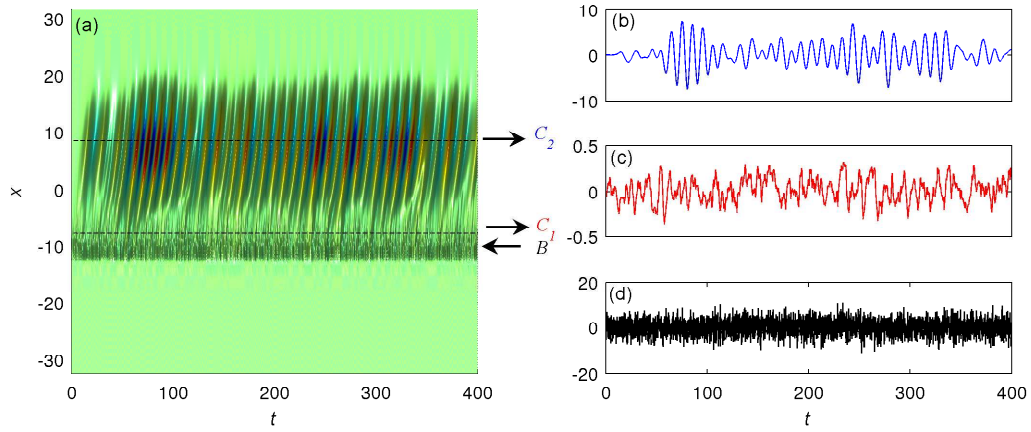

FIGURE 11. Example of the input-output behavior of the Ginzburg-Landau equation with one input and two outputs. In (a) the evolution in space and time of the state when forced by random noise is shown. The region between the dashed lines is convectively unstable. The locations of the forcing B ($x = -11$), the first output C_1 (at branch I) and the second output C_2 (at branch II) are marked by arrows. In (b) and (c) the output signals $y_1 = C_1 q$ and $y_2 = C_2 q$ and in (d) the input signal u are shown. Note that, in (c) the amplitude of the output signal y_1 is less than one, but further downstream in (b), the second output signal y_2 has an amplitude close to 10. This illustrates the amplifying behavior of the system.

This framework will build the foundation for the subsequent design of control schemes, since it allows the quantitative description of the open-loop dynamics, *i.e.* the response to, for example, excitation in the free-stream or to blowing/suction at the wall. We will denote the input sources by $u(t)$ and the measured outputs by $y(t)$. In many realistic flow cases, the output $y(t)$ will only be a subset of the state variable $q(t)$. For example, only shear or pressure measurements at the wall (or another specific location) will be available.

The common format for an input-output analysis is given by the state-space formulation

$$\dot{q}(t) = Aq(t) + Bu(t) \tag{24a}$$
$$y(t) = Cq(t) \tag{24b}$$
$$q(0) = q_0 \tag{24c}$$

where A represents the discrete Ginzburg-Landau operator, the matrices B and C govern the type and location of the inputs $u(t)$ and outputs $y(t)$, respectively, and q_0 stands for the initial condition. For the state-space formulation of the

linearized incompressible Navier–Stokes equations see Farrell & Ioannou (1993) and Jovanovic & Bamieh (2005).

The continuous equations are discretized in space using a spectral Hermite collocation method described in Appendix A. The inputs $B = \{B_1, \ldots, B_p\}$ and outputs $C = \{C_1, \ldots, C_r\}^H$ have spatial distributions of the form of Gaussian functions given by equation (108). In what follows, we will formulate and present results based on matrices and the *discrete* Ginzburg-Landau operator A.

The corresponding adjoint state-space equations of (24) describing the evolution of adjoint state variable $r(t)$ can be written as (van der Schaft 1991)

$$\dot{r}(t) = A^+ r(t) + C^+ v(t) \tag{25a}$$
$$z(t) = B^+ r(t) \tag{25b}$$
$$r(0) = r_0. \tag{25c}$$

The discrete adjoint matrices are not simply the complex conjugate transpose (in other words, $(A^+, B^+, C^+) \neq (A^H, B^H, C^H)$), unless the inner-product used to derive the adjoint operator (14) has an associated weight M which is unity. For the more general case, $M \neq I$, we have

$$A^+ = M^{-1} A^H M, \tag{26a}$$
$$B^+ = B^H M, \tag{26b}$$
$$C^+ = M^{-1} C^H, \tag{26c}$$

where M is a positive-definite and Hermitian weight-matrix. In this work, M is chosen such that the inner-product produces the energy of the state variable (see Appendix A).

The system of equations (24) has the formal solution

$$y(t) = Ce^{At} q_0 + C \int_0^t e^{A(t-\tau)} B u(\tau)\, d\tau \tag{27}$$

where we identify the first part of the right-hand side with the homogeneous solution and the second part with the particular solution stemming from the forcing term Bu. Having covered the homogeneous solution (for $C = I$) in detail in the previous section, we now turn our attention to the particular solution. Setting $q_0 = 0$ leaves us with the input-output relation

$$y(t) = C \int_0^t e^{A(t-\tau)} B u(\tau)\, d\tau \tag{28}$$

from which we will develop tools to capture and characterize aspects of the transfer behavior of an input signal $u(t)$ as it is passes through the linear system given by A.

Before analyzing the above input-output relation in all generality, a first simple numerical experiment shall demonstrate the response behavior of the convectively unstable Ginzburg-Landau equation (see figure 11). As an input signal $u(t)$ we choose white noise — drawn from a normal distribution with

zero mean and unit variance — introduced at a location just upstream of the unstable region; the corresponding response $y(t) = Cq(t)$ is extracted at the two boundaries of the unstable domain, *i.e.*, at branch I and II. A first observation confirms the amplification of the signal as it traverses the unstable domain as well as the emergence of a distinct frequency from the noisy input. The system, thus, seems to act as both a noise amplifier (Huerre & Monkewitz 1990) and a filter. These two characteristics will be analyzed in more detail below.

3.1. *Impulsive and harmonic forcing*

The above introductory example has shed some light on the response behavior of the Ginzburg-Landau equations to external forcing. Even though the signal has demonstrated amplification and frequency selection of the linear system, a more general analysis is pursued that parameterizes the input-output behavior more precisely.

For this reason, we will consider two distinct input signals: an impulsive signal applied at a specified location $x_w = -11$ which will trigger what is referred to as the impulse response, and a harmonic signal, again applied at a given location, that yields the frequency response of the linear system.

For the impulse response we thus assume

$$u(t) = \delta(t) \tag{29}$$

which, according to (28), results in

$$y(t) = Ce^{At}B = g(t). \tag{30}$$

The spatial localization of the impulsive input signal is contained in the matrix B (see equation (108a)). For $C = I$, the above solution (30) represents the Green's function of the Ginzburg-Landau equation. It forms the fundamental solution of the linear system since particular solutions to more general external excitations can be constructed by a simple convolution of the input signal with the Green's function. The input-output system (24) is defined as stable if and only if the impulse response (30) decays as time tends to infinity. Consequently, the convectively unstable flow is input-output stable, which is in contrast to the globally unstable flow where an impulse will trigger the growth of an unstable global mode with a well defined frequency. For the convectively unstable case, the state impulse response $q(t) = e^{At}B$ for a pulse introduced at $x_w = -11$ is displayed in figure 12a; the impulse response (30) is shown in figure 12b. We observe the rise of a wavepacket with a distinct spatial wavenumber and propagation speed. As expected from the introductory example (figure 5), the amplitude of the wavepacket grows throughout the unstable domain before it decays as the wavepacket passes branch II. For larger times, only the remnants of the wavepacket near branch II are observed.

The impulsive signal $u(t) = \delta(t)$ contains all temporal frequencies with equal amplitude. It is thus ideally suited to extract and analyze a frequency selection behavior from an unbiased input. On the other hand, we could choose

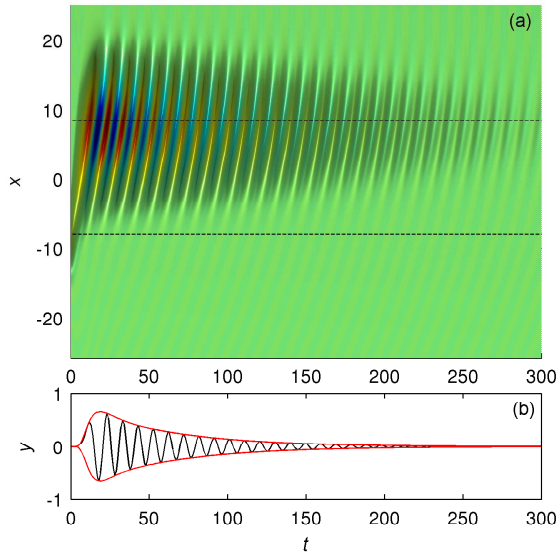

FIGURE 12. Impulse response of the Ginzburg-Landau equation: (a) The state response to an impulse introduced at $t = 0$ and $x_w = -11$. (b) The impulse response at branch II. The convective character of the instability is evident: a wavepacket grows as it enters the unstable domain, but is gradually convected away from this domain before it begins to decay.

an input signal with only one frequency (rather than all frequencies), *i.e.*

$$u(t) = e^{st} \qquad s \in \mathbb{C}. \tag{31}$$

Inserting the above input into (28), assuming A is globally stable and $t = \infty$ yields

$$\begin{aligned} y(t) \quad &= \int_0^\infty g(\tau) e^{s(t-\tau)}\, d\tau = \\ &= \underbrace{\int_0^\infty g(\tau) e^{-s\tau}\, d\tau}_{G(s)}\, e^{st} = |G(s)| e^{(st+\phi)}. \end{aligned} \tag{32}$$

We can identify the transfer matrix of dimension $r \times p$

$$G(s) = C(sI - A)^{-1}B \qquad s \in \mathbb{C}, \tag{33}$$

as the Laplace transform of the impulse response $g(t)$. Due to the linear nature of the Ginzburg-Landau equation an input e^{st} will generate an output with the same frequency but with a phase shift $\phi = \text{Arg}\, G(s)$ and an amplitude of $|G(s)|$. Since $G(s)$ is usually a rectangular matrix, the amplitude is defined as

$$|G(s)| = \sigma_1, \tag{34}$$

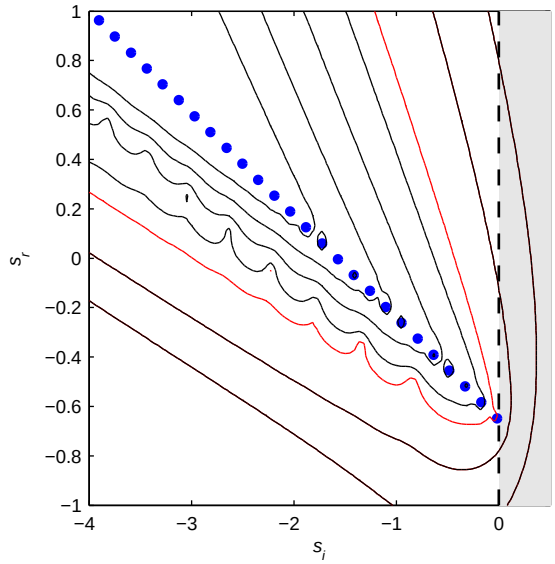

FIGURE 13. Input-output pseudospectra where the black transfer function contour levels are $\{10^0, 10^1, 10^3, 10^4, 10^5, 10^6\}$. The red contour (with level 208) represents the largest contour value that crosses the imaginary axis. The blue symbols indicate the eigenvalues of A.

where $\sigma_1\{\cdot\}$ denotes the largest singular value of $G(s)$. The transfer function $G(s)$ fully describes the input-output behavior of the system, whereas the state-space formulation (24) describes the dynamics of flow.

The transfer function can be regarded as a generalization of the resolvent (22) introduced earlier. In fact, the pseudospectra in figure 10 are contours of $|G(s)|$ for the case $B = I$ which corresponds to a uniform distribution of the input and $C = F$ (where $M = F^H F$) which corresponds to the measurement of the flow energy. As discussed in section 2.4, the contours represent locations in the complex plane where approximate eigenvalues of A can be found for a given error norm ($\epsilon = 1/|G(s)|$). Figure 13 displays pseudospectra of the input-output system with B defined as in (108) and $C = F$. In this case, the contour levels correspond to the response amplitude of the output for a unit amplitude input of the form e^{st}.

As an example, we will concentrate on a purely harmonic forcing and set $s = i\omega$. The response of the linear system to this type of excitation is given by the expression

$$G(i\omega) = C(i\omega I - A)^{-1}B \qquad \omega \in \mathbb{R}, \tag{35}$$

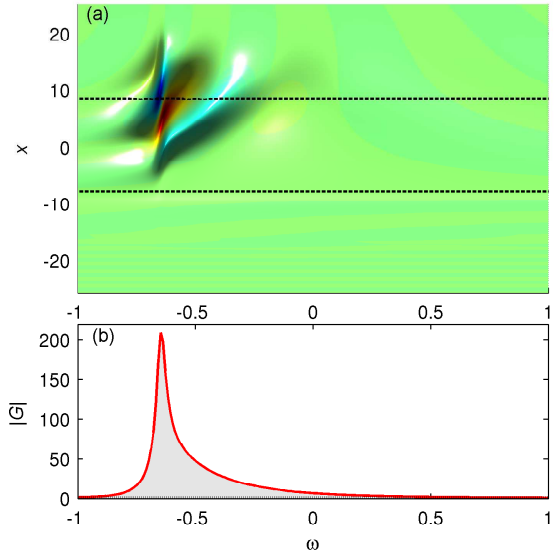

FIGURE 14. (a) The state response to harmonic forcing located upstream of branch I (lower of the two dashed lines). The largest response is at branch II (upper dashed line) for $\omega = -0.65$. (b) The frequency response, where the output is a Gaussian function (see Appendix A) located at branch II. In the gray area all forcing frequencies are amplified in the unstable domain, all other frequencies are damped illustrating a filtering effect. This response corresponds to the thick dashed line representing the imaginary axis in the pseudospectra plot in figure 13, and the peak value $\|G\|_\infty = 208$ corresponds to the red contour level.

and the largest response to a harmonic input can be defined as the maximum value of $|G(i\omega)|$,

$$\|G\|_\infty = \max_\omega |G(i\omega)|. \tag{36}$$

A remark on the choice of notation seems necessary: in the stability section, we defined the energy norm of the state vector $q(t)$ as $\|q\|_M^2 = q^H M q$, whereas the definition (36) of $\|G\|_\infty$ represents a norm of all stable transfer functions in the complex frequency space.

For normal systems the largest response to harmonic forcing is proportional to the distance of the real part of the largest eigenvalue of A to the imaginary axis, *i.e.*,

$$\|G\|_\infty \sim 1/|\mathrm{Re}(\lambda_1)|. \tag{37}$$

For non-normal systems, however, the response of the system can be substantial even though the forcing frequency is nowhere close to an eigenvalue. The largest

response $\|G\|_\infty$, in this case, is proportional to the largest value of the contour $|G(s)|$ that crosses the imaginary axis.

This feature is exemplified on the Ginzburg-Landau equation in figure 13 and 14. The state response (*i.e.*, the special case with $C = I$) to spatially localized, harmonic forcing at $x_w = -11$ is shown in figure 14a. The largest response is obtained for a frequency of $\omega = -0.65$, and the location of the most amplified response in space is — not surprisingly — in the vicinity of branch II. In figure 14b the frequency response $|G(i\omega)|$ is shown which corresponds to the dashed line in the contour plot of figure 13. The peak of this response $\|G_c\|_\infty = 208$ is associated with the red contour in the pseudospectra plot (figure 13). The response computed from the distance to the nearest eigenvalue (37) has a value of only 56. It is thus confirmed that the frequency response for non-normal systems is substantially larger than what can be inferred from the distance of the forcing frequency to the nearest eigenvalue.

3.2. *Stochastic forcing*

Under realistic conditions we rarely possess the exact knowledge of the disturbances influencing the flow system, and it is therefore essential to account for a certain amount of uncertainty. In this section we present fundamental techniques to characterize the response behavior within a statistical framework. This framework also gives insight into inherent stability properties of the flow (Hœpffner 2006; Schmid 2007), as for example in the case of channel flow studied by Farrell & Ioannou (1993); Bamieh & Dahleh (2001); Jovanovic & Bamieh (2005) and boundary layer Hœpffner & Brandt (2008). When a fluid system is externally excited by stochastic disturbances, its response is best characterized by the state statistics, for instance, the *rms* values of the velocity components, the mean energy, or two-point correlations. In the context of aerodynamic flows, stochastic excitation can be attributed, among others, to free-stream turbulence, wall roughness, or incident acoustic waves.

A naive statistical analysis may consist of performing a large number of simulations by choosing sample realizations of the forcing and by subsequent averaging of the resulting flow quantities to obtain the desired statistics. A more direct approach involves the derivation of evolution equations for the statistical properties, such as *e.g.* two-point correlations, of the flow quantities. For linear systems it is possible to solve directly for the two-point correlations of the flow quantities in terms of the two-point correlations of the external excitation. The key equation relating second-order statistics of the excitation to second-order statistics of the state is the Lyapunov equation. In this section we will derive the Lyapunov equation and give examples of how to extract relevant information from its solution.

An introductory example can be seen in figure 15a where the temporal evolution of the state energy is displayed as a random forcing with zero mean and unit variance applied upstream of branch I. The results of five simulations are shown. Due to the stochastic nature of the forcing each simulation yields

different results but, nevertheless, reveals a general trend: no energy is observed at the beginning of each simulation (since the initial condition is identically zero), but considerable energy levels are reached after an initial transient of approximately 100 time units and a quasi-steady regime in which the energy fluctuates about a mean value is established. Because of this observed noise amplification, convective unstable flows are also referred to as noise amplifiers. Furthermore, the dashed line shows the average of 50 simulations, representing the evolution of the mean energy. This curve is compared to the mean energy (red solid line) computed from the algebraic Lyapunov equation; this mean energy level is increasingly better approached as the number of simulations comprising the average is increased.

Although the above experiment already demonstrates the amplification behavior of a convectively unstable linear system driven by stochastic forcing, the relation between the forcing covariance and the resulting state covariance will be established next.

We again consider the linear system given by equation (24), now driven by a stochastic process $u(t)$, *i.e.* a random time-varying input signal. We assume that A is globally stable but convectively unstable. To simplify the analysis, we also assume that the random variable u is normally distributed, *i.e.*, that the probability density function of the stochastic process is Gaussian, completely characterized by its mean and its variance.

To represent the mean and the variance of a random variable, we introduce the expectation operator $\mathcal{E}$. The mean of a scalar random variable ξ is then $m = \mathcal{E}\{\xi\}$, its variance is the quadratic expression $\sigma = \mathcal{E}\{\xi\xi^H\}$. From a statistical point of view, $\mathcal{E}$ can be thought of as an averaging operator (for example the action of an integral in time.)

We can similarly characterize the covariance of two random variables ξ and η as $P_{\xi\eta} = \mathcal{E}\{\xi\eta^H\}$. The covariance of two random variables gives information about the degree of similarity of the two signals. The above definition of the covariance is readily extended to vectors of random variables. The covariance of two random vector variables $f(t)$ and $g(t)$ of dimension n is simply the $n \times n$ matrix,

$$P_{fg}(t) = \mathcal{E}\{f(t)g(t)^H M\}. \tag{38}$$

Using the energy weight matrix M, we recover the kinetic energy of a state by simply taking the trace of the covariance matrix,

$$E(t) = \mathcal{E}\{\mathrm{trace}(q(t)q(t)^H M)\} = \mathrm{trace}(P_{qq}). \tag{39}$$

Furthermore, the diagonal elements of P_{qq} are the variance of the individual elements of $q(t)$. In particular, we define the root-mean-square (rms-value) of the disturbance as

$$q_{rms}(t) = \sqrt{\mathrm{diag}\{P_{qq}\}} \tag{40}$$

From the above equations (39) and (40), it is clear that the covariance of the state contains all the essential statistics that is necessary for evaluating the response to stochastic forcing. We now return to our dynamical system

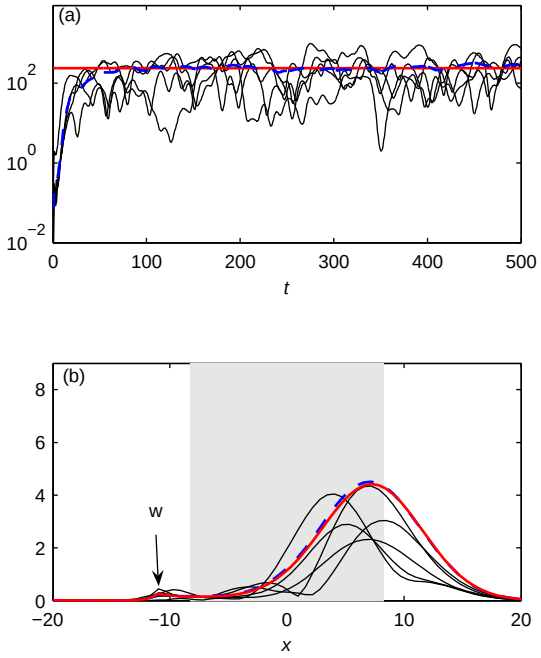

FIGURE 15. The response to stochastic forcing. (a) The evolution of the state energy for five different simulations (black lines), the mean state energy given by the solution of the algebraic Lyapunov equation (red solid line) and the energy averaged over 50 simulations (thick dashed line). (b) The thick red line shows the rms-value of the Ginzburg-Landau equation when excited by random forcing w at the location marked with an arrow. Five representative snapshots of the response to this forcing are shown by black thin lines; the average over 50 simulations is displayed by a thick blue dashed line.

(24) and derive an explicit expression of the state covariance in terms of the forcing covariance. For simplicity, we will assume that the applied forcing is uncorrelated in time, that is, it is a temporal white noise process:

$$\mathcal{E}\{u(t)u(t')^H M\} = WM\delta(t-t') \tag{41}$$

where t and t' are two instances in time, and W denotes the spatial covariance of u. For example, if u is a vector of random variables, $W_{ij} = \mathcal{E}\{u_i {u_j}^H\}$.

To derive an evolution equation for the covariance of the state, we start with the expression describing the time evolution of the state forced by u (*i.e.*

equation (28) with $C = I$),

$$q(t) = \int_0^t \mathrm{e}^{A(t-t')} B u(t') \mathrm{d}t'. \tag{42}$$

As before, we have assumed a zero initial condition $q_0 = 0$.

We begin with the definition of the covariance matrix P_{qq} of the state at time t

$$\begin{aligned} P &= \mathcal{E}\{q(t)q(t)^H M\} \\ &= \int_0^t\int_0^t e^{A(t-t')} B \underbrace{\mathcal{E}\{u(t')u(t'')^H M\}}_{WM\delta(t'-t'')} B^H e^{A^H(t-t'')} \mathrm{d}t'\mathrm{d}t'' \\ &= \int_0^t e^{A(t-t')} BWB^+ e^{A^+(t-t')} \mathrm{d}t' \end{aligned} \tag{43}$$

where we have used the fact that u is uncorrelated in time and omitted the subscript $_{qq}$. We can differentiate this last expression in (43) with respect to time to obtain an evolution equation for P of the form

$$\dot{P} = AP + PA^+ + BWB^+ \qquad P(0) = 0. \tag{44}$$

In this expression $\dot{P}$ denotes the time derivative of the covariance matrix. The above equation is referred to as a differential Lyapunov equation. Given the covariance W of the forcing term u, we obtain the time evolution of the state covariance P. If the system A is asymptotically stable and, furthermore, A, W and B are time-independent, the stochastically driven system relaxes after an initial transient into a statistical steady state. To obtain this steady state, we set $\dot{P} = 0$ and recover the algebraic Lyapunov equation

$$AP + PA^+ + BWB^+ = 0. \tag{45}$$

This statistical steady state is of interest if we study a system that is exposed to external forcing for a long time horizon, *e.g.*, the flow over a wing under cruise conditions. We like to emphasize that despite the presence of a steady statistical state, the state vector of the system as well as the external forcing is varying in time.

To illustrate the above statistical description of the system dynamics, we revisit the Ginzburg-Landau equation forced at the upstream edge of the convectively unstable region where we apply the external excitation of Gaussian form shown in equation (108a), with $u(t)$ as a scalar white noise process with zero mean and unit variance $W = 1$. The covariance of the state obtained by solving the algebraic Lyapunov equation (Datta 2003) is depicted in figure 16. The rms-value of this state-covariance is shown with a red line in figure 15b and the gray area marks the region of convective instability. In addition, we have represented the instantaneous state of five realizations of the forcing as well as the mean of 50 of these realizations, as we did in figure 15a for the total energy evolution in time. We see that the average of 50 realizations is close to the mean obtained from the Lyapunov equation, but a sample set of

50 realization is not yet enough for a converged statistical result. We will see more examples of this kind in the control section where we will quantify the performance of the controller using mean energy.

We conclude this section by stressing that transient growth mechanisms in hydrodynamic stability theory as well as the spatio-temporal evolution of disturbances can be recast into an input-output framework. For example, in this framework, the output signal $y(t)$ to random, impulsive or harmonic inputs shown in figures 11, 12 and 14, respectively, exhibits an initial growth in time before the signal either decays to zero or stabilizes around a steady state.

3.3. *Controllability and observability*

An important issue in the analysis of linear systems in state-space form concerns the mapping between input signals and the state vector and between the state vector and the output signals. Since for many realistic configurations the matrices B and C are rectangular, reflecting the fact that we force the system only at a few points in space and/or measure the system only at a limited number of sensors, we need to address the topic of controllability and observability (Kailath 1980).

In this section we will characterize the controllability and observability of a system in terms of covariance matrices of the state and the adjoint state, which in this context are called *Gramians*. We will continue to consider one input and one output and assume that A is stable (subcritical Ginzburg-Landau equation), even though the theory extends to unstable systems as well (Zhou *et al.* 1999).

3.3.1. *Controllability — the POD modes*

The controllability of a system is concerned with finding the flow states most easily influenced by a given input. It can be shown (Lewis & Syrmos 1995; Antoulas 2005) that the minimum amount of input energy $\|u\|_2^2$ to bring the state from zero to the given initial condition q_0 is given by the expression

$$q_0^H P^{-1} q_0 \tag{46}$$

where P is the unique $n \times n$ matrix

$$P = \int_0^\infty e^{A\tau} B B^+ e^{A^+\tau} \, d\tau, \tag{47}$$

referred to as the *controllability Gramian* (for a derivation of this result in terms of an optimal control problem see Lewis & Syrmos (1995).) Also note that the adjoint operators with superscript $^+$ are related to the conjugate transpose ^{H} according to (26).

Since for linear systems the state for an impulsive input at any given time is $q(t) = e^{At}B$, we recognize that the controllability Gramian (47) equals an infinite-horizon state covariance (43) with covariance $W = I$. This is not very surprising since one can interpret white noise as a set of impulse inputs that

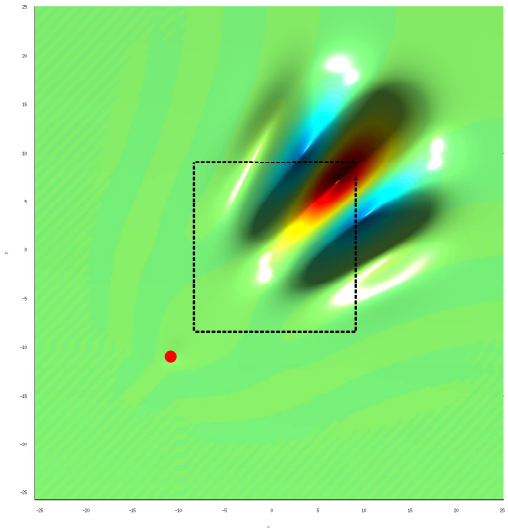

FIGURE 16. The state covariance/controllability Gramian P of the Ginzburg-Landau equation. The Gramian describing how the state components are influenced by an input corresponds in a stochastic framework to the state covariance for white noise as input. The red circle signifies the forcing location ($x_w = -11$), the dashed box marks the region of instability. The states that are most sensitive to forcing, and thus controllable, are located downstream, at branch II.

are uncorrelated in time. Furthermore, assuming A is stable, the controllability Gramian can be computed by solving the algebraic Lyapunov equation (45). In figure 16 the controllability matrix of the Ginzburg-Landau equation is shown graphically. The state components that respond to an input located just upstream of the unstable region are situated downstream of the unstable domain.

By diagonalizing the matrix P we obtain a measure of controllability for each component of the state vector. The diagonalization of the covariance matrix or, in the linear framework, the controllability Gramian is commonly referred to as the proper orthogonal decomposition (POD) (Lumley 1970) but is also known as empirical eigenfunction (EOF) decomposition, Karhunen-Loève decomposition or principal component analysis (PCA). The eigenvectors and eigenvalues of P are given by

$$P\phi_i = \lambda_i \phi_i, \qquad \lambda_1 \geq \cdots \geq \lambda_n \geq 0. \tag{48}$$

Since P is positive semidefinite, the eigenvalues are real and positive and the eigenvectors are orthogonal. The first two POD modes of the Ginzburg-Landau equation are shown in figure 17. Traditionally, the interpretation of these modes is that they represent decorrelated energy-ranked flow states. For example,

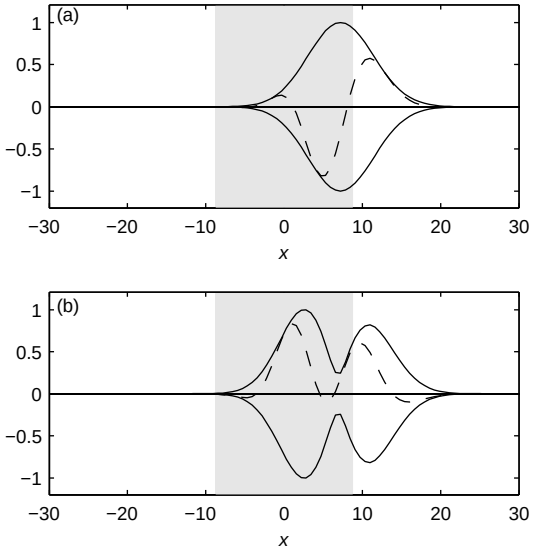

FIGURE 17. The first (a) and second (b) proper orthogonal decomposition (POD) mode obtained from an eigenvalue decomposition of the controllability Gramian in figure 16. Note that these modes are orthogonal. The absolute value is shown in solid and real part in dashed. The gray area marks the region of instability.

the first POD mode ϕ_1 is the most energetic structure in the flow containing $\lambda_1 / \sum_{i=1}^{n} \lambda_i$ of the total flow energy. From a linear systems point of view, POD modes can be considered as the most controllable structures of the system for a given input. In this case the eigenvalue λ_i is a measure of how much the state ϕ_i is influenced by the input. In particular, if P is rank deficient, there exists a zero eigenvalue, $\lambda_i = 0$, which would mean according to equation (46) that the energy required to influence the corresponding state is infinite. If P is not rank-deficient, we say that (A, B) is controllable.

3.3.2. *Observability — the adjoint POD modes*

The POD modes capture the response to input and thus span a controllable subspace of the state-space. Equally important in the input-output analysis is to take into account the observable subspace by considering the relation between the outputs and flow states. A similar analysis as in the previous section for POD modes is thus performed, but this time for the adjoint system (25). Comparing the direct state-space equations (24) with their corresponding adjoint state-space equations (25) we observe that the output of the direct equations is related to the input of the adjoint equations.

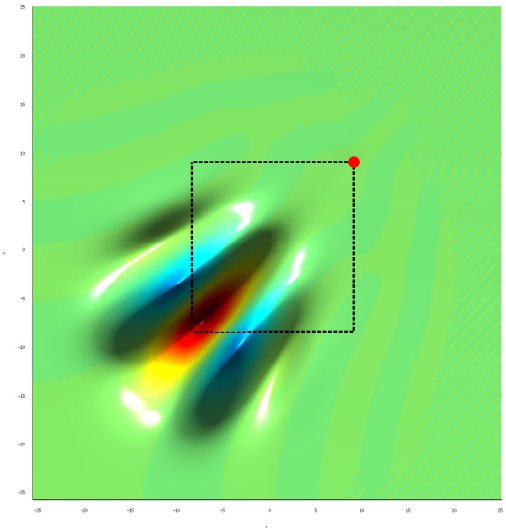

FIGURE 18. The observability Gramian Q of the Ginzburg-Landau equation. The red circle markes the location of the output C at branch II. The initial states that contribute most to the output are located upstream, at branch I.

The observability of a system is concerned with finding the initial conditions q_0 that will produce the largest output energy. For zero input the solution to the state-space equations is

$$y = Ce^{At}q_0. \tag{49}$$

The output energy is then given by

$$\|y\|_2^2 = q_0^H Q q_0 \tag{50}$$

where the *observability Gramian,*

$$Q = \int_0^\infty e^{A^+\tau} C^+ C e^{A\tau}\ d\tau, \tag{51}$$

is a unique matrix of dimension $n \times n$.

If we note that the impulse response of the adjoint state-space equations (25) is given by

$$r(t) = e^{A^+ t} C^+ \tag{52}$$

the observability Gramian can be written as the state correlation matrix of the adjoint system

$$Q = \mathcal{E}\{rr^H M\}, \tag{53}$$

and the Gramian can be computed by solving the algebraic Lyapunov equation

$$A^+ Q + QA + C^+ C = 0. \tag{54a}$$

In figure 18 the observability matrix of the Ginzburg-Landau equation is shown. The observable components of the state vector are located upstream of the unstable domain when the output location is at branch II (red dot in figure 18).

By diagonalizing the observability Gramian,

$$Q\psi_i = \lambda_i \psi_i, \qquad \lambda_1 \geq \cdots \geq \lambda_n \geq 0, \tag{55}$$

we obtain an orthogonal set of functions called the adjoint POD modes or the most observable modes. These modes are flow structures that are ranked according to their contribution to the output energy. The corresponding eigenvalues λ_i provide a means to measure how observable the corresponding eigenvectors are. If there exist zero eigenvalues, $\lambda_i = 0$, Q is rank deficient, which means according to equation (50) that the corresponding adjoint POD mode does not contribute to sensor output. If Q has full rank, we say that (C, A) is observable.

It should be evident that in order to build an effective control system, both sufficient controllability and observability has to be established. Only in this case will the actuation have an appreciable effect on the flow system whose response, in turn, will be detectable by the sensors. Without adequate controllability or observability the flow of information from the system's output to the system's input will be compromised, and any control effort will be futile. Within the LQG-based feedback control framework, the controller will always stabilize the system if the unstable global eigenmodes are both controllable and observable. We will show how the controllability and observability of global eigenmodes can be determined in the next section.

4. Model reduction

Any type of significant flow control applied to the discretized two- or three-dimensional Navier–Stokes equations requires some form of model reduction. Model reduction is concerned with the transformation of a system with a large number of degrees of freedom to an approximately equivalent system of markedly smaller size. The term "approximately equivalent" is often difficult to quantify and usually encompasses a measure of preservation of important system characteristics under the model reduction transformation. In this sense, model reduction becomes problem-dependent: for example, a transformation that preserves the inherent dynamics of the system may be inappropriate in capturing the input-output behavior.

Model reduction techniques for fluid systems typically rely on physical insight into the specific flow situation rather than on a systematic approach detached from the application. For instance, for spatially invariant systems it is possible to decouple the linear state space equations in Fourier space. Control, estimation and other types of optimization can then be performed independently for each wavenumber and then transformed back to physical space. This approach has been adopted in Högberg *et al.* (2003*a*,*b*); Hœpffner *et al.* (2005); Chevalier *et al.* (2006, 2007); Monokrousos *et al.* (2008).

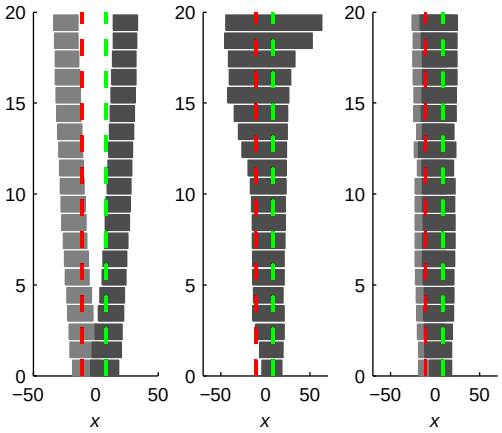

FIGURE 19. The spatial support of the first 20 global (a), POD (b) and balanced modes (c). The spatial support is defined as the region where the amplitude of a particular mode is larger than 2% of its maximum amplitude. The location of the input (just upstream of branch I) and output (at branch II) is marked with red and green dashed lines, respectively. The global modes span only the region around branch II. The first POD modes (b) are located at branch II, even though the higher modes quickly recover the input. The balanced modes (c) cover the region between input and output with only two modes. The areas marked with light gray in (a) and (c) represent the spatial support of the adjoint modes for the global and balanced modes. The spatial separation in x of the direct and adjoint modes, shown in (a) for global modes, is absent in (b) for the balanced modes.

The model reduction (or projection) technique (Obintata & Andersson 2001; Antoulas 2005) discussed in this paper involves three steps.

The first step consists of finding an expansion basis $\{\phi_i\}_{i=1}^{r}$ that spans an appropriate subspace of order r of the state space of order n, with $r \ll n$. We will present and compare three different subspaces using the Ginzburg-Landau equation: the subspace spanned by the least stable global eigenmodes, POD modes and the balanced modes (described in the next section).

In a second step, the state-system given by (24) is projected onto this subspace yielding the reduced-order model

$$\dot{\kappa}(t) = \hat{A}\kappa(t) + \hat{B}u(t) \tag{56a}$$

$$y(t) = \hat{C}\kappa(t) \tag{56b}$$

$$\kappa(0) = \kappa_0. \tag{56c}$$

When the expansion basis is non-orthogonal, we can use a set of adjoint modes $\{\psi_i\}_{i=1}^r$ associated with $\{\phi_i\}_{i=1}^r$, to obtain the entries of κ, $\hat{A}$, $\hat{B}$ and $\hat{C}$,

$$\hat{\kappa}_i = \frac{\langle q, A\phi_i\rangle}{\langle \psi_i, \phi_i\rangle} \tag{57a}$$

$$\hat{A}_{i,j} = \frac{\langle \psi_i, A\phi_j\rangle}{\langle \psi_i, \phi_i\rangle} \tag{57b}$$

$$\hat{B}_i = \frac{\langle \psi_i, B\rangle}{\langle \psi_i, \phi_i\rangle} \tag{57c}$$

$$\hat{C}_i = C\phi_i \tag{57d}$$

with $i, j = 1, \ldots, r$. The term $\langle \psi_i, \phi_i\rangle$ is a normalization factor that we choose such that $\|\phi_n\| = \|\psi_n\| = 1$ and is smaller than one if the modes are non-orthogonal, that is $\psi_i \neq \phi_i$. The subscript M in the above inner products is omitted for brevity and we have assumed that B is a column vector and C a row vector, *i.e.* we continue to consider one input and one output.

The third and final step consists of estimating the error of the reduced order model (56). For control purposes it is not necessary for the reduced-order model to capture the entire dynamics described by the general state-space formulation (24), rather it suffices to accurately capture the input-output behavior described by the transfer function $G(s) = C(sI-A)^{-1}B$. It thus seems reasonable to estimate the error of a reduced-order system by comparing the norms of the transfer function (35) of the full system G and the reduced system $G_r = \hat{C}(sI-\hat{A})^{-1}\hat{B}$, *e.g.* $\|G-G_r\|_\infty$ (Obintata & Andersson 2001; Zhou *et al.* 2002; Green & Limebeer 1995). This is equivalent to calculating the difference of the peak values of the frequency response between the two models.

4.1. *Global modes and input/output residuals*

Global modes (figure 7a,b) preserve the dynamical characteristics of the system matrix A. Model reduction using global modes simply consists of an expansion of the state vector q into the leading global eigenmodes (10), where eigenmodes with substantial decay rates will be neglected. By this process, the resulting new system matrix $\hat{A}$ in (56) will consist of a diagonal matrix of the retained global eigenvalues. The new reduced state vector κ is given by the eigenfunction expansion coefficients, and the expansion coefficients of B (57c) and C (57d) are called the *controllability modal residuals* and the *observability modal residuals,* respectively (see also Bewley & Liu (1998)).

It is clear that if $\langle \psi_i, B\rangle$ is zero in (57c), we will not be able to act on the corresponding state component κ_i and therefore on the global mode ϕ_i. Thus, we can use the controllability modal residual as a measure of controllability of the global mode by considering the amount of overlap between the support of the input and the support of the corresponding adjoint global mode. If this overlap is zero, the global mode is not controllable (Chomaz 2005; Lauga & Bewley 2004).

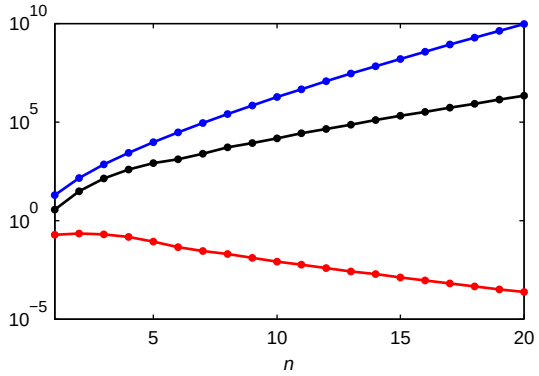

FIGURE 20. The controllability modal residuals (black line) of the first 20 global modes given by equation (57c) which is the product of the overlap of the actuator and adjoint mode $\langle \psi_i, B \rangle$ (red) and the sensitivity defined by $(\langle \psi_i, \phi_i \rangle)^{-1}$ (blue). Although, the overlap of the spatial support of the actuator decreases for higher modes, the controllability still increases due to the rapid growth of the receptivity of higher modes to forcing, quantified by the inverse of $\langle \psi_i, \phi_i \rangle$.

A similar derivation based on (57d) shows that in order for (C, A) to be observable, the spatial support of the sensor and the support of the global mode must overlap. If $\hat{C}_i = C\phi_i$ is zero, we will not be able to detect the eigenmode ϕ_i using a sensor characterized by C. This eigenmode is thus unobservable.

Owing to the term $\langle \psi_i, \phi_i \rangle$ in the denominator of (57c), additional attention has to be paid to the system's sensitivity due to non-normal effects: the forcing response or controllability of ϕ_i is inversely proportional to $\langle \psi_i, \phi_i \rangle$, *i.e.* the separation of global and adjoint modes. This separation is illustrated in figure 19a, where the spatial support — defined as the region where the amplitude of a particular mode is larger than 2% of its maximum amplitude (see also Lauga & Bewley (2003)) — of the first 20 global and adjoint modes is shown. We see that the global modes only span a small part of the domain, which is located near and downstream of the unstable domain (green dashed line), whereas the corresponding adjoint modes are located upstream of the unstable domain (red dashed line); this results in a large sensitivity, $\langle \psi_i, \phi_i \rangle \ll 1$.

In figure 20 we display the controllability as the number of global modes is increased, together with the numerator and denominator of expression (57c). Whereas the numerator represents a measure of overlap between the input and the adjoint global modes, the denominator measures the degree of non-normality. The marked rise in controllability as more global modes are added

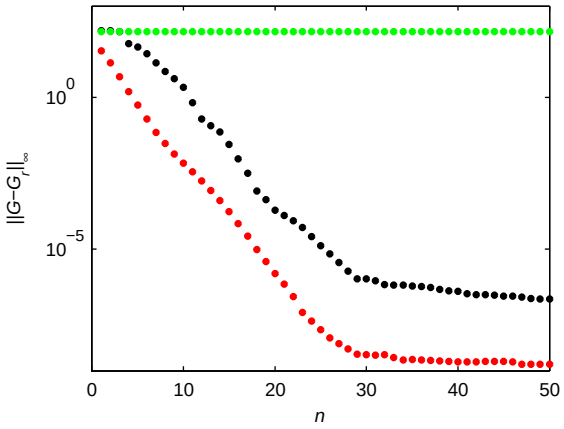

FIGURE 21. Model reduction error of the POD (black), balanced (red) and global (green) modes. For the balanced modes the error always decays by increasing the number of modes, in contrast to the error of POD modes. The error does not decay at all for the first 50 global modes due to the failure to project the input B located upstream of branch I onto the global eigenmodes located close and downstream to branch II.

is thus a compound effect of these two components. It illustrates that non-normal systems can be very sensitive to the external perturbation environment and that it is possible to manipulate the flow using very small actuator effort.

An upper limit of the error for reduced-order models based on global modes is given by (Skogestad & Postlethwaite 2005; Antoulas 2005)

$$\|G - G_r\|_\infty \leq \sum_{i=r+1}^{n} \frac{|\hat{C}_i \hat{B}_i|}{|\mathrm{Re}(\lambda_i)|}. \tag{58}$$

From the above expression it is evident that choosing a subspace based on the criterion of dominant eigenvalues may not be appropriate if one wishes to approximate the input-output behavior. The reason is that the error norm (58) depends on the matrices B and C. Although the eigenvalues may exhibit substantial decay, for highly non-normal systems $\hat{B}$ is large yielding a large model reduction error as shown in figure 21 using green circles.

In figure 22 we compare the frequency response of the full model $|G(i\omega)|$ of order $r = 220$ (blue dashed line) to the frequency response of the reduced models $|G_r(i\omega)|$ of order $r = 2, 4$ and 6 (green solid line). As before, the input B (at branch I) is located upstream and the output C (at branch II) downstream. The frequency response of the reduced models shows a large deviation from the true frequency response, even as the number of included modes is increased.

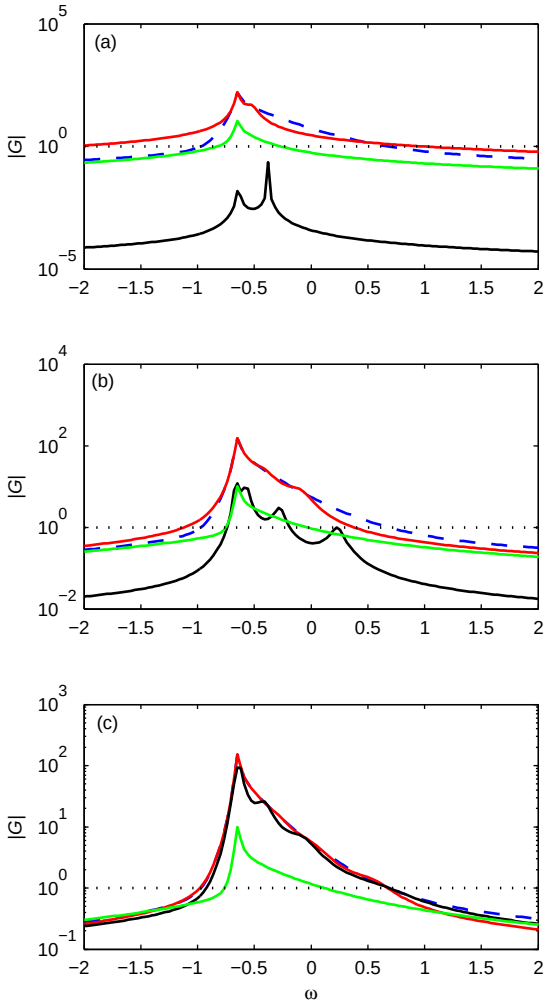

FIGURE 22. Comparison of the frequency response of the full Ginzburg-Landau equation with three reduced-order models. Blue dashed lines represent the full model of order $n = 220$. The performance of reduced-order models based on $r = 2, 4$ and 6 modes are shown in the (a), (b) and (c), respectively. Red lines represent the balanced modes, black lines the POD modes and green lines the global eigenmodes. We observe that the balanced modes capture the peak value of the frequency response which represents the main characteristic of the input-output behavior. The approximation of the frequency response for the open-loop case is unsatisfactory for POD models of order 2 and 4 and for all global-mode models.

4.2. *POD modes*

For an improved transfer behavior of the reduced model we can base our subspace on the response of the linear system to external forcing. In this case, both the system matrix A and the control matrix B determine the dynamics of the driven system. To reduce a driven model, we will expand the state vector into the POD modes (31) (figure 17). The expansion in POD modes will be truncated at a convenient level that results in a significantly lower-dimensional system matrix but still retains the most energetic structures. These modes are ideal in detecting and extracting coherent fluid structures in a hierarchical manner that is based on their contribution to the overall perturbation energy of the flow. However, for control and input-output behavior low-energy features that are not captured by this expansion may be critically important.

We like to point out that the controllable subspace adequately spans the *response* to inputs but not necessarily the inputs themselves. This is illustrated in figure 19b, where the spatial support of the first 20 POD modes are shown. The first POD modes capture the largest structures, located at branch II; however, in contrast to the global modes, the higher modes eventually cover the entire unstable domain including our input location. For this reason the error norm shown with black circles in figure 21 is not decreasing for the first three POD-modes; only when the fourth mode, which captures some of the input structure, is included in the expansion basis does the error norm begin to decrease. An explicit error estimate does not exist for POD modes; only after computing the frequency response of the two systems can one determine the error (given by the difference of the peak values in the frequency response).

Finally, in figure 22 the frequency response of the POD-based reduced model (black line) $|G_r(i\omega)|$ of order $r = 2, 4$ and 6 is observed to gradually approach the response of the full model.

4.3. *Balanced modes*

The third subspace is based on *balancing* the system and involves the three matrices A, B and C. It is based on the idea of reducing the dimensions of the original system by (i) removing the redundant states for characterizing the input-output behavior — the uncontrollable and unobservable states — and (ii) removing the states that are nearly uncontrollable and unobservable. This technique of model reduction is referred to as balanced truncation (Moore 1981).

The balanced modes $\{\phi_i\}_{i=1}^r$ are defined as the eigenvectors of the product of the two Gramians,

$$PQ\phi_i = \phi_i\sigma_i^2, \qquad \sigma_1 \geq \cdots \geq \sigma_r \geq 0. \tag{59}$$

The eigenvalues σ_i are called the Hankel singular values (HSV). First two balanced modes are shown in figure 23.

To illustrate what *balancing* refers to, let us consider the projection of the Gramian matrices P and Q on a set of modes, for instance any of the modes

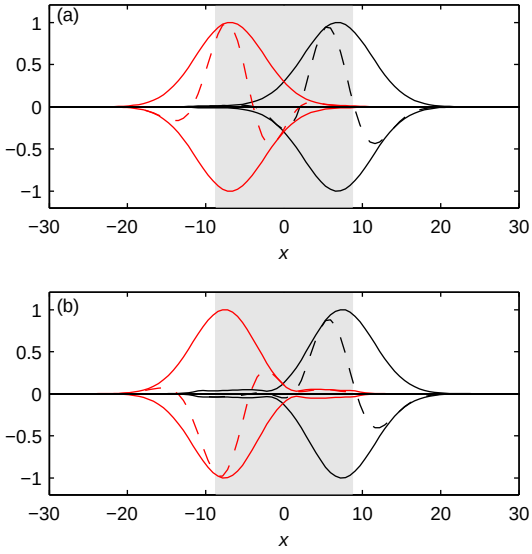

FIGURE 23. The first (a) and second (b) balanced mode. The modes are non-orthogonal and the adjoint balanced modes are shown in red. The absolute value is shown in solid and real part in dashed. The gray area marks the region of instability.

introduced in this section. The projected matrices, denoted by $\hat{P}$ and $\hat{Q}$, have the elements

$$\hat{P}_{i,j} = \langle \psi_i, P\psi_j \rangle \tag{60a}$$

$$\hat{Q}_{i,j} = \langle \phi_i, Q\phi_j \rangle \tag{60b}$$

where ψ_i denotes the adjoint mode associated with ϕ_i. Balancing refers to the fact that if $\hat{P}$ and $\hat{Q}$ are obtained from a projection onto balanced modes, they become diagonal and equal to the Hankel singular values, *i.e.*

$$\hat{P} = \hat{Q} = \Sigma = \mathrm{diag}(\sigma_1, \ldots \sigma_r). \tag{61}$$

The balanced modes are flow structures that are ranked according to their contribution to the input-output behavior. These modes are influenced by the input and, in turn influence the output by the same amount, given by the corresponding Hankel singular values σ_i.

A very attractive feature of balanced truncation is the existence of an *a priori* error bound that is of the same order as the lowest bound achievable for any basis,

$$\sigma_{r+1} < \|G - G_r\|_\infty \leq 2 \sum_{j=r+1}^{n} \sigma_j. \tag{62}$$

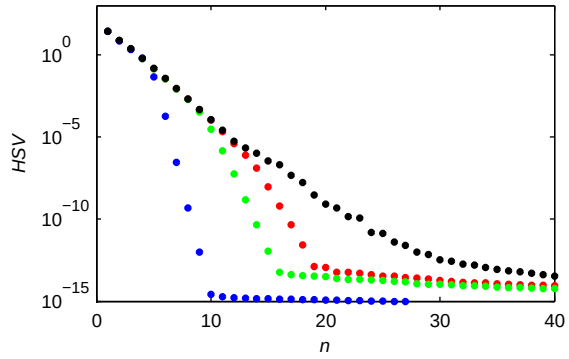

FIGURE 24. Hankel singular values of the approximate balanced truncation are marked with colored symbols and the exact balanced truncation with black symbols. The number of singular values that are correctly captured increases with the number of snapshots (red: 1000, green: 500 and blue: 70 snapshots).

In contrast to equation (58) the above error norm is independent of the input and output matrices B and C. The error norm for the balanced truncation model in figure 21 shows a rapid decay. In figure 22 we notice that the performance of balanced reduced-order models (red lines) $|G_r(i\omega)|$ is very good, and only two balanced modes are required to capture the peak response of the full system.

In summary, we would like to recall that each of the three sets of basis vectors (global modes, POD modes, balanced modes) span different subspaces of the state space and are therefore suitable for different applications. The spatial support is shown in figure 19 for the first 20 modes of each of the three sets. The balanced modes (right plot), by construction, cover the region between the input and the output with very few modes and are thus the appropriate set of functions to accurately capture the input-output behavior of our linear system.

4.4. *The snapshot method*

To compute the POD modes or balanced modes we must first solve Lyapunov equations. This becomes prohibitively expensive as n exceeds approximately 10^5 which usually is the case when discretizing the Navier–stokes equations in two or three dimensions. Recently, numerous iterative methods to solve these equations have appeared (Antoulas 2005; Antoulas *et al.* 2001).

A different approach to approximate the Gramians without solving the Lyapunov equations — the so-called snapshot-based balanced truncation — has recently been introduced (Willcox & Peraire 2002; Rowley 2005). It is based on the snapshot technique first introduced by Sirovich (1987) for computing

POD modes. We will demonstrate the method for one input and one output, see Rowley (2005) for additional details.

We begin with collecting r snapshots $q(t_j)$ at discrete times $t_1, \ldots, t_r$, of the response of the system (24) to an impulse $\delta(t)$. These snapshot are gathered as columns in a $n \times r$ matrix X, *i.e.*

$$X = [e^{At_1}B, e^{At_2}B, \ldots, e^{At_r}B]\sqrt{\Delta_r}, \tag{63}$$

where Δ_r stands for the quadrature coefficients of the time integral in equation (47). Instead of solving the Lyapunov equation (45), we can approximate its solution, *i.e.* the controllability Gramian P as

$$P \approx XX^H M. \tag{64}$$

If we observe that $e^{A^+t}C^+$ is the impulse response of the adjoint state-space equation (25), we can construct an approximation of the observability Gramian Q

$$Q \approx YY^H M \tag{65}$$

by collecting a sequence of snapshots of the adjoint impulse response in the $n \times r$ matrix

$$Y = [e^{A^+t_1}C^+, e^{A^+t_2}C^+, \ldots, e^{A^+t_r}C^+]\sqrt{\Delta_r}. \tag{66}$$

In the method of snapshots, instead of solving the large $n \times n$ eigenvalue problem (59) one can form the singular value decomposition of the $r \times r$ matrix,

$$Y^H MX = U\Sigma V^H. \tag{67}$$

The approximate Hankel singular values (HSV) are given in the diagonal matrix Σ. The normalized balanced modes and the associated adjoint balanced modes are recovered from

$$T = XV\Sigma^{-1/2}, \qquad S = YU\Sigma^{-1/2}. \tag{68}$$

Usually the number of snapshots r is significantly smaller than the number of states n, which makes this method computationally tractable for systems of very large dimensions.

Figure 24 shows the HSVs for the exact balanced truncation (solving two Lyapunov equations) and the approximate HSVs (using the snapshot method). For improved results more snapshots may be taken during periods of large transient energy growth and fewer snapshots as the energy decreases. Snapshot-based balanced truncation has been applied to channel flow (Ilak & Rowley 2008) and to the flow around a pitching airfoil (Ahuja *et al.* 2007).

5. Control

The natural extension to the investigations of the previous sections — the response behavior of a linear system to initial conditions and external excitations — is concerned with attempts to manipulate the inherent dynamics of a system or to control it. A substantial body of literature on flow control has accumulated over the past decade, with topics ranging from laminar flow

control (Joslin 1998) to control of turbulence (Moin & Bewley 1994), from opposition control (Choi *et al.* 1994) to suboptimal (Bewley & Moin 1994) and nonlinear control (Bewley *et al.* 2001; Zuccher & Bottaro 2004; Guégan *et al.* 2006). Reviews on the subject of flow control can be found in Gunzburger (1995); Gal-El-Hak (1996, 2000); Bewley (2001); Kim (2003); Kim & Bewley (2007).

The framework laid out in the following sections falls in the category of *linear feedback control* (Kwakernaak & Sivan 1972; Anderson & Moore 1990; Zhou *et al.* 2002; Skelton *et al.* 1998; Skogestad & Postlethwaite 2005). In particular, our objective is to minimize the perturbation energy resulting from asymptotic or transient instabilities of the uncontrolled system during the transition process in order to suppress or delay turbulence (Joshi *et al.* 1997; Bewley & Liu 1998; Högberg *et al.* 2003*a*). Since the disturbance energy growth is initially a linear process (Schmid & Henningson 2001) it seems prudent to design control schemes for the linearized governing equations. However, linear control has also been applied with considerable success to the full Navier–Stokes equations (Chevalier *et al.* 2007), and attempts have been made to relaminarize a fully developed turbulent flow (Högberg *et al.* 2003*b*).

We will consider two fundamentally different stability scenarios for the evolution of perturbations q governed by the non-parallel Ginzburg-Landau equation: (i) local convective instabilities and (ii) global instabilities. The parameters for the two cases are listed in Table 1.

5.1. *The concept of feedback*

The actuation on the flow can be accomplished by various means, such as, for example, the injection of fluid through blowing/suction holes in the wall. Within the region of validity of our underlying physical model, it is possible to compute a control strategy in advance that will retain the flow in a laminar state. This procedure is referred to as open-loop control. However, under the presence of uncertainty over the exact disturbance environment (or the validity of our physical model), open-loop control will fail. Instead, one can monitor the flow through measurements and adjust the actuation accordingly such that predefined objectives are met. A control setup of this type is known as closed-loop control. It uses feedback to establish a connection between the output from the system (*i.e.* the measurement signal) and the input to the system (*i.e.* the control signal). Under realistic conditions, we are faced with a wide range of unknown variations, such as modeling errors or sensor noise, and a feedback-type control system is required to efficiently compensate for these uncertainties.

The main idea of linear feedback control is shown in figure 1. The entire system is described in state-space form as follows

$$\dot{q} = Aq + B_1 w + B_2 u, \tag{69a}$$

$$z = C_1 q + Du, \tag{69b}$$

$$y = C_2 q + g. \tag{69c}$$

This set of equations is commonly referred to as the *plant*. The first equation (69a) describes the dynamics of our linear system captured in the system matrix A as external forces, modeled by $B_1 w$ and $B_2 u$, are applied. We have decomposed the input into two terms with $B_1 w(t)$ describing the effect of external sources of excitations and $B_2 u(t)$ representing the control input. The variable $z(t)$ given by the second equation (69b) represents the objective function as described below. The third equation (69c) describes a connection between the state q and the measurements y, where the additional term g accounts for noise contaminating the measurements. In general, the objective is to find a control signal $u(t)$ such that the influence of the external disturbances w and g on the output z is minimized. The above set of equations (69) has been discretized using a Hermite collocation method as described in Appendix A.

Our objective is to find a control signal $u(t)$ such that the perturbation energy contained in the state variable $q(t)$ is minimized. Furthermore, the energy input expended by the control must be smaller than the amount of energy gained by it. Thus, in addition to focusing on the perturbation energy we also have to penalize our control effort. This results in a objective (or cost) functional of the form

$$\|z\|_2^2 = \|C_1 q\|_2^2 + \|Du\|_2^2 = \int_0^T q^H \underbrace{C_1^H C_1}_{M} q + u^H \underbrace{D^H D}_{R} u \; dt \tag{70}$$

where M and R are positive semi-definite matrices; we have furthermore assumed that $D^H [C_1 \; D] = [0 \; I]$ in order to get zero cross terms (Zhou *et al.* 2002). It is important to realize that the 2-norm in the above expression is defined both over time and space. Note that if C_1 is chosen as F in equation (19) then the kinetic energy of the disturbance will be minimized. In the above setup we have assumed that the full state q is known, but for realistic flow situations the complete instantaneous velocity field is not available for determining an appropriate feedback. We thus have to *estimate* the full state vector resulting in an approximate state vector $\hat{q}$, reconstructed from the measurements $y(t)$ via an estimation problem. A controller based on an estimated state vector is known as an output feedback controller or a compensator.

5.2. *The LQG framework*

If we assume that the unknown disturbance noise w and the measurement noise g are given by white-noise stochastic processes with zero mean and respective covariances W and G, a compensator can be found that minimizes the cost functional (70). In addition, the closed-loop control is guaranteed to be stable,

if the plant is both observable and controllable. In fact, a sufficient condition for a global minimum value of (70) is that the system is stabilizable and detectable. A system is stabilizable (detectable) if all unstable global modes are controllable (observable).

The control will be optimal in minimizing (70) which stems, in one part, from the optimal filtering of noise that has corrupted our signal (Kalman 1960) and, in another part, from the optimal control when the entire state vector is assumed to be available. These two separate problems — the estimation problem and the full-information problem — can then be combined to construct a compensator. This two-step procedural framework matured in the 1960's into what we now refer to as Linear Quadratic Gaussian (LQG) control (Kwakernaak & Sivan 1972; Anderson & Moore 1990). The assumption that $w(t)$ and $g(t)$ are white-noise stochastic processes may be far from reality in some applications; it is, however, possible to describe a plant with colored-noise input in terms of an augmented system with white-noise input (Lewis & Syrmos 1995).

In applications LQG control is particularly successful when the system operator A (in our case the Ginzburg-Landau equation) accurately describes the modeled physical phenomenon. The remaining uncertainties in the overall model are thus restricted to the inputs represented by stochastic disturbances with known statistical properties. For this reason, the LQG framework is appropriate when we can rely on an accurate plant, while a precise knowledge of external disturbances and the degree of noise contamination of the measurements are not available.

If the external disturbances are stochastic variables, the state will as well be a stochastic process, and the objective function (70) can therefore be written as

$$\|z\|_2^2 = \mathcal{E}\left\{q^H M q + u^H R u\right\}. \tag{71}$$

As alluded to above, we will determine the optimal control $u(t)$ in (69) based on noisy measurements $y(t)$ such that the cost functional (71) is minimized. The first step in constructing such a compensator is to estimate the full state $q(t)$ given only the noisy measurements. After the state has been successfully estimated, we assume, in a second step, that the control $u(t)$ and the estimate of the state $\hat{q}(t)$ satisfy a linear relation involving some yet unknown matrix K, *i.e.*,

$$u(t) = K\hat{q}(t). \tag{72}$$

The goal of this second step is then to find such a matrix K, which is referred to as the control gain.

At the heart of the LQG-framework is the separation principle (Skogestad & Postlethwaite 2005) which states that the controller that minimizes (70) can be computed in two independent steps: (i) we can solve the estimation problem to obtain an approximation $\hat{q}$ of the true state q without any reference to the control problem; (ii) to find the control gain K in (72) we do not need the estimate $\hat{q}$ in (72) but instead can assume the full-information relation $u(t) = Kq(t)$. One of the important consequences of the separation principle

is the fact that the final compensator, using (72) based on the control gain K obtained by considering $q(t)$ (not $\hat{q}$), will always yield a closed-loop system that is stable if and only if each of the two separate problems (estimation and full-information control) are themselves stable (see Zhou *et al.* (2002)). In addition to stability, the closed-loop system will be optimal. To simplify the expressions in the following analysis we assume that the adjoint system is derived using a standard Euclidean inner-product, *i.e.* the dual or the adjoint of the plant (69) is given simply by its complex conjugate transpose.

5.2.1. *The estimation problem*

Under the assumption that the measurements capture a sufficient amount of the system's dynamics (*i.e.* that we have significant observability), it is possible to estimate or observe the state vector by using a Kalman filter (Kalman 1960). In this section we derive the algebraic Riccati equation for estimation and show examples on the Ginzburg-Landau equation. For additional details see *e.g.* Lewis & Syrmos (1995); Anderson & Moore (1990).

We assume zero initial conditions, since we are interested in the controller performance as an average over long time while the system is excited by external perturbations. We further assume white-noise stochastic processes for $w(t)$ and $g(t)$ with zero mean. The estimator then takes on the form

$$\dot{\hat{q}} = A\hat{q} + B_2 u - L(y - \hat{y}), \tag{73a}$$

$$\hat{y} = C_2 \hat{q}. \tag{73b}$$

In the above expression, we compare the measurement y from the state and the measurement $\hat{y}$ from the estimated state and feed back the mismatch in these two quantities using the estimator gain L. To analyze the performance of the estimation problem, it is instructive to derive the dynamics of the estimation error $\tilde{q} = q - \hat{q}$. Combining (69) and (73) we obtain

$$\dot{\tilde{q}} = A\tilde{q} + B_1 w + L(y - \hat{y}). \tag{74}$$

Substituting the explicit dependence of the two measurements on the state q and estimated state $\hat{q}$, respectively, we obtain

$$\dot{\tilde{q}} = (A + LC_2)\tilde{q} + B_1 w + Lg \tag{75}$$

where the estimation error dynamics is governed by the matrix $A_e = A + LC_2$ and is driven by two source terms, namely the external excitation w and the sensor noise g. We aim at finding an estimator gain L such that A_e is asymptotically stable and is not sensitive to the external perturbations $B_1 w + Lg$. Since (69) is driven by noise, the state $q(t)$ and the output $y(t)$ are consequently random processes whose stochastic properties have to be considered in finding the estimator gain L. The error covariance is given as

$$P(t) = \mathcal{E}\{\tilde{q}\tilde{q}^H\} \tag{76}$$

which represents a measure of uncertainty in the estimate. Smaller values of $P(t)$ indicate a better estimate as the estimation error is more tightly distributed about its mean value of zero. If the estimator (75) is stable, the error $\tilde{q}(t)$ will eventually reach a steady-state with a constant mean and covariance. The steady-state covariance can be readily obtained by solving the Lyapunov equation

$$A_e P + P A_e^H + L G L^H + B_1 W B_1^H = 0 \tag{77}$$

where G and W are the covariance matrices of $g(t)$ and $w(t)$, respectively. The optimal estimation feedback gain L is then chosen to both keep (75) stable and to minimize the mean of the steady-state estimation error. We obtain the mean estimation error from the covariance (76) using the expression (39),

$$J = \mathcal{E}\{\tilde{q}\} = \mathrm{trace}(PM), \tag{78}$$

where the mean is chosen as the kinetic energy. This minimization has to be accomplished under the constraint that P satisfies the above Lyapunov equation (77). We add this constraint to the cost functional J via a Lagrange multiplier Λ and obtain the Lagrangian $\mathcal{M}$

$$\begin{aligned}\mathcal{M} &= \mathrm{trace}(PM) + \\ &\quad + \mathrm{trace}[\Lambda(A_e P + P A_e^H + L G L^H + B_1 W B_1^H)].\end{aligned}$$

We thus minimize J subject to the constraint (77) by equivalently finding stationary points of $\mathcal{M}$ without imposed constraints. The necessary conditions for a minimum are given by:

$$\frac{\partial \mathcal{M}}{\partial P} = A_e^H \Lambda + \Lambda^H A_e + M = 0, \tag{79a}$$

$$\frac{\partial \mathcal{M}}{\partial \Lambda} = A_e P + P A_e^H + L G L^H + B_1 W B_1^H = 0, \tag{79b}$$

$$\frac{\partial \mathcal{M}}{\partial L} = 2\Lambda(P C_2^H + L G) = 0. \tag{79c}$$

We can eliminate Λ from equation (79c) to obtain an expression for the estimator gain

$$L = -P C_2^H G^{-1}. \tag{80}$$

Inserting the expression above into the second condition (79b) leads to a quadratic matrix equation for the error covariance P

$$AP + P A^H - P C_2^H G^{-1} C_2 P + B_1 W B_1^H = 0 \tag{81}$$

which is referred to as an algebraic Riccati equation. In Laub (1991); Datta (2003) efficient methods of solving the Riccati equations can be found. We can thus determine the optimal estimation gain L by solving (81) for the error covariance P which, using (104), results in L. No requirements of observability or controllability have to be explicitly imposed on the estimation problem; however, if we place the input describing external disturbances B_1 and the sensor C_2 such that (C_2, A) is observable and (A, B_1) is controllable, then the resulting Riccati equation (81) will have a unique positive definite solution. Moreover, the closed-loop estimator will then be asymptotically stable.

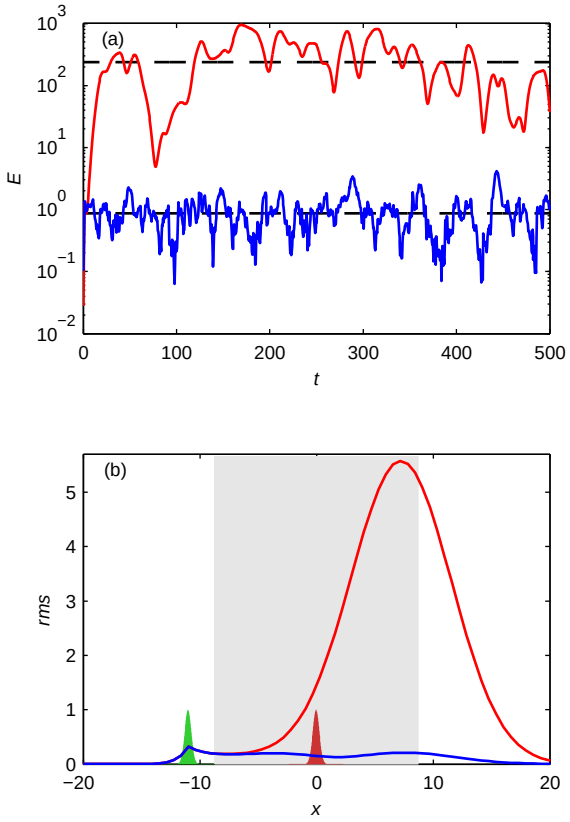

FIGURE 25. (a) The mean of the error covariance trace(PM) (lower dashed line) obtained by solving the Riccati-equation (81) is compared to the estimation error (blue line) obtained by marching the estimator in time (73). Also, the mean value of the state (top dashed line/red line) is shown and found to be nearly three orders of magnitude larger than the estimation error. It is evident that both the state and the estimation error reach a steady state. (b) The rms-value of the error and the state are shown in blue and red lines, respectively. The red and green Gaussian functions represent the location of the input (stochastic disturbances) and the sensor. The error attains its minimum value just downstream of the sensor location and increases upstream as well as downstream of it.

One way to investigate the performance of the estimator, is to compare the energy of the true flow state with the energy of the estimation error. In figure (25a) the temporal evolution of the state energy (red line) and of the estimation error (blue line) are shown. The energy of the estimation error is

nearly three orders of magnitude smaller than the energy of the true state. In the same figure, the mean energy of the estimation error — obtained by solving the Riccati-equation (81) — and the mean energy of the state — obtained by solving the Lyapunov equation (45) — are plotted with dashed lines. We observe that the solutions of the Riccati equation and the Lyapunov equation provide the mean energy in which, respectively, the estimation error and state energy fluctuate about. In figure (25b), the corresponding rms of the error $\tilde{q}_{rms}$ together with the rms of state q_{rms} are shown.

5.2.2. *Full-information control*

The second step in the design of an LQG-compensator involves the solution of an optimal control state-feedback problem. We show in this section that the optimal solution is, again provided by the solution of a Riccati equation. The reader is directed to Anderson & Moore (1990); Lewis & Syrmos (1995) for more detailed derivations.

We seek a control $u(t)$ as a linear function of the flow state $q(t)$ that minimizes the deterministic cost functional

$$J = \frac{1}{2}\int_0^T q^H M q + u^H R u \; dt, \qquad M, R > 0, \tag{82}$$

while satisfying the initial value problem

$$\dot{q} = Aq + B_2 u, \qquad q(t=0) = q_0. \tag{83}$$

We perform the steps analogous to the estimation problem by first defining an augmented Lagrangian $\mathcal{N}$ of the form (Lewis & Syrmos 1995)

$$\mathcal{N} = \frac{1}{2}\int_0^T (q^H M q + u^H R u) + \lambda^T(-\dot{q} + Aq + B_2 u)\; dt \tag{84}$$

where λ is again a Lagrange multiplier which enforces the initial value problem (97). The necessary conditions for a minimum of $\mathcal{N}$ result in the following set of equations

$$\frac{\partial \mathcal{N}}{\partial \lambda} = -\dot{q} + Aq + B_2 u = 0, \tag{85a}$$

$$\frac{\partial \mathcal{N}}{\partial q} = \dot{\lambda} + Mq + A^H \lambda = 0, \tag{85b}$$

$$\frac{\partial \mathcal{N}}{\partial u} = Ru + B_2^H \lambda = 0. \tag{85c}$$

We proceed by assuming a linear relation between the state $q(t)$ and the Lagrange multiplier $\lambda(t)$

$$\lambda(t) = X(t) q(t), \tag{86}$$

where $X(t)$ is self-adjoint and positive semidefinite. Using this linear relation and the optimality condition (85c) yields the following feedback law:

$$u(t) = \underbrace{-R^{-1} B_2^H X(t)}_{K(t)} q(t). \tag{87}$$

To find $X(t)$ we differentiate (86) and use the state equation (85a) to obtain

$$-\dot{\lambda} = \dot{X}q + X(Aq - B_2^H R^{-1} B_2 X q). \tag{88}$$

Substituting equation (85b) into this last expression leads to a quadratic matrix equation for $X(t)$ that (assuming controllability of (A, B_2)) asymptotically converges to

$$A^H X + XA - XB_2 R^{-1} B_2^H X + M = 0. \tag{89}$$

As before, we obtain a Riccati equation for the linear mapping X. The solution to this equation provides the optimal steady feedback gain via the relation (98).

Moreover, stabilizability of (A, B_2) and detectability of (A, C_1) imply additional desirable properties: the feedback gain K is guaranteed to stabilize the plant and to yield a global minimum value of (96). We recall that a system is stabilizable (detectable) if all unstable global modes are controllable (observable). In other words, if we place our actuators such that we ensure controllability of the unstable global modes and if we choose M as the kinetic energy weight matrix, then the closed-loop system is guaranteed to be stable. In the limit as $T \to \infty$ the cost functional is given by (Högberg 2001)

$$J = q_0^H X q_0, \tag{90}$$

and any other stabilizing controller will result in a larger value of this objective functional.

5.2.3. *The LQG-compensator*

Combining the estimator and controller we can now control our plant by solely relying on the measurements $y(t)$. To validate the separation principle, we may write the control (72) in terms of the full state q and the estimation error $\tilde{q}$,

$$u = Kq - K\tilde{q}. \tag{91}$$

We can combine the plant (69) and the equation for the estimation error (75) into the augmented system

$$\begin{pmatrix} \dot{q} \\ \dot{\tilde{q}} \end{pmatrix} = \begin{pmatrix} A + B_2 K & -B_2 K \\ 0 & A + LC_2 \end{pmatrix} \begin{pmatrix} q \\ \tilde{q} \end{pmatrix} + \begin{pmatrix} B_1 & 0 \\ B_1 & L \end{pmatrix} \begin{pmatrix} w \\ g \end{pmatrix}. \tag{92a}$$

Since this augmented system is block-triangular, the eigenvalues of the augmented closed-loop system consist of the union of the eigenvalues of $A_c = A + B_2 K$ and $A_e = A + LC_2$. Thus, if the full-information controller A_c and the estimator A_e are stable, then the closed-loop system, *i.e.*, the compensator,

obtained by combining the plant (69) and estimator (73),

$$\begin{pmatrix}\dot{q}\\ \dot{\hat{q}}\end{pmatrix} = \underbrace{\begin{pmatrix}A & B_2K\\ -LC_2 & A+B_2K+LC_2\end{pmatrix}}_{\mathsf{A}}\begin{pmatrix}q\\ \hat{q}\end{pmatrix} + \underbrace{\begin{pmatrix}B_1 & 0\\ 0 & -L\end{pmatrix}}_{\mathsf{B}}\begin{pmatrix}w\\ g\end{pmatrix} \tag{93a}$$

$$z = \underbrace{(C_1 \;\; DK)}_{\mathsf{C}}\begin{pmatrix}q\\ \hat{q}\end{pmatrix} \tag{93b}$$

is also stable. As the separation principle suggests, the compensator consisting of an optimal estimator and an optimal full-state controller is itself optimal. The closed-loop system, given by equation (93), as two inputs, the external disturbances w and the measurements noise g, and one output, the objective function z. This closed-loop system is treated as a new dynamical system whose properties, such as stability, input-output behavior and performance, have to be investigated. Next, we discuss these issues for the two prototypical flow cases.

5.3. *Control of Subcritical flow*

For a choice of parameters that results in a convectively unstable plant (Table 1), the objective is to apply control schemes that lower transient energy growth or reduce the amplification of external disturbances. We will now construct a LQG-compensator for the Ginzburg-Landau equation to illustrate how a typical convectively unstable flow system may react to control. Similar to the analysis of the uncontrolled system in sections 2 and 3, the response behavior of the closed-loop system — in terms of spatio-temporal evolution of the state, kinetic energy and sensor signal — will be investigated for various inputs, optimal initial disturbance, harmonic forcing and stochastic forcing.

Before control schemes can be designed, one has to decide on the placement of actuators and sensors, the choice of which is reflected in the matrices B_2 and C_2. We assume the spatial distribution of the inputs and the outputs as Gaussian functions of the form given by (108). The width parameter $s = 0.4$ is chosen such that 95% of the spatial extent of the input/output distributions are $\sim 5\%$ of the length of the unstable domain (see figure 31a). In this way, we are restricted — as in any practical implementation of control schemes — to only a limited number of noisy measurements and to actuation in a rather small region of the full domain. An additional simplification is made by considering only one actuator and one sensor.

Identifying regions of the flow where sensing and actuation are favorable to the feedback control of a convectively unstable system is significantly complicated by the convective nature of the flow. Usually one has to use physical intuition and a trial-and-error approach. Transient growth of energy due to the non-normality of A is associated with the local exponential growth of disturbances between branch I and II. As a consequence — and in contrast to the

globally unstable case (see next section), where it suffices to estimate at branch II and control at branch I — the entire unstable domain between branch I and II is of great importance for the flow dynamics.

Appropriate choices for the location of an actuator and a sensor for the subcritical Ginzburg-Landau equation is found to be $x_u = -3$ and $x_s = 0$, respectively. In figure 31a, the actuator and sensor placement are shown that result in an acceptable closed-loop performance.

5.3.1. *Stochastic disturbance*

Consider a system driven by white noise $B_1 w(t)$ just upstream of branch I. From the noisy measurements $y(t) = C_2 q(t) + g$ between branch I and II an estimated state is obtained. Based on this estimate, the control signal $B_2 u(t)$ is applied upstream to the sensor. The placement of the excitation, sensor and actuator is shown in figure 31a.

The covariance of the external and measurement noise should be chosen to match as closely as possible the uncertainties that are expected for the chosen design configuration, but it is difficult to make more specific statements. It has however been found (Hœpffner *et al.* 2005; Chevalier *et al.* 2006; Hœpffner & Brandt 2008) that the performance of the estimator can be improved dramatically if the covariances are chosen to reflect physically relevant flow structures rather than generic probability distributions. For our problem, the sensor noise g is chosen to have a variance of $G = 0.1$ which is 10% of the variance of a random input with $W = 1$.

Since (69) is driven by white noise $w(t)$, the state $q(t)$ is consequently a random process and is defined by its stochastic properties, *e.g.* its covariance $P = \mathcal{E}\{qq^H\}$. As we have shown in section 3.2, these properties are linked to the statistical characteristics of the forcing via a Lyapunov equation (45).

In figure 31a the rms-values (40) of the state without control (red) and with control (black) are shown. The rms-value of the uncontrolled state grows exponentially as it enters the unstable domain at branch I; this growth prevails until branch II. The rms of the controlled state, however, grows only slightly in the unstable region and is considerably lower than the rms-value of the uncontrolled state at branch II.

In figures 31b and c the performance of the compensator is shown more explicitly in form of a temporal simulation of the closed-loop system (93) in time. The control is only engaged for $t \in [250, 750]$. Without control the stochastic disturbances grow exponentially as they enter the unstable region at $x = -8.2$ and decay as they exit the region at $x = 8.2$. When the control is activated the perturbation energy is reduced from $E \approx 10^3$ to $E \approx 1$. When the control is disengaged, the disturbances immediately start to grow again. During and after the time when the control is applied the perturbation energy reaches a steady-state at a level that can be determined from the covariance of the state according to $E = \mathrm{trace}(PM)$, (equation (39)). Dashed lines in figure 31c indicate these levels.

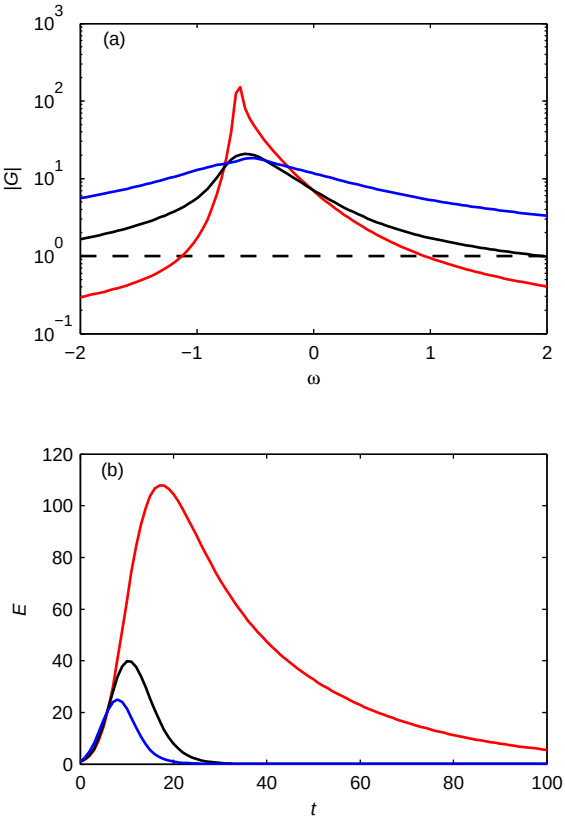

FIGURE 26. (a) Comparison of the frequency response of the open-loop (red), LQG-controlled (black) and $\mathcal{H}_\infty$-controlled (blue) Ginzburg-Landau equation. For the open-loop, the ∞-norm corresponding to the peak value of the response is 151, whereas the 2-norm corresponding the to integral of the response is 20.5. The $\mathcal{H}_\infty$ controller minimizes the peak value to 18.4 and reduces the 2-norm to 8.7. The LQG/$\mathcal{H}_2$ controller, on the other hand, minimizes the 2-norm to 6.1 and reduces the peak value to 20.8. (b) The energy evolution of an optimal disturbance is shown for the convectively unstable Ginzburg-Landau equation (red line) and the closed-loop system computed with LQG/$\mathcal{H}_2$ (black) and $\mathcal{H}_\infty$ (blue).

5.3.2. *Harmonic and optimal disturbance*

The aim of feedback control for subcritical flows is to design closed-loop systems with small transfer function norms compared to the stable open-loop system. Maximum transient energy growth of a perturbation and the norm of the system

transfer function G are linked for highly non-normal systems (see section 3.1 for details). To show this link, we will pose the LQG problem as a control problem in the frequency domain with the objective to minimize the 2-norm of the closed-loop transfer function.

The relation between the input and output signals, that is, between disturbance and measurement noise and the objective function, $(w \to z, g \to z)$, of the closed-loop system (93) (displayed schematically in figure 1) can be described by the transfer function,

$$G_c(s) = \mathsf{C}(sI - \mathsf{A})^{-1}\mathsf{B} \qquad s \in \mathbb{C}. \tag{94}$$

The relation between the objective function (70) in the time-domain and in the frequency domain can easily be found from Parseval's identity,

$$\int_{-\infty}^{\infty} z^2 \; dt = \frac{1}{2\pi} \int_{-\infty}^{\infty} \mathrm{trace}|G_c(i\omega)|_2^2 d\omega = \|G_c(i\omega)\|_2^2 \tag{95}$$

with $|G_c|_2^2 = G_c^H G_c$. We have thus defined the 2-norm of the transfer function $G_c(s)$ as the integral over the 2-norm of the amplitude of the transfer function along the imaginary axis. The $\mathcal{H}_2$ problem is then to minimize (95). The symbol $\mathcal{H}_2$ stands for the "Hardy space" (Zhou *et al.* 2002) which contains the set of stable transfer functions with bounded 2-norms.

In figure 26a the frequency response $(w \to z, g \to z)$ of the open-loop system is shown (red line) for the subcritical Ginzburg-Landau equation; we observe a 2-norm of 20.5. The corresponding LQG/$\mathcal{H}_2$ closed-loop transfer function (94) is displayed (black line) in figure 26, where the 2-norm is now minimized to a value of $\|G_c\|_2 = 6.1$. In figure 26b the optimal energy growth (section 2.3) of the uncontrolled and controlled system are compared. The maximum transient energy growth (peak value) is reduced by an order of magnitude.

5.4. *Control of supercritical flow*

For a globally unstable flow (parameters given in Table 1), *i.e.*, an unstable plant (69), the influence of uncertainties ($w(t)$ and $g(t)$) on the system dynamics is rather small compared to the asymptotic behavior of the most unstable global mode. This mode will grow exponentially as soon as any disturbance (assuming it is not orthogonal to the unstable mode) enters the unstable region. For this reason disturbance modeling may not play a decisive role for globally unstable flows, in contrast to convectively unstable flows.

The goal of any control effort is to stabilize an otherwise unstable system; this task is particularly straightforward using LQG-based feedback control, since the closed-loop system (93) is guaranteed to be stable as long as the actuator and the sensor are placed such that the system is both stabilizable and detectable.

In other words, the performance of a controller to a globally unstable Ginzburg-Landau equation can only be successful if all unstable global modes

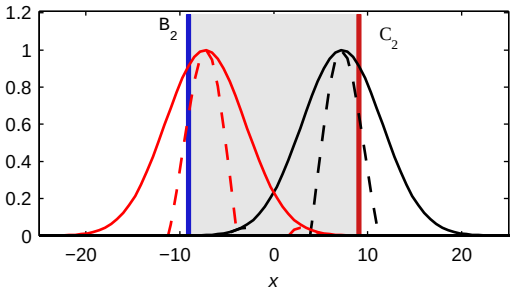

FIGURE 27. Actuator and sensor placement for the supercritical Ginzburg-Landau equation which yields a stabilizable and detectable system. The spatial support of the actuator (blue bar), sensor (red bar), the unstable domain (gray region) as well as the unstable global mode (black lines) together with its corresponding adjoint mode (red lines) are shown.

are controllable and observable. It was concluded in section 4.1 that a global mode is controllable (observable) if the overlap of the actuator (sensor) and the adjoint mode (global modes) is nonzero. In figure 27, a configuration for the actuator and sensor is shown that yields a plant which is both stabilizable and detectable.

For this set-up a LQG compensator (93) is constructed by solving the Riccati equations (99) and (81). The perturbation energy, the impulse response and the spectrum of the uncontrolled plant (69) and controlled closed-loop system (93) are shown in figures 28 and 29. We observe that the closed-loop system has all eigenvalues in the stable half-plane yielding an asymptotically stable flow.

For a point-wise spatial distribution of actuators $\delta(x - x_u)$ it has been shown in Lauga & Bewley (2003) that the Ginzburg-Landau equation gradually loses stabilizability as the parameter μ_0 is increased. This loss is due to the increasing number of unstable global modes which are located further downstream. Controllability of the unstable global modes is gradually diminished as the support of the actuator and the support of the corresponding unstable adjoint global modes (57c) move apart until controllability is entirely lost. At this point no compensator will be able to stabilize the system using one pointwise actuator.

5.5. *The $\mathcal{H}_\infty$ framework — robust control*

In the previous sections we have tacitly assumed that the system matrices A, B and C are known exactly. In reality, however, this is not the case, since modeling errors (for example, a small mismatch in the Reynolds number between the model and the actual flow) are always present. The presence of these errors raises the important issue of robustness of a specific control design.

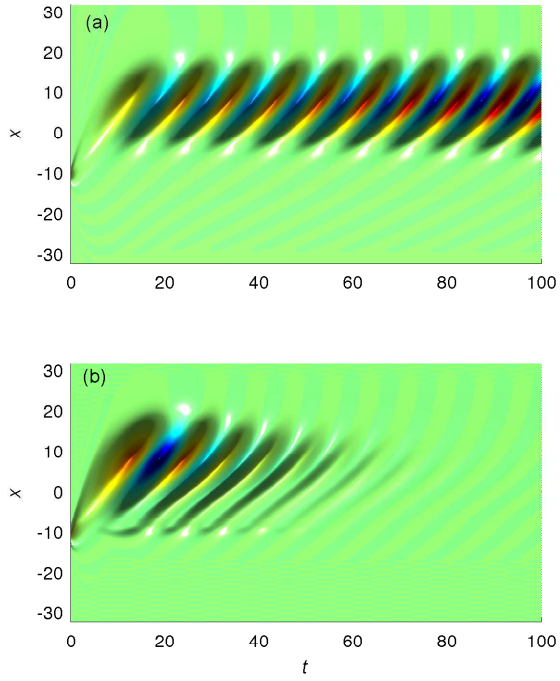

FIGURE 28. The spatio-temporal response to an impulse in time induced at $x = -10$ for the uncontrolled system (a) and LQG-controlled system (c).

Concentrating for simplicity on the dynamic model error, let us consider a model system given by A. The real flow, on the other hand, shall be subject to a small deviation from this model and is described by the dynamic matrix $A + \epsilon\Delta$ with Δ as a unit-norm uncertainty matrix and with ϵ parameterizing the magnitude of the uncertainty. For a given value of ϵ, the controller designed for A has the "robust stability" property if the closed-loop system is stable for all unit-norm uncertainty matrices Δ and, similarly, has the "robust performance" property if the performance of the closed-loop system is satisfactory for all possible unit-norm uncertainty matrices Δ. If information about the specific form of the uncertainties is available, one can restrict the structure of the uncertainty matrix Δ to reflect this information and thus reduce the "uncertainty set". In a similar fashion, the magnitude ϵ of the uncertainty may be estimated or bounded.

Unfortunately, the LQG/$\mathcal{H}_2$-control design does not account explicitly for uncertainties in the system matrices, which is needed to guarantee robust performance or even robust stability. For a given controller, the smallest value of ϵ such that the closed-loop system is unstable is referred to as the *stability margin*. It is known (Doyle Aug 1978) that there are no guaranteed stability

margins for LQG/$\mathcal{H}_2$-controllers. However, this does not necessarily mean that the $\mathcal{H}_2$-controller will be unstable for very small values of ϵ; instead, it merely means that the search for robustness is not accounted for.

To incorporate the presence of uncertainties into the control design framework one can adjust the actuation penalty and sensor noise which, in turn, directly affects the strength of the controller and may help push the control design toward robustness. This approach has led to the development of control optimization based on the $\mathcal{H}_\infty$-norm. Instead of minimizing the energy of the transfer function (*i.e.*, the integral of the frequency response over all frequencies), it concentrates instead on reducing the peak value of the frequency response. These are two very different objectives: for instance, a strong peak in the frequency response localized about one single frequency may not contribute significantly to the energy (integral) of the response. This new $\mathcal{H}_\infty$-objective plays a pivotal role in the search for robustness since closed-loop instabilities can be quantified by the relation between the magnitude of the dynamic uncertainty and the maximum frequency response (Zhou *et al.* 2002).

The steps to compute $\mathcal{H}_\infty$-controllers closely follow the ones for LQG/$\mathcal{H}_2$-design except that a new term is added to the objective functional that will represent the worst possible external forcing. The subsequent optimization scheme will search for a controller that achieves the best performance for the worst perturbation (Bewley & Liu 1998; Bewley 2001). Mathematically, this is equivalent to searching for a saddle point of this new objective functional rather than a minimum. The augmented objective functional reads

$$J = \int_0^T q^H M q + u^H R u - \gamma^2 w^H W w \; dt. \tag{96}$$

In this expression w represents both external disturbances and measurement noise. We then wish to find the control u which minimizes the control objective (70) in the presence of a disturbance w that maximally disrupts this objective. A new free parameter γ appears that plays the role of ϵ in parameterizing the magnitude of the worst perturbation.

To simplify the following derivation we assume for now that $W = 1$ and $R = 1$. Similar to the LQG-design in 5.2.3, we can also specify the control objective in the frequency domain instead of the time domain (96). In this case we simply aim at restricting the maximum values of the closed-loop transfer function as given by (see *e.g.* Green & Limebeer (1995)),

$$\|G_c(i\omega)\|_\infty \leq \frac{\|z\|_2}{\|w\|_2} \leq \gamma. \tag{97}$$

The above transfer function norm was defined in (36).

The $\mathcal{H}_\infty$-problem consists of finding a control signal $u(t)$ that minimizes both the perturbation energy and control effort while *maximizing* the effects of the external disturbances w. As the parameter γ approaches infinity the objective functional (and the optimal control) reduces to the one of the LQG-problem. In this review we will merely present the solution of the $\mathcal{H}_\infty$-problem

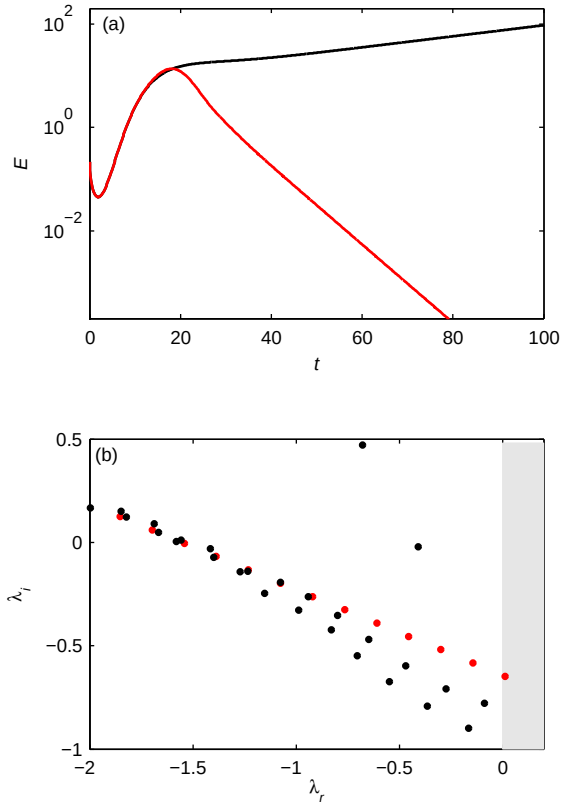

FIGURE 29. Top figure: The perturbation energy of an initial condition which illustrates the asymptotic growth and decay of the global mode of the controlled and uncontrolled systems. Bottom figure: The spectrum of the uncontrolled (red) and LQG-controlled (black) Ginzburg-Landau equation. The exponential growth of the wavepacket in figure 28a is due to one unstable global mode of the open-loop shown by the red circle in the unstable half-plane (gray region). The LQG-based closed-loop is stable with no unstable eigenvalues.

and show how it relates to the LQG-solution. For a more detailed derivation of this link see Zhou *et al.* (2002) or Green & Limebeer (1995).

The solution of the above $\mathcal{H}_\infty$-problem is, similar to the LQG-problem, obtained by solving two Riccati equations which stem from two separate problems: the estimation and the full-information control problem. The full-information control problem leads to the Riccati equation of the form

$$A^H X + XA - X(-\gamma^{-2} B_1 B_1^H + B_2 B_2^H)X + M = 0 \tag{98}$$

with the control given by

$$u = \underbrace{-B_2^H X}_{K} q. \tag{99}$$

Furthermore, one finds that the worst-case disturbance w is given by

$$w_{worst} = \gamma^{-2} B_1^H X q. \tag{100}$$

The Riccati equation (98), whose solution yields the control feedback gain for $\mathcal{H}_\infty$, is modified such that it takes into account the worst-case disturbance acting on the system. We notice that the term $-\gamma^{-2} B_1 B_1^H$ is absent in the Riccati equation (99) of the LQG-problem. Rather, by modeling and incorporating the structure of the disturbances B_1 when computing the feedback gain K, the components of the state that are expected to be most influenced by external disturbances are forced by the largest feedback, $K\hat{q}$. We would like to point out that the parameter γ is supplied by the user and that the resulting control (99) is only suboptimal rather than optimal. For large values of γ, the full-information solution of the associated LQG-problem and the optimal control signal are recovered.

The estimated state is also computed in the presence of worst-case disturbances $\hat{w}_{worst} = \gamma^{-2} B_1^H X \hat{q}$ and is therefore the result of the following estimation problem

$$\dot{\hat{q}} = A\hat{q} + B_1 \hat{w}_{worst} + B_2 u - L(y - \hat{y}), \tag{101a}$$

$$\hat{y} = C_2 \hat{q}. \tag{101b}$$

Similar to the LQG-estimation problem, the difference between the true measurement y and the estimated measurement $\hat{y}$ is fed back using the estimator gain L. There is, however, no longer any assumption on the disturbances w and g. Instead the additional term $B_1 \hat{w}_{worst}$ provides the estimator with information on the worst-case disturbance. The estimation gain in equation (101) is given by $L = -ZYC_2^H$, where Y is the solution of the following Riccati equation (for a derivation of this result see, *e.g.* Zhou *et al.* (2002))

$$AY + YA^H - Y(-\gamma^{-2} C_1^H C_1 + C_2^H G^{-1} C_2) Y + B_1 B_1^H = 0, \tag{102}$$

and Z is a constant matrix given by

$$Z = (I - \gamma^{-2} YX)^{-1}. \tag{103}$$

Equation (102) can now be compared to the Riccati equation (81) for the LQG-problem. The additional term $-\gamma^{-2} C_1^H C_1$ is present in the above equation which reflects the fact that the computation of the estimation gain L depends on the weights in the cost functional. The components of the estimated state that most contribute to the objective functional are forced stronger by the feedback $L(y - \hat{y})$. In addition we notice that the estimation gain L depends via equation (103) on the solution of the full-state Riccati solution X.

By combining the estimator (101) and the plant (69) it is straightforward to formulate the $\mathcal{H}_\infty$-compensator as a closed-loop system. Even though the required calculations (the solution of two Riccati equations) are reminiscent

of the LQG-approach, in the $\mathcal{H}_\infty$ case we face additional restrictions for the stability of the closed-loop system and a more demanding computational effort for finding an optimal controller.

First, stabilizability and detectability is no longer a sufficient condition to guarantee the stability of the closed-loop system. For the $\mathcal{H}_\infty$-problem to be solvable, the spectral radius ρ of XY has to be smaller than γ^2 (Doyle *et al.* Aug 1989).

Secondly, the solution presented above is merely suboptimal; finding an optimal robust controller involves an iterative process that terminates when a lower bound γ_0 of γ is found which still satisfies $\rho(XY) < \gamma^2$. This optimal γ_0 can typically be found with fewer than 20 iterations using the bisection algorithm.

We use the Ginzburg-Landau equation to exemplify the techniques introduced above. For a more detailed investigation we refer to Lauga & Bewley (2004). In figure 26a the frequency response (*i.e.*, the mapping $w, g \rightarrow z$) of the open-loop system is shown with a red line for the subcritical Ginzburg-Landau equation, displaying a ∞-norm of 151. The corresponding $\mathcal{H}_\infty$ closed-loop design is shown with a blue line where the ∞-norm is now reduced to $\|G_c\|_\infty = 18.4$. Comparing the frequency responses of the controlled systems based on the $\mathcal{H}_2$ and $\mathcal{H}_\infty$, we can confirm that in the former case the 2-norm $\|G_c\|_2$ is minimized while in the latter case $\|G_c\|_\infty$ is minimized. Consequently, the most amplified frequencies are more damped in the $\mathcal{H}_\infty$-case at the expense of the higher frequencies which are amplified compared to the uncontrolled case. The $\mathcal{H}_2$ controller, on the other hand, shows a smaller reduction of the most unstable open-loop frequencies (*i.e.* the peak value in the frequency response). This is not surprising, since the $\mathcal{H}_2$-controller minimizes the energy — the integral of the transfer function along the imaginary axis — whereas the $\mathcal{H}_\infty$-controller minimizes the peak value of the transfer function on the imaginary axis.

The optimal energy growth (see equation (21)) in figure 26b demonstrates that the maximum energy growth is smaller for the $\mathcal{H}_\infty$-design which suggests that reducing the most amplified frequencies, rather than all the frequencies, is a more efficient strategy for damping maximum energy growth. However, to achieve its goal the $\mathcal{H}_\infty$-controller expends more control energy than the corresponding $\mathcal{H}_2$-controller (Lauga & Bewley 2004).

Using the Ginzburg-Landau equation for a set of parameters that yields a globally unstable flow Lauga & Bewley (2004) compared the $\mathcal{H}_\infty$-controller to the $\mathcal{H}_2$-controller for a range of control penalties and various levels of measurement noise. They found that the $\mathcal{H}_\infty$ control design always uses more control energy (for the same control penalty) than the corresponding $\mathcal{H}_2$ control design. A robust controller uses this additional control energy to ensure that the constraint on the maximum value of the transfer function norm $\|G_c\|_\infty$ is satisfied.

5.6. *Reduced-order controllers*

The process of systematic control design as presented above involves the solution of two Riccati equations. The cost of computing a Riccati solution is of order n^3 where n is the number of components in the discretized state vector. Whereas for the Ginzburg-Landau equation n is still sufficiently low to allow a direct solution of the Riccati equations, for the Navier–Stokes equations the number of state vector components is rather large. The cost of a direct Riccati solution is prohibitively expensive when $n > 10^5$ which is easily reached for two- and three-dimensional flow configurations. As discussed in section 4, this high cost can be avoided by developing a reduced-order model which preserves the essential flow dynamics.

Similar to solving a Lyapunov equation, there exist "matrix-free" methods to solve a Riccati equation. One common approach that significantly reduces the cost of directly solving the Riccati equation — if the number of inputs and outputs is much smaller than the number of states — is known as the Chandrasekhar method (Kailath 1973). In this method the Riccati solution is expressed as the solution to a coupled system of ordinary differential equations which needs to be integrated in time (see Hœpffner *et al.* (2005) for an application).

Even if we manage to obtain the feedback gains from the full system, however, there still remains the issue that the controller is of very high order, which requires a rather fast feedback-system running next to the experiment.

We will return to the issue of model reduction (see section 4) based on the projection of the original high-dimensional system onto a smaller system using a given basis. One of the main advantages of this approach is that the error in the reduced-order model can be quantified in terms of transfer functions as shown in equation (54) and (58).

Once a reduced-order model is devised (using the techniques in section 4) whose transfer function is a sufficiently good approximation of the open-loop transfer function, we can design an $\mathcal{H}_2$- or an $\mathcal{H}_\infty$-controller for this reduced model. This results in a reduced-order controller which, coupled to the full-order open-loop system, will result in the following augmented system

$$\begin{pmatrix} \dot{q} \\ \dot{\hat{q}} \end{pmatrix} = \begin{pmatrix} A & B_2\hat{K} \\ -L\hat{C} & \hat{A} + \hat{B}_2\hat{K} + \hat{L}\hat{C} \end{pmatrix} \begin{pmatrix} q \\ \hat{q} \end{pmatrix} + \begin{pmatrix} B_1 & 0 \\ 0 & -\hat{L} \end{pmatrix} \begin{pmatrix} w \\ g \end{pmatrix}. \tag{104}$$

The expression of the reduced-order controller is equivalent to the full-order given by equation (93), except that the quantities marked with $\hat{}$ are of order $r \ll n$. Note that the feedback gain K and estimation gain L have the dimension of the reduced model resulting in a fast online controller.

We can now compare the frequency response of the reduced-order models with and without control. The frequency response of the full model without control was shown by the dashed blue lines in figures 22. The frequency response of reduced-order models using global modes (green), proper orthogonal

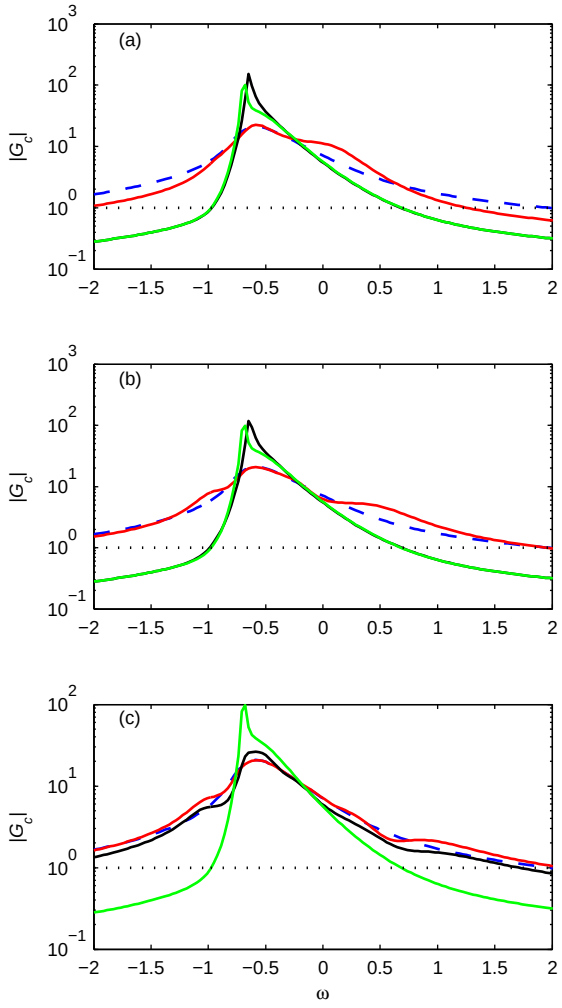

FIGURE 30. The frequency response of the closed feedback-loop based on a LQG-compensator. Blue dashed lines represent the full model of order $n = 220$. The performance of reduced-order models based on $r = 2, 4$ and 6 modes are shown in the (a), (b) and (c), respectively. Red lines represent balanced modes, black lines POD modes and green lines global eigenmodes. We observe that reduced order controller based on balanced modes outperforms the other two models. The poor performance of the reduced-order based on POD and global modes, is directly associated with the unsatisfactory approximation of the open-loop case in figure 22.

decomposition (POD) modes (black) and balanced modes (red) were also shown in the figures.

In figures 30a,b,c we display with dashed blue lines the frequency response $G_c(i\omega)$ of the LQG closed-loop system when solving the full-order ($n = 220$) Riccati equations. Comparing the dashed blue lines in figure 22, where the frequency response of the reduced-model of the open-loop is shown, with the ones of the closed loop in figure 30, we see that the most unstable frequencies are reduced by an order of magnitude. Solving the Riccati equations for the reduced models of order $r = 2, 4$ and 6 for the three sets of modes (global, POD, balanced modes) we observe the same trend for the closed-loop system as we saw for the open-loop system: the reduced-order model based on two balanced modes (red line in figure 30b) is able to obtain a closed-loop performance very similar to the full model, whereas POD modes require a substantially larger basis and global modes fail entirely.

It should be mentioned that model reduction for unstable systems is also possible using global modes (Åkervik *et al.* 2007), POD modes (Gillies 1998) and, more recently, balanced modes (Ahuja & Rowley 2008).

6. Conclusion

A unifying framework for linear fluid dynamical systems has been presented and reviewed that allows the analysis of stability and response characteristics as well as the design of optimal and robust control schemes. An input-output formulation of the governing equations yields a flexible formulation for treating stability problems and for developing control strategies that optimize given objectives while still satisfying prescribed constraints.

The linear Ginzburg-Landau equation on the infinite domain has been used as a model equation to demonstrate the various concepts and tools. It has been modified to capture both subcritical and supercritical disturbance dynamics and thus span the range of fluid behavior observed in various generic shear flow configurations. With a small modification, the equation can also be used to mimic instabilities in other spatially developing flows, for instance flows on semi-infinite domains such as inhomogeneous jets and wakes. We should however keep in mind that Ginzburg-Landau is a great simplification of the dynamics described by linearized Navier–Stokes equations, modelling merely the fundamental behavior of different types of local and global instabilities and the transition between them.

Input-output-based analysis tools, such as the impulse response or the frequency response, have been applied to the model equation. This type of analysis lays the foundation for a thorough understanding of the disturbance behavior and the design of effective control strategies. Concepts such as controllability and observability play an important role for both the input-output behavior and the control design.

The design of effective and efficient control strategies is a challenging task, starting with the placement of actuators and sensors and ending with the judicious choice of a model reduction basis in order to numerically solve the compensator problem. Along the way, compromises between optimality ($\mathcal{H}_2$-control) and robustness ($\mathcal{H}_\infty$-control) have to be made that influence the overall performance of the feedback system.

It is hoped that this review has given a comprehensive and modern introduction to the fields of stability and control theory and has shown the close link between them. It is further hoped that it will spark interest in the fluid dynamics community to continue the exploration of these two exciting disciplines.

The Matlab files to reproduce the results and figures of this review article are available from the FTP server *ftp://ftp.mech.kth.se/pub/review.*

Acknowledgements

This work was partially sponsored by the Air Force Office of Scientific Research, under grant/contract number FA8655-07-1-3053 through the EOARD. The first author acknowledges financial support by École Polytechnique and the Swedish research council (VR) for his stay at LadHyX where part of this work was performed.

Appendix A. Discretization

The numerical studies in this review article are based on a pseudospectral discretization of the Ginzburg-Landau operator $\mathcal{A}$ using Hermite functions and the corresponding differentiation matrices provided by Weideman & Reddy (2000). To approximate the derivatives in (1), we expand the solution $q(x,t)$ in n Hermite functions

$$q(x,t) = \sum_{j=1}^{n} \alpha_j(t) \exp(-\frac{1}{2}b^2x^2) H_{j-1}(bx) \tag{105}$$

where $H_j(bx)$ refers to the jth Hermite polynomial. The differentiation process is exact for solutions of the form

$$f(x) = \exp(-\frac{1}{2}b^2x^2)p(bx) \tag{106}$$

where $p(bx)$ is any polynomial of degree $n-1$ or less. The scaling parameter b can be used to optimize the accuracy of the spectral discretization (Tang 1993). A comparison of the above expression with the analytical form of the global Ginzburg-Landau eigenmodes (11b) shows that they are of the same form except for the exponential term $\exp\{(\nu/2\gamma)x\}$ stemming from the convective part of the Ginzburg-Landau equation. This exponential term is responsible for the non-orthogonality of the eigenmodes of $\mathcal{A}$. The Hermite functions are thus the "orthogonal part" of the global modes. By choosing the Hermite function

scaling factor $b = \chi$ we obtain a highly accurate approximation of $\mathcal{A}$, since any solution of the Ginzburg-Landau equation will decay with the same exponential rate as the Hermite functions in the limit as the domain tends to infinity.

The collocation points $x_1, \ldots, x_n$ are given by the roots of $H_n(bx)$. We also notice that the boundary conditions are enforced implicitly and that $-x_1 = x_n = \mathcal{O}(\sqrt{bn})$ in the limit as $n \to \infty$ (Abramowitz & Stegun 1964). The discretization converts the operator $\mathcal{A}$ into a matrix A of size $n \times n$ (with n as the number of collocation points). Throughout this review article we present results for $n = 220$ yielding a computational domain with $x \in [-85, 85]$.

Discretization transforms flow variable $q(x,t)$ into a column vector $\hat{q}(t)$ of dimension n, and the inner product is defined as

$$\begin{aligned} \langle f, g \rangle &= \int_{-\infty}^{\infty} f(x)^* g(x) dx \\ &\approx \sum_{i=1}^{n} \sum_{j=1}^{n} \hat{f}_i^H \hat{g}_j w_{i,j} = \hat{f}^H M \hat{g} = \langle \hat{f}, \hat{g} \rangle_M, \end{aligned} \tag{107}$$

where $\hat{f} = [\hat{f}_1 \ldots \hat{f}_n]^H$ and $\hat{g} = [\hat{g}_1, \ldots, \hat{g}_n]^H$ are column vectors consisting of, respectively, $f(x)$ and $g(x)$ evaluated at the collocation points. The symbol ^{H} denotes the Hermitian (complex conjugate transpose) operation. The positive-definite matrix M contains the weights $w_{i,j}$ of the chosen quadrature rule. For instance, applying the trapezoidal rule to the Hermite collocation points results in a diagonal matrix $M = \frac{1}{2}\mathrm{diag}\{\Delta x_1, \Delta x_2 + \Delta x_1, \ldots, \Delta x_{n-1} + \Delta x_{n-2}, \Delta x_{n-1}\}$, with $\Delta x_i = x_{i+1} - x_i$. In this paper, the discrete variables $\hat{f}$ are denoted by f.

The operators B and C, describing the input and output configuration, are represented at their respective collocation points. We assume a spatial distribution of inputs $B = \{B_1, \ldots, B_p\}$ and outputs $C = \{C_1 \ \ldots \ C_r\}^T$ in the form of Gaussian functions

$$B_i u(t) = \exp\left[-\left(\frac{x - x_{w,i}}{s}\right)^2\right] u(t), \tag{108a}$$

$$C_i q(t) = \exp\left[-\left(\frac{x - x_{s,i}}{s}\right)^2\right]^H M q(t). \tag{108b}$$

where x represents the Hermite collocation points.

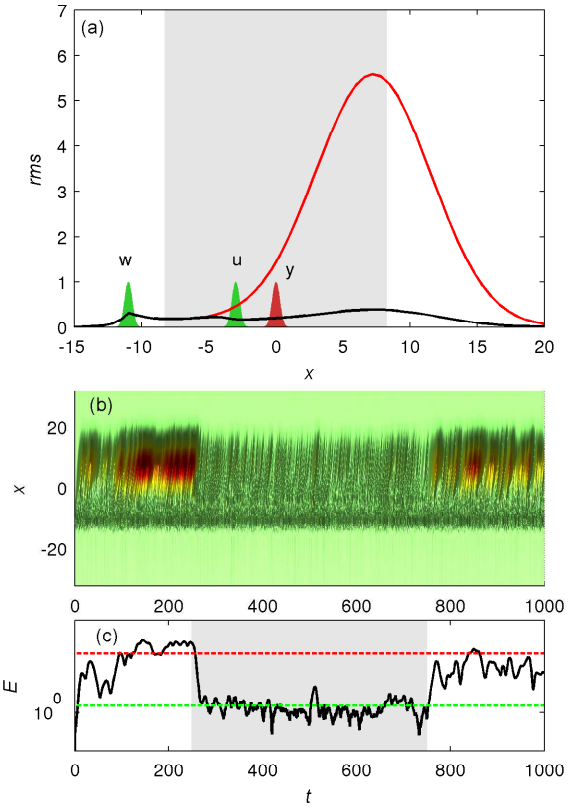

FIGURE 31. The controlled Ginzburg-Landau equation with stochastic excitation: (a) white noise w with zero mean and unit variance $W = 1$ forces the system at $x = -11$, just upstream of unstable region with input B_1 as a Gaussian function (green). Measurements $y(t)$ of the state (red Gaussian) contaminated by white noise with zero mean and variance $G = 0.1$ are taken at $x_s = 0$. The actuator u with control penalty $R = 1$ is placed upstream of the sensor at $x_u = -3$. The rms-values of the uncontrolled and LQG-controlled state are given by the solid red and black lines, respectively. The absolute value of the state $|q|$ is shown in an x-t-plane in (b), while the lower plot (c) displays the kinetic energy $E = \|q\|_M$ as a function of time. The control is only engaged for $t \in [250, 750]$. Dashed lines in (c) indicate the mean value computed from Lyapunov equation.

References

Abramowitz, M. & Stegun, I. E. 1964 *Handbook of mathematical functions : With formulas, graphs, and mathematical tables*. Washington, DC: National Bureau of Standards.

Ahuja, S. & Rowley, C. W. 2008 Low-dimensional models for feedback stabilization of unstable steady states. *AIAA Paper 2008-553, 46th AIAA Aerospace Sciences Meeting and Exhibit* .

Ahuja, S., Rowley, C. W., Kevrekidis, I. G. & Wei, M. 2007 Low-dimensional models for control of leading-edge vortices: Equilibria and linearized models. *AIAA Paper 2007-709, 45th AIAA Aerospace Sciences Meeting and Exhibit* .

Åkervik, E., Ehrenstein, U., Gallaire, F. & Henningson, D. S. 2008 Global two-dimensional stability measures of the flat plate boundary-layer flow. *Eur. J. Mech. B/Fluids* In press.

Åkervik, E., Hœpffner, J., Ehrenstein, U. & Henningson, D. S. 2007 Optimal growth, model reduction and control in a separated boundary-layer flow using global eigenmodes. *J. Fluid. Mech.* **579**, 305–314.

Albarède, P. & Monkewitz, P. A. 1992 A model for the formation of oblique shedding and "chevron" patterns in cylinder wakes. *Phys. Fluids A* **4**, 744–756.

Anderson, B. & Moore, J. 1990 *Optimal control: Linear Quadratic Methods*. New York: Prentice Hall.

Andersson, P., Berggren, M. & Henningson, D. 1999 Optimal disturbances and bypass transition in boundary layers. *Phys. Fluids* **11**, 134–150.

Antoulas, A., Sorensen, D. & Gugercin, S. 2001 A survey of model reduction methods for large-scale systems. *Contemp. Math* **280**, 193–219.

Antoulas, C. A. 2005 *Approximation of Large-Scale Dynamical Systems*. Philadelphia: SIAM.

Bamieh, B. & Dahleh, M. 2001 Energy amplification in channel flows with stochastic excitation. *Phys. Fluids* **13**, 3258–3269.

Bewley, T. & Moin, P. 1994 Optimal control of turbulent channel flows. In *Active Control of Vibration and Noise* (ed. E. W. H. K.W. Wang, A. H. Von Flotow R. Shoureshi & T. W. Farabee). ASME DE-Vol. 75.

Bewley, T. R. 2001 Flow control: New challenges for a new renaissance. *Progr. Aerospace. Sci.* **37**, 21–58.

Bewley, T. R. & Liu, S. 1998 Optimal and robust control and estimation of linear paths to transition. *J. Fluid Mech.* **365**, 305–349.

Bewley, T. R., Moin, P. & Temam, R. 2001 Dns-based predictive control of turbulence: An optimal benchmark for feedback algorithms. *J. Fluid Mech.* **447**, 179–225.

Biau, D. & Bottaro, A. 2004 Transient growth and minimal defects: Two possible initial paths of transition to turbulence in plane shear flows. *Phys. Fluids* **16**, 3515–3529.

Briggs, R. J. 1964 Electron-stream interaction with plasmas. *MIT Press* .

Butler, K. & Farrell, B. F. 1992 Three-dimensional optimal perturbations in viscous shear flow. *Phys. Fluids A* **4**, 1637–1650.

Chevalier, M., Hœpffner, J., Åkervik, E. & Henningson, D. S. 2007 Linear

feedback control and estimation applied to instabilities in spatially developing boundary layers. *J. Fluid Mech.* **588**, 163–187.

Chevalier, M., Hœpffner, J., Bewley, T. R. & Henningson, D. S. 2006 State estimation in wall-bounded flow systems. part 2: Turbulent flows. *J. Fluid Mech.* **552**, 167–187.

Choi, H., Moin, P. & Kim, J. 1994 Active turbulence control for drag reduction in wall-bounded flows. *J. Fluid Mech.* **262**, 75–110.

Chomaz, J., Huerre, P. & Redekopp, L. 1987 Models of hydrodynamic resonances in separated shear flows. *Symposium on Turbulent Shear Flows, 6th, Toulouse, France* .

Chomaz, J., Huerre, P. & Redekopp, L. 1988 Bifurcations to local and global modes in spatially developing flows. *Phys. Rev. Lett.* **60**, 25–28.

Chomaz, J., Huerre, P. & Redekopp, L. 1990 The effect of nonlinearity and forcing on global modes. In *New Trends in Nonlinear Dynamics and Pattern-Forming Phenomena* (ed. P. Coullet & P. Huerre), pp. 259–274. New York: NATO ASI Ser. B.

Chomaz, J., Huerre, P. & Redekopp, L. 1991 A frequency selection criterion in spatially developing flows. *Stud. Appl. Math.* **84**, 119-114.

Chomaz, J. M. 2005 Global instabilities in spatially developing flows: Non-normality and nonlinearity. *Ann. Rev. Fluid Mech.* **37**, 357–392.

Cohen, K., Siegel, S., McLaughlin, T., Gillies, E. & Myatt, J. 2005 Closed-loop approaches to control of a wake flow modeled by the ginzburg-landau equation. *Comp. & Fluids* **34**, 927–949.

Corbett, P. & Bottaro, A. 2001 Optimal linear growth in swept boundary layers. *J. Fluid. Mech.* **435**, 1–23.

Cossu, C. & Chomaz, J. M. 1997 Global measures of local convective instabilities. *Phys. Rev. Lett.* **78**, 4387–4390.

Datta, B. 2003 *Numerical Methods for Linear Control Systems Design and Analysis*. New York: Elsevier.

Davies, E. B. 2002 Non-self-adjoint differential operators. *Bull. London Math. Soc.* **34**, 513-532.

Doyle, J. Aug 1978 Guaranteed margins for LQG regulators. *Automatic Control, IEEE Transactions* **23**, 756–757.

Doyle, J., Glover, K., Khargonekar, P. & Francis, B. Aug 1989 State-space solutions to standard H2 and H∞ control problems. *Automatic Control, IEEE Transactions* **34**, 831–847.

Ehrenstein, U. & Gallaire, F. 2005 On two-dimensional temporal modes in spatially evolving open flows: The flat-plate boundary layer. *J. Fluid Mech.* **536**, 209–218.

Farrell, B. F. 1988 Optimal excitation of perturbations in viscous shear flow. *Phys. Fluids* **31**, 2093–2102.

Farrell, B. F. & Ioannou, P. J. 1993 Stochastic forcing of the linearized navier–stokes equations. *Phys. Fluids* **5**, 2600–2609.

Farrell, B. F. & Ioannou, P. J. 1996 Generalized stability theory. part i. autonomous operators. *J. Atmos. Sci.* **53**, 2025–2040.

Gal-El-Hak, M. 1996 Modern developments in flow control. *Appl. Mech. Rev.* **49**, 365–379.

Gal-El-Hak, M. 2000 *Flow Control: Passive, Active And Reactive Flow Management*. London: Cambridge University Press.

Giannetti, F. & Luchini, P. 2007 Structural sensitivity of the first instability of the cylinder wake. *J. Fluid Mech.* **581**, 167–197.

Gillies, E. A. 1998 Low-dimensional control of the circular cylinder wake. *J. Fluid Mech.* **371**, 157–178.

Green, M. & Limebeer, J. N. 1995 *Linear Robust Control*. New Jersey: Prentice Hall.

Guégan, A., Schmid, P. J. & Huerre, P. 2006 Optimal energy growth and optimal control in swept hiemenz flow. *J. Fluid Mech.* **566**, 11–45.

Gunzburger, M. 1995 *Flow Control*. Berlin: Springer.

Henningson, D. & Åkervik, E. 2008 The use of global modes to understand transition and perform flow control. *Phys. Fluids* **20**, 031302.

Hill, D. 1995 Adjoint systems and their role in the receptivity problem for boundary layers. *J. Fluid. Mech.* **292**, 183–204.

Ho, C. M. & Huerre, P. 1984 Perturbed free shear layers. *Ann. Rev. Fluid Mech* **16**, 365–424.

Hœpffner, J. 2006 *Stability and Control of Shear Flows Subject to Stochastic Excitations*. KTH Stockholm, ph.D. Dissertation.

Hœpffner, J. & Brandt, L. 2008 Stochastic approach to the receptivity problem applied to bypass transition in boundary layers. *Phys. Fluids* **20**, 024108.

Hœpffner, J., Chevalier, M., Bewley, T. R. & Henningson, D. S. 2005 State estimation in wall-bounded flow systems. part i: Laminar flows. *J. Fluid Mech.* **534**, 263–294.

Högberg, M. 2001 *Optimal control of boundary-layer transition*. KTH Stockholm, ph.D. Dissertation.

Högberg, M., Bewley, T. R. & Henningson, D. S. 2003*a* Linear feedback control and estimation of transition in plane channel flow. *J. Fluid Mech.* **481**, 149–175.

Högberg, M., Bewley, T. R. & Henningson, D. S. 2003*b* Relaminarization of $re_tau = 100$ turbulence using gain scheduling and linear state-feedback control flow. *Phys. Fluids* **15**, 3572–3575.

Huerre, P. 2000 Open shear flow instabilities. In *Perspectives in Fluid Dynamics*, pp. 159–229. Cambridge University Press.

Huerre, P. & Monkewitz, P. A. 1990 Local and global instabilities in spatially developing flows. *Ann. Rev. Fluid Mech.* **22**, 471–573.

Hunt, R. E. & Crighton, D. G. 1991 Instability of flows in spatially developing media. *Proc. R. Soc. Lond. A* **435**, 109–128.

Ilak, M. & Rowley, C. W. 2008 Modeling of transitional channel flow using balanced proper orthogonal decomposition. *Phys. Fluids* **20**, 034103.

Joshi, S. S., Speyer, J. L. & Kim, J. 1997 A systems theory approach to the feedback stabilization of infinitesimal and finite-amplitude disturbances in plane poiseuille flow. *J. Fluid Mech.* **332**, 157–184.

Joslin, R. D. 1998 Aircraft laminar flow control. *Ann. Rev. Fluid Mech* **30**, 1–29.

Jovanovic, M. R. & Bamieh, B. 2005 Componentwise energy amplification in channel flows. *J. Fluid Mech.* **534**, 145–183.

Kailath, T. 1973 Some new algorithms for recursive estimation in constant linear systems. *IEEE Trans. Inf. Theory* **19**, 750–760.

Kailath, T. 1980 *Linear Systems*. Englewood Cliffs: Prentice-Hall.

Kalman, R. E. 1960 A new approach to linear filtering and prediction problems. *Trans. ASME, Ser. D. J. Basic Eng.* **82**, 24–45.

Kim, J. 2003 Control of turbulent boundary layers. *Phys. Fluids* **15**, 1093–1105.

Kim, J. & Bewley, T. R. 2007 A linear systems approach to flow control. *Ann. Rev. Fluid Mech.* **39**, 383–417.

Kwakernaak, H. & Sivan, R. 1972 *Linear Optimal Control Systems*. New York: Wiley Interscience.

Laub, A. 1991 Invariant subspace methods for the numerical solution of riccati equations. In *The Riccati equation* (ed. W. Bittaini, Laub), pp. 163–96. Berlin: Springer.

Lauga, E. & Bewley, T. R. 2003 The decay of stabilizability with reynolds number in a linear model of spatially developing flows. *Proc. R. Soc. Lond. A.* **459**, 2077–2095.

Lauga, E. & Bewley, T. R. 2004 Performance of a linear robust control strategy on a nonlinear model of spatially developing flows. *J. Fluid Mech.* **512**, 343–374.

Le Dizés, S., Huerre, P., Chomaz, J. M. & Monkewitz, P. A. 1996 Linear global modes in spatially developing media. *Phil. Trans. R. Soc. Lond. A* **354**, 169–212.

Lee, K. H., Cortelezzi, L., Kim, J. & Speyer, J. 2001 Application of reduced-order controller to turbulent flow for drag reduction. *Phys. Fluids* **13**, 1321–1330.

Lesshafft, L., Huerre, P., Sagaut, P. & Terracol, M. 2006 Nonlinear global modes in hot jets. *J. Fluid Mech.* **554**, 393–409.

Lewis, F. L. & Syrmos, L. V. 1995 *Optimal Control*. New York: John Wiley & Sons.

Luchini, P. 2000 Reynolds-number-independent instability of the boundary layer over a flat surface: Optimal perturbations. *J. Fluid. Mech.* **404**, 289–309.

Luchini, P. & Bottaro, A. 1998 Gortler vortices: a backward-in-time approach to the receptivity problem. *J. Fluid. Mech.* **363**, 1–23.

Lumley, J. L. 1970 *Stochastic Tools in Turbulence*. Academic Press.

Marquillie, M. & Ehrenstein, U. 2002 On the onset of nonlinear oscillations in a separating boundary-layer flow. *J. Fluid Mech.* **458**, 407–417.

Moin, P. & Bewley, T. R. 1994 Feedback control of turbulence. *Appl. Mech. Rev.* **47** (6).

Monkewitz, P. 1989 Feedback control of global oscillations in fluid systems. *AIAA Paper 89-0991* .

Monkewitz, P. 1990 The role of absolute and convective instability in predicting the behavior of fluid systems. *Eur. J. Mech., B/Fluids* **9**, 395–413.

Monkewitz, P. A., Williamson, C. H. K. & Miller, G. D. 1996 Phase dynamics of Kármán vortices in cylinder wakes. *Phys. Fluids* **8**, 91.

Monokrousos, A., Brandt, L., Schlatter, P. & Henningson, D. S. 2008 Dns and les of estimation and control of transition in boundary layers subject to free-stream turbulence. *Int. J. Heat Fluid Flow* Submitted.

Moore, B. Feb 1981 Principal component analysis in linear systems: Controllability, observability, and model reduction. *Automatic Control, IEEE Transactions* **26** (1), 17–32.

Nichols, J. W., Schmid, P. J. & Riley, J. J. 2007 Self-sustained oscillations in variable-density round jets. *J. Fluid Mech.* **582**, 341–376.

Obintata, G. & Andersson, B. D. 2001 *Model Reduction for Control System Design*. New York: Springer.

Park, D. S., Ladd, D. M. & W., H. E. 1993 Feedback control of a global mode in spatially developing flows. *Phys. Lett. A.* **182**, 244–248.

Pier, B. 2002 On the frequency selection of finite-amplitude vortex shedding in the cylinder wake. *J. Fluid Mech.* **458**, 407–417.

Provansal, M., Mathis, C. & Boyer, L. 1987 Bénard-von Kármán instability: Transient and forcing regimes. *J. Fluid. Mech.* **182**, 1–22.

Reddy, S. & Henningson, D. 1993 Energy growth in viscous channel flows. *J. Fluid Mech.* **252**, 209–238.

Reddy, S., Schmid, P. & Henningson, D. 1993 Pseudospectra of the orr-sommerfeld operator. *SIAM J. Appl. Math.* **53** (1), 15–47.

Roussopoulos, K. & Monkewitz, P. 1996 Nonlinear modeling of vortex shedding control in cylinder wakes. *Physica D* **97**, 264–273.

Rowley, C. W. 2005 Model reduction for fluids using balanced proper orthogonal decomposition. *Int. J. Bifurc. Chaos* **15** (3), 997–1013.

van der Schaft, A. J. 1991 Duality for linear systems: External and state space characterization of the adjoint problem. In *Analysis of controlled dynamical systems* (ed. B. B. etal), pp. 393–403. Boston: Birkhäuser.

Schmid, P. J. 2007 Nonmodal stability theory. *Ann. Rev. Fluid Mech.* **39**, 129–62.

Schmid, P. J. & Henningson, D. S. 2001 *Stability and Transition in Shear Flows*. New York: Springer Verlag.

Sirovich, L. 1987 Turbulence and the dynamics of coherent structures i-iii. *Quart. Appl. Math.* **45**, 561–590.

Skelton, R., Iwasaki, T. & Grigoriadis, K. 1998 *A Unified Algebraic Approach to Linear Control Design*. Taylor & Francis.

Skogestad, S. & Postlethwaite, I. 2005 *Multivariable Feedback Control, Analysis to Design*, 2nd edn. Wiley.

Tang, T. 1993 The Hermite spectral method for Gaussian-type functions. *J. Sci. Comp.* **14**, 594–606.

Trefethen, L. & Bau, D. 1997 *Numerical Linear Algebra.*. Philadelphia: SIAM.

Trefethen, L. & Embree, M. 2005 *Spectra and Pseudospectra — The Behavior of Nonnormal Matrices and Operators*. New Jersey: Princeton University Press.

Trefethen, L., Trefethen, A., Reddy, S. & Driscoll, T. 2005 Hydrodynamic stability without eigenvalues. *Science* **261**, 578–584.

Trefethen, L. N. 1997 Pseudospectra of linear operators. *SIAM Review* **39** (3), 383–406.

Weideman, J. A. & Reddy, S. C. 2000 A matlab differentiation matrix suite. *ACM Trans. of Math. Software* **26**, 465–519.

Willcox, K. & Peraire, J. 2002 Balanced model reduction via the proper orthogonal decomposition. *AIAA J.* **40** (11), 2323–2330.

Zhou, K., Doyle, J. & Glover, K. 2002 *Robust and Optimal Control*. New Jersey: Prentice Hall.

Zhou, K., Salomon, G. & Wu, E. 1999 Balanced realization and model reduction for unstable systems. *Int. J. Robust Nonlinear Control* **9**, 183–198.

Zuccher, S. Luchini, P. & Bottaro, A. 2004 Algebraic growth in a blasius boundary layer: optimal and robust control by mean suction in the nonlinear regime. *J. Fluid. Mech.* **556**, 189–216.

2

Paper 2

Input-output analysis, model reduction and control of the flat-plate boundary layers

By Shervin Bagheri, Luca Brandt & Dan S. Henningson

Linné Flow Centre, Department of Mechanics
Royal Institute of Technology, S-100 44 Stockholm, Sweden

Submitted to the Journal of Fluid Mechanics

The dynamics and control of two-dimensional disturbances in the spatially evolving boundary layer on a flat-plate are investigated from an input-output viewpoint. From the linearized Navier–Stokes equations with inputs (disturbances and actuators) and outputs (objective function and sensor) controllable, observable and balanced modes are extracted using the snapshot-method and a matrix-free time-stepper approach. A balanced reduced-order model is constructed and shown to capture the input-output behavior of linearized Navier–Stokes equations. This model is finally used to design a $\mathcal{H}_2$-feedback controller to suppress the growth of two-dimensional perturbations inside the boundary-layer.

1. Introduction

Many powerful linear systems and control theoretical tools have been out of reach for the fluids community due to the complexity of the Navier–Stokes equations. Two elements that have enabled a systematic approach to flow control are the availability of increasingly powerful computer resources and recent advances of matrix-free methods. In this paper, the linearized Navier–Stokes equations including inputs and outputs are analyzed using systematic tools from linear systems and control theory. The techniques do not rely on physical insight into the specific flow configuration and can in principle be applied to any geometry.

We will focus on the flat-plate geometry which still poses a computational challenge. The two-dimensional Blasius boundary-layer is non-parallel, *i.e.* spatially evolving and therefore has two inhomogeneous spatial directions. Many tools in both stability analysis and control theory rely on the linearized stability operator, which even for two-dimensional flows becomes very large when it is discretized. As an example, a moderate grid resolution with 200 points in two directions leads to a system matrix with a memory demand of 10 Gigabytes, whereas to store a flow field requires only 3 Megabytes. It is therefore essential to either approximate or develop algorithms where large matrices are avoided and the storage demands are of the order of few flow fields. Matrix-free methods

employ the "timestepper approach" in which given a flow field a Navier–Stokes code is used to provide a field at a later time. The time-stepper technique has become increasingly popular in stability analysis, both for computing the largest transient growth and performing asymptotic analysis (Barkley *et al.* 2002). Another example of matrix-free method is the snapshot method introduced by Sirovich (1987), which allows the proper orthogonal decomposition (POD) of flow fields without solving large eigenvalue problems.

The starting point of modern optimal and robust control design, also denoted as $\mathcal{H}_2$– and $\mathcal{H}_\infty$–control, is an input-output formulation referred to as the standard state-space formulation (Zhou *et al.* 1999). The well-known stochastic approach to optimal control referred to as LQG (Linear Quadratic Gaussian) is an example of a $\mathcal{H}_2$ controller. In the $\mathcal{H}_2$ framework three inputs and two outputs are considered; the inputs represent external disturbances, measurement noise and the actuator whereas the outputs represent measurements for estimation and the objective functional to be minimized. The control problem is to supply the actuator with an optimal signal based on the measurements taken from the first sensor, such that the effect of external disturbances and measurement noise on the disturbance energy is minimized at the location of the second sensor. Given the physical distribution of the inputs and outputs, the control design process amounts to the determination of input signals given output signals. Therefore, for successful control design it is sufficient to capture only a fraction of the dynamics, namely the relationships between the input and output signals.

The aim of this study is to build a model of low dimension that captures the input-output behavior of the flat-plate boundary layer, and use this model for optimal feedback control design. With the help of the adjoint Navier–Stokes equations two fundamental dynamical structures are identified; (i) the flow structures that are influenced by the inputs (ii) the flow structures that the outputs are sensitive to. These controllable and observable structures determine the input-output behavior completely for linear systems. It is well-known in systems theory that these two set of modes can be balanced, and represented by one set of modes, called the balanced modes. In this way, the flow structures that capture most of the input-output behavior are extracted and used as projection basis for model reduction. The method employed in this work to compute the balanced modes is called the snapshot-based balanced truncation (Rowley 2005; Willcox & Peraire 2002). This method has been applied to the channel flow (Ilak & Rowley 2008) and the flow around a pitching airfoil (Ahuja *et al.* 2007).

Previous work in flow control involving model reduction and control design has typically relied on physical insight into the specific flow situation rather than on a systematic approach detached from the application (see Kim & Bewley 2007, for a recent review). For instance, for parallel flows it is possible to decouple the linear equations in Fourier space. Control, estimation and other

types of optimization can then be performed independently for each wavenumber and then transformed back to physical space. This approach has been adopted for channel flow in Högberg *et al.* (2003) and even extended to weakly nonparallel flows by Chevalier *et al.* (2007*a*). Another example is the projection of the linearized Navier–Stokes equations on a set of modes such as global eigenmodes of the stability operator or POD modes. Although, these methods have been applied with considerable success to various flows (Gillies 1998; Åkervik *et al.* 2007) their success is strongly dependent on the dynamics of the specific flow situation. For many open shear flows the global eigenmodes and their associated adjoint modes can become widely separated in the streamwise direction (Chomaz 2005) and gradually move away from the locations of the inputs and outputs (Lauga & Bewley 2003). As a consequence controllability and observability of the global eigenmodes is gradually diminished. If controllability/observability is lost for any unstable eigenmode, no control scheme will be able to stabilize the system. The POD basis also has limitations for describing the input-output behavior. Although it is optimal for capturing the energy of the response to an input, it does not always capture the input itself and takes no consideration of the output. However, examples of successful adaptations of POD modes can be found e.g. in Noack *et al.* (2003); Siegel *et al.* (2008) for the globally unstable flow past a circular cylinder.

The paper is organized as follows: we start with describing the flow domain, the inputs, outputs and the control problem in section 2. In this section the mathematical framework is presented with evolution, controllability and observability operators and their associated adjoint operators. These operators are used to introduce the Gramians and balanced modes in section 3, where we also investigate the input-output behavior of our linear system and discuss the most controllable, observable and balanced modes. In section 4 the impulse and harmonic response of the balanced reduced-order model are compared to the full Navier–Stokes equations and the model reduction error is quantified. Section 5 deals with the control design. We briefly introduce the $\mathcal{H}_2$ framework and evaluate the closed-loop performance. Concluding remarks and a summary of the presented material are offered in the last section. Finally, in the appendix we derive the adjoint operators, describe the snapshot method, the solution of the $\mathcal{H}_2$ problem and our time-stepper.

2. Problem formulation

2.1. *Governing equations*

We consider the linear spatio-temporal evolution of two-dimensional disturbances in a viscous, incompressible flow over a flat plate. The geometry of the problem and the physical domain, $\Omega = (0, L_x) \times (0, L_y)$, are shown in figure 1. The disturbance behavior is governed by the Navier–Stokes equations linearized

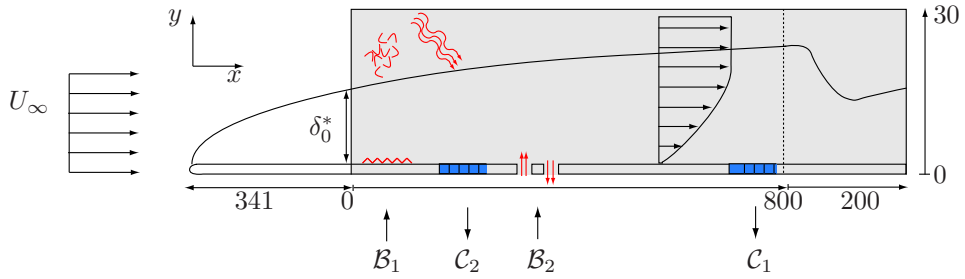

FIGURE 1. The input/output configuration used for the control of perturbations in a two-dimensional flat-plate geometry. The computational domain $\Omega = (0, L_x) \times (0, L_y)$, shown by the gray region, extends from $x = 0$ to $x = 1000$ with the fringe region starting at $x = 800$. The first input $\mathcal{B}_1$, located at $(x_{\mathsf{w}}, y_{\mathsf{w}}) = (35, 1)$, models the initial receptivity phase, where disturbances are induced by free-stream turbulence, acoustic waves or wall roughness. The actuator, $\mathcal{B}_2$, provides a mean to manipulate the flow, in this case by a localized volume forcing, and is centered at $(x_{\mathsf{u}}, y_{\mathsf{u}}) = (400, 1)$. Two sensors, $\mathcal{C}_1$ and $\mathcal{C}_2$, are located at $(x_{\mathsf{v}}, y_{\mathsf{v}}) = (300, 1)$ and $(x_{\mathsf{z}}, y_{\mathsf{z}}) = (750, 1)$ respectively. The upstream measurements are used to estimate the incoming perturbations, while the downstream sensor quantifies the effect of the control. Note that in this work all the inputs and outputs are Gaussian functions given by expression (10).

about a spatially evolving zero-pressure-gradient boundary layer,

$$\dot{\boldsymbol{u}} = \mathcal{A}\boldsymbol{u} - \nabla p + \boldsymbol{f}, \tag{1a}$$

$$0 = \nabla \cdot \boldsymbol{u}, \tag{1b}$$

$$\boldsymbol{u} = \boldsymbol{u}_0 \qquad \text{at} \quad t = 0. \tag{1c}$$

The disturbance velocity and pressure field at position $\boldsymbol{x} = (x, y)$ and time t are represented by $\boldsymbol{u}(\boldsymbol{x}, t) = [u, v]^T$ and $p(\boldsymbol{x}, t)$, respectively. The divergence operator is denoted by $\nabla = [\partial_x, \partial_y]^T$, the external forcing by $\boldsymbol{f}(\boldsymbol{x}, t)$ and the governing linear operator $\mathcal{A}$ is

$$\mathcal{A}(\mathrm{Re}, \mathbf{U}, \lambda) = -(\mathbf{U} \cdot \nabla) - (\nabla \mathbf{U}^T)^T + \mathrm{Re}^{-1}\nabla^2 + \lambda(x). \tag{2}$$

The Reynolds number is defined as $\mathrm{Re} = U_\infty \delta_0^* / \nu$, where U_∞ is the free-stream velocity and δ_0^* the displacement thickness at the computational inflow $x_0 = 0$. All the simulations were performed at $\mathrm{Re} = 1000$ which corresponds to a distance of $341\delta_0^*$ from the leading edge to the inlet of the computational domain. The base flow $\mathbf{U} = [U, V]^T(x, y)$ is a solution to the steady nonlinear Navier–Stokes equations.

The term $\lambda(x)$ is used to enforce periodicity of the physical flow in the streamwise direction, so that a spectral Fourier expansion technique can be employed for our numerical solution. This function is nonzero only in a fringe region at the end of the domain (see figure 1) where it forces the outgoing perturbation amplitude to zero (See Appendix C and Nordström *et al.* 1999, for further details). The solutions to (1) satisfy no-slip condition at the plate and vanish at the upper boundary $L_y = 30\delta_0^*$ which is chosen to be well outside the boundary layer. The boundary conditions hence are

$$[u, v]_{x=0} = [u, v]_{x=L_x}, \tag{3a}$$

$$[u, v]_{y=0} = [u, v]_{y=L_y} = 0. \tag{3b}$$

2.2. *Standard state-space formulation & the $\mathcal{H}_2$ problem*

The Navier–Stokes equations (1) may be written in the *standard state-space form* (Zhou *et al.* 2002) useful for applying tools from systems theory and for $\mathcal{H}_2/\mathcal{H}_\infty$ control design. In this framework, any instantaneous divergence-free disturbance field $\boldsymbol{u}$ that satisfies the boundary conditions (3) is an element of the state-space $\mathbb{X} = L_2(\Omega)$. Furthermore, the forcing $\boldsymbol{f}$, also referred to as the input, is decomposed into external disturbances w and a control u, *i.e.*

$$\boldsymbol{f} = \mathcal{B}_1\mathsf{w} + \mathcal{B}_2\mathsf{u}, \tag{4}$$

where the input signals w, u are functions of time and $\mathcal{B}_1(x, y), \mathcal{B}_2(x, y)$ are linear mappings from $\mathbb{R} \to \mathbb{X}$. The first mapping, $\mathcal{B}_1$, represents the spatial distribution of the sources of external disturbances acting on the flow (see figure 1). In our model, the input forcing $\mathcal{B}_1$ is located at the upstream end of the domain to model the upstream receptivity phase, when disturbances are introduced into the boundary layer by *e.g.* roughness and free-stream perturbations. The actuator used for control is defined by the mapping $\mathcal{B}_2$, which represents a localized volume force, mimicking blowing and suction at the wall. Finally, $\mathsf{u}(t)$ represents the control signal we wish to apply and is based on the sensor measurements.

Information about the disturbance behavior is given by two outputs

$$\mathsf{z} = \mathcal{C}_1\boldsymbol{u} + l\mathsf{u}, \tag{5}$$

$$\mathsf{v} = \mathcal{C}_2\boldsymbol{u} + \alpha\mathsf{g}, \tag{6}$$

where the output signals z, v are functions of time and $\mathcal{C}_1, \mathcal{C}_2$ are functionals from $\mathbb{X} \to \mathbb{R}$. The sensor defined by $\mathcal{C}_1$ is located far downstream and it is used to evaluate the level of the disturbance amplitude. Therefore it reveals whether the "objective" of our control has been met. In particular, the objective is to find a control signal $\mathsf{u}(t)$ such that the perturbation energy in the flow is minimized downstream at the location defined by $\mathcal{C}_1$. To design an efficient controller, however, the energy input expended in the actuation should be limited; thus, the control effort is penalized with a scalar l. For large values of l the control effort is considered to be expensive, whereas small values indicate cheap control.

This results in an objective functional of the form

$$\|\mathsf{z}\| = \|\mathcal{C}_1 \boldsymbol{u}\| + l\|\mathsf{u}\| \tag{7}$$

and explains why the control signal is added to the sensor signal when defining the output signal z. The norms in (7) are associated to the inner products defined in the next section. In the definition of z we have assumed $\langle l\mathsf{u}, \mathcal{C}_1\boldsymbol{u}\rangle = 0$ so that there is no cross weighting between the flow energy and control input (Zhou *et al.* 1999).

The second output signal $\mathsf{v}(t)$ is the measurement signal extracted from the sensor $\mathcal{C}_2$. This signal is the only information delivered to the controller in order to provide a control signal such that the above objective is met. The additional term $\mathsf{g}(t)$ accounts for noise contaminating the measurements. This term can be considered as a third forcing, but rather than forcing the Navier–Stokes equations it forces the measurements. Large values of the scalar α indicate high level of noise corruption in the output signal, whereas for low values of α the measurement v reflects information about the flow field with high fidelity.

The choice of the relative position of the sensor $\mathcal{C}_2$ and actuator $\mathcal{B}_2$ used in the control design process and reported in figure 1 is based on the knowledge of the behavior of boundary layer instabilities. These instabilities are of a convective nature, so unstable waves are amplified while travelling downstream eventually leaving our control domain. As a consequence, the relative streamwise position of the sensor and actuator is related to the flux of information. Since the control signal is based on the measured velocity disturbance, the actuation can be implemented only downstream of the measurement point. In the same way, the effect of the control can be measured only downstream of the actuator. A completely different choice of sensors and actuators may be more appropriate in the case of globally unstable flows (see Bagheri *et al.* 2008), when the whole flow beats at a specific frequency. As example, in the case of feedback control applied to flow separation over a long shallow cavity (Åkervik *et al.* 2007), the measurement sensor was placed at the downstream end of the cavity where the velocity fluctuations reach larger amplitudes, while the actuation was applied at the upstream edge where adjoint modes revealed higher flow sensitivity.

The Navier–Stokes equations (1) with input vector $\mathbf{f} = [\mathsf{w}, \mathsf{g}, \mathsf{u}]^T$ as an element in the input space $\mathbb{U} = \mathbb{R}^3$ and output vector $\mathbf{y} = [\mathsf{z}, \mathsf{v}]^T$ as an element in the output space $\mathbb{Y} = \mathbb{R}^2$ may now be written in the standard state-space form

$$\dot{\boldsymbol{u}} = \mathcal{A}\boldsymbol{u} - \nabla p + \mathcal{B}\mathbf{f} \tag{8a}$$

$$0 = \nabla \cdot \boldsymbol{u} \tag{8b}$$

$$\mathbf{y} = \mathcal{C}\boldsymbol{u} + \mathcal{D}\mathbf{f} \tag{8c}$$

where $\mathcal{C} = [\mathcal{C}_1, \mathcal{C}_2]^T$, $\mathcal{B} = [\mathcal{B}_1, 0, \mathcal{B}_2]$ and

$$\mathcal{D} = \begin{bmatrix} 0 & 0 & l \\ 0 & \alpha & 0 \end{bmatrix}. \tag{9}$$

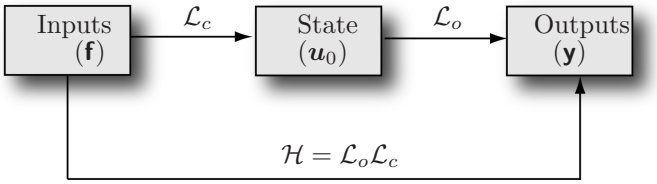

FIGURE 2. The operators used to examine the system input-output behavior. The controllability operator $\mathcal{L}_c$ relates past inputs to the present state, while the observability mapping $\mathcal{L}_o$ relates the present state to the future outputs. Their combined action is expressed by the Hankel operator $\mathcal{H}$.

The system (8) is asymptotically stable, *i.e.* in the global framework all the eigenvalues of the linearized Navier–Stokes system for a spatial boundary layer represent perturbations decaying in time. Note that the pressure gradient and the continuity equation can be removed from (8) by considering only the divergence-free part of the state, *i.e.* projecting the equations on a divergence-free subspace (Chorin & Marsden 1990).

Finally, we define the spatial distribution of the sensors and actuators introduced above. In this work, the input and output operators are modeled with the Gaussian function $h(\boldsymbol{x}, \boldsymbol{x}_0)$, defined as

$$\boldsymbol{h}(\boldsymbol{x};\boldsymbol{x}_0) = \begin{bmatrix} \sigma_x\gamma_y \\ -\sigma_y\gamma_x \end{bmatrix} \exp(-\gamma_x^2 - \gamma_y^2) \tag{10}$$

where

$$\gamma_x = \frac{x - x_0}{\sigma_x}, \qquad \gamma_y = \frac{y - y_0}{\sigma_y}. \tag{11}$$

The scalars (σ_x, σ_y) and (x_0, y_0) determine, respectively, the size and location of the inputs and outputs. They are all of the same size, but located at different streamwise locations, as shown schematically in figure 1. With these definitions we have,

$$\mathcal{B} \;=\; [\boldsymbol{h}(\boldsymbol{x};\boldsymbol{x}_{\mathsf{w}}), 0, \boldsymbol{h}(\boldsymbol{x};\boldsymbol{x}_{\mathsf{u}})] \tag{12}$$

and

$$\mathcal{C}\boldsymbol{u} = \int_\Omega \begin{bmatrix} \boldsymbol{h}(\boldsymbol{x};\boldsymbol{x}_{\mathsf{z}})\boldsymbol{u} \\ \boldsymbol{h}(\boldsymbol{x};\boldsymbol{x}_{\mathsf{v}})\boldsymbol{u} \end{bmatrix} \mathrm{d}x\mathrm{d}y. \tag{13}$$

The particular shape of sensor and actuators implies that the inputs amount to localized volume forcing, whereas the flow measurements are obtained by averaging the velocity field over small domains using the Gaussian function as weights.

Operator	Mapping	Definition	Adjoint operator
Evolution	$\mathbb{X} \to \mathbb{X}$	$\mathcal{T}(t+s)\boldsymbol{u}(t) = \boldsymbol{u}(t+s)$	$\mathcal{T}^*(t-s)\boldsymbol{u}(t) = \boldsymbol{u}(t-s)$
Controllability	$\mathbb{U} \to \mathbb{X}$	$\mathcal{L}_c\mathbf{f}(t) = \int_{-\infty}^{0} \mathcal{T}(-t)\mathcal{B}\mathbf{f}(t)\mathrm{d}t$	$\mathcal{L}_c^*\boldsymbol{u}_0 = \mathcal{B}^*\mathcal{T}^*(-t)\boldsymbol{u}_0$
Observability	$\mathbb{X} \to \mathbb{Y}$	$\mathcal{L}_o(t)\boldsymbol{u} = \mathcal{C}\mathcal{T}(t)\boldsymbol{u}_0$	$\mathcal{L}_o^*(t)\mathbf{f} = \int_0^{\infty} \mathcal{T}^*(t)\mathcal{C}^*\mathbf{f}\mathrm{d}t$
Hankel	$\mathbb{U} \to \mathbb{Y}$	$\mathbf{y} = \mathcal{L}_o(t)\mathcal{L}_c\mathbf{f}$	$\mathbf{f} = \mathcal{L}_c^*(t)\mathcal{L}_o^*\mathbf{y}$

TABLE 1. The linear operators used in this work. See Appendix A for further details and derivations of the adjoint operators.

2.3. *Operators*

When performing model reduction for control design, one wishes to retain the relationship between the inputs and the outputs in the low-order system. Following linear system theory, the properties of the input/output system (8) can be described by the three operators introduced in this section. In the framework presented below we assume that all operators are bounded in the chosen metrics and we refer to Curtain & Zwart (1995) and Dullerud & Paganini (1999) for further mathematical details. See figure 2 and table 2.3 for an overview of the operators.

First, we define a linear evolution operator $\mathcal{T} : \mathbb{X} \to \mathbb{X}$ for the state variable $\boldsymbol{u}$ as

$$\boldsymbol{u}(\boldsymbol{x}, t+s) = \mathcal{T}(t+s)\boldsymbol{u}(\boldsymbol{x}, t). \tag{14}$$

Given a perturbation field at time t, $\mathcal{T}(t+s)$ provides the velocity field at a later time $t+s$. The operator satisfies the following properties $\mathcal{T}(t+s) = \mathcal{T}(t)\mathcal{T}(s)$, $\mathcal{T}(0) = I$. Note that $\mathcal{T}$ can be considered as a semi-group of the form $\exp(\mathcal{A}t)$ on a divergence-free subspace (see *e.g.* Curtain & Zwart 1995).

In this work, the action of the operator is approximated numerically: $\mathcal{T}(t+s)\boldsymbol{u}(\boldsymbol{x}, t)$ is obtained by solving the partial differential equation (1) using a time-stepper (Barkley *et al.* 2002) (*i.e.* a Navier–Stokes solver) with $\boldsymbol{u}(\boldsymbol{x}, t)$ as initial condition. In its simplest form, a time-stepper sets up a grid in space and time and computes approximate solutions on this grid by marching in time. This approach is computationally feasible also for high-order systems since large matrices are not stored. The time-stepper used and the corresponding numerical method are described in Appendix C.

The operators needed to describe the input-output behavior can be related to the formal solution of the system of equations (8), which is

$$\mathbf{y}(t) = \mathcal{C}\mathcal{T}(t)\boldsymbol{u}_0 + \mathcal{C}\int_0^t \mathcal{T}(t-\tau)\mathcal{B}\mathbf{f}(\tau)\mathrm{d}\tau + \mathcal{D}\mathbf{f}(t). \tag{15}$$

This equation can be verified by inserting $\mathcal{T} = \exp(\mathcal{A}t)$ into (15) and using (8). In the expression above, we identify the first term on the right-hand side with the homogeneous solution and the second term with the particular solution stemming from the forcing $\mathbf{f}$. Note that in our case the forcing term is an element in $\mathbb{X}$, *i.e.* divergence-free and satisfies the boundary conditions. For a

more general forcing $\boldsymbol{f}$, only the divergence-free part of the forcing $\hat{\boldsymbol{f}}$ will affect the output signal. The difference $\hat{\boldsymbol{f}} - \boldsymbol{f}$ can be written as the gradient of a scalar and thus will only modify the pressure (Bewley *et al.* 2000). The third part of expression (15) relates the input to the output through the matrix $\mathcal{D}$ without any operators involved. Without loss of generality, we will neglect this term for now and consider it again in section 5 for control design.

In systems theory, the quantitative investigation of the input-output properties of a linear system is commonly performed through the mappings sketched in figure 2. We begin by introducing the controllability operator $\mathcal{L}_c : \mathbb{U} \rightarrow \mathbb{X}$,

$$\boldsymbol{u}_0 = \mathcal{L}_c \mathbf{f}(t) = \int_{-\infty}^{0} \mathcal{T}(-\tau)\mathcal{B}\mathbf{f}(\tau)\mathrm{d}\tau. \tag{16}$$

This operator describes the mapping of any input $\mathbf{f}(t)$ with $t \in (-\infty, 0]$ onto the state vector $\boldsymbol{u}$ at the reference time $t = 0$. The action of $\mathcal{L}_c$ can be numerically computed by a time-stepper. It amounts to solving the linearized Navier–Stokes equations for the velocity field $\boldsymbol{u}$ with forcing term $\mathbf{f}(t)$ and zero initial conditions. The observability operator $\mathcal{L}_o : \mathbb{X} \rightarrow \mathbb{Y}$ is defined as

$$\mathbf{y}(t) = \mathcal{L}_o(t)\boldsymbol{u}_0 = \mathcal{C}\mathcal{T}(t)\boldsymbol{u}_0. \tag{17}$$

This operator describes the mapping of any initial velocity field $\boldsymbol{u}_0$ to the output signal $\mathbf{y}(t)$. The action of $\mathcal{L}_o(t)$ can also be numerically computed and it amounts to extracting the output signal while solving the linearized Navier–Stokes equations with the initial condition $\boldsymbol{u}_0$ at the reference time $t = 0$ and zero forcing.

A direct mapping between input and output can be obtained as the combination of the operators just introduced (see figure 2),

$$\mathbf{y}(t) = \mathcal{L}_o\mathcal{L}_c\mathbf{f}(t) = \int_{-\infty}^{0} \mathcal{C}\mathcal{T}(t-\tau)\mathcal{B}\mathbf{f}(\tau)\mathrm{d}\tau. \tag{18}$$

This expression can be interpreted as a mapping from past inputs to future outputs. It can be shown that equation (18) is the formal solution for a system which is forced by $\mathbf{f}(t)$ in the time interval $t \in (-\infty, 0]$, resulting in the flow field $\boldsymbol{u}_0$ at $t = 0$. The output is extracted for $t \geq 0$, corresponding to the signal $\mathbf{y}(t)$ produced by the initial condition $\boldsymbol{u}_0$. Expression (18) is also the starting point for the input-output analysis leading to systematically finding reduced order approximations. The mapping from inputs to outputs given by (18) in terms of $\mathcal{L}_c$ and $\mathcal{L}_o$ is called Hankel operator and is denoted by $\mathcal{H}$, *i.e.*,

$$\mathbf{y}(t) = \mathcal{L}_o(t)\mathcal{L}_c\mathbf{f} = (\mathcal{H}\mathbf{f})(t). \tag{19}$$

We have two different representations of the input-output behavior of the flow system; (i) the state-space representation (8) and (ii) the Hankel operator $\mathcal{H}$ defined in (19). Note that in the latter case it is assumed that inputs and outputs are not active at the same time.

2.4. *Adjoint equations and operators*

Before issues related to controllability, observability and model reduction can be considered the adjoint linear operators corresponding to $(\mathcal{T}, \mathcal{L}_c, \mathcal{L}_o)$ must be introduced. The adjoint variables provide information about how variations in the velocity field affect the system output and how variations in the forcing affect the flow. We show that the adjoint operators can be associated with the adjoint linearized Navier–Stokes equations in state-space form, where the role of the inputs and outputs is reversed. The operators $(\mathcal{T}^*, \mathcal{L}_c^*, \mathcal{L}_o^*, \mathcal{C}^*, \mathcal{B}^*)$ and adjoint Navier–Stokes equations are derived in Appendix A. The derivations in the make use of the following definitions of inner products in, respectively, the state ($\mathbb{X}$), input ($\mathbb{U}$) and output ($\mathbb{Y}$) space,

$$\langle \boldsymbol{u}, \boldsymbol{p} \rangle_{\mathbb{X}} = \int_\Omega \boldsymbol{u}^T \boldsymbol{p} \, \mathrm{d}x\mathrm{d}y, \qquad \forall \; \boldsymbol{u}, \boldsymbol{p} \in \mathbb{X}, \tag{20a}$$

$$\langle \mathbf{f}, \mathbf{y} \rangle_{\mathbb{U}} = \mathbf{f}^T \mathbf{y}, \qquad \forall \; \mathbf{f}, \mathbf{y} \in \mathbb{U}, \tag{20b}$$

$$\langle \mathbf{f}, \mathbf{y} \rangle_{\mathbb{Y}} = \mathbf{f}^T \mathbf{y}, \qquad \forall \; \mathbf{f}, \mathbf{y} \in \mathbb{Y}. \tag{20c}$$

Note that the kinetic energy of a perturbation $\boldsymbol{u}$ at time t is measured by $\|\boldsymbol{u}(t)\|_{\mathbb{X}}^2$. The adjoint of the unforced ($\boldsymbol{f} = 0$) linearized Navier–Stokes equations (1) associated with inner product (20a) is

$$-\dot{\boldsymbol{p}} = \mathcal{A}^* \boldsymbol{p} + \nabla \sigma, \tag{21a}$$

$$0 = \nabla \cdot \boldsymbol{p}, \tag{21b}$$

$$\boldsymbol{p} = \boldsymbol{p}_T \qquad \text{at} \quad t = T, \tag{21c}$$

where

$$\mathcal{A}^* = \; (\mathbf{U} \cdot \nabla) - (\nabla \mathbf{U})^T + \mathrm{Re}^{-1} \nabla^2 + \lambda(x). \tag{22a}$$

This system of equations describes the evolution of adjoint flow field $\boldsymbol{p}(\boldsymbol{x}, t) = [u^*, v^*]^T$ backwards in time. The term σ denotes the adjoint pressure field; the boundary conditions for $\boldsymbol{p}$ are given in A.1.

The evolution operator associated with (21) is

$$\boldsymbol{p}(\boldsymbol{x}, t) = \mathcal{T}^*(t) \boldsymbol{p}(\boldsymbol{x}, t + s), \tag{23}$$

so that given an adjoint field at time $t+s$ the adjoint evolution operator provides a solution at an earlier time t. Again, the above operator is approximated numerically using a time-stepper solving equations (21). In A.1 it is shown that $\mathcal{T}^*$ is in fact the adjoint of $\mathcal{T}$ under the inner product (20a).

The adjoint linearized Navier–Stokes equations and its corresponding evolution operator form the basis of the adjoint input-output system dual to (8). This can be obtained in three steps; (i) derive the adjoint input and output operators $\mathcal{B}^*$ and $\mathcal{C}^*$ (ii) use $\mathcal{B}^*$, $\mathcal{C}^*$ and $\mathcal{T}^*$ to derive the adjoint controllability and observability operator $\mathcal{L}_c^*$ and $\mathcal{L}_o^*$ (iii) identify the adjoint state-space with the system which is associated with $\mathcal{L}_c^*$ and $\mathcal{L}_o^*$.

The adjoint of the input and output operators $\mathcal{B}$ and $\mathcal{C}$ associated with the inner products (20b) and (20c) are,

$$\mathcal{C}^* \quad = \quad [\mathcal{C}_1^*, \mathcal{C}_2^*] = [h(\boldsymbol{x};\boldsymbol{x}_\mathsf{z}), h(\boldsymbol{x};\boldsymbol{x}_\mathsf{v})], \tag{24}$$

and

$$\mathcal{B}^*\boldsymbol{p} \quad = \quad \begin{bmatrix} \mathcal{B}_1^*\boldsymbol{p} \\ 0 \\ \mathcal{B}_2^*\boldsymbol{p} \end{bmatrix} = \int_\Omega \begin{bmatrix} h(\boldsymbol{x};\boldsymbol{x}_\mathsf{w})\boldsymbol{p} \\ 0 \\ h(\boldsymbol{x};\boldsymbol{x}_\mathsf{u})\boldsymbol{p} \end{bmatrix} \mathrm{d}\boldsymbol{x}, \tag{25}$$

respectively.

The adjoint controllability and observability operators $\mathcal{L}_c^*$ and $\mathcal{L}_o^*$ associated with the inner products (20b) and (20c) (derived in A.2) are given by

$$\mathcal{L}_c^*(-t)\boldsymbol{p}(x,0) \quad = \quad \mathcal{B}^*\mathcal{T}^*(-t)\boldsymbol{p}(\boldsymbol{x},0) \tag{26a}$$

$$\mathcal{L}_o^*\mathbf{t}(t) \quad = \quad \int_0^\infty \mathcal{T}^*(\tau)\mathcal{C}^*\mathbf{t}(\tau)\ d\tau, \tag{26b}$$

where $\mathbf{t} \in \mathbb{Y}$ and $\boldsymbol{p} \in \mathbb{X}$. The first mapping, $\mathcal{L}_c^*$, is from the adjoint state at time $t = 0$ onto a signal in $\mathbb{U}$ at time $-t$. The mapping $\mathcal{L}_o^*$ is from an output signal in $\mathbb{Y}$ in $t \in (\infty, 0]$ to a state in $\mathbb{X}$ at $t = 0$. In analogy to the case of the forward problem defined by (8), it can be seen that these two mappings are the observability and controllability operator of the following state-space system,

$$-\dot{\boldsymbol{p}} \quad = \quad \mathcal{A}^*\boldsymbol{p} + \nabla\sigma + \mathcal{C}^*\mathbf{t}, \tag{27a}$$

$$0 \quad = \quad \nabla \cdot \boldsymbol{p}, \tag{27b}$$

$$\mathbf{e} \quad = \quad \mathcal{B}^*\boldsymbol{p}, \tag{27c}$$

with initial condition $\boldsymbol{p}(\boldsymbol{x}, T) = \boldsymbol{p}_T$. This system has two inputs contained in the vector $\mathbf{t} = [\mathsf{z}^*, \mathsf{v}^*]$ with $\mathbf{t} \in \mathbb{Y}$ and three outputs contained in the vector $\mathbf{e} = [\mathsf{w}, \mathsf{u}, \mathsf{g}] \in \mathbb{U}$. Comparing the above adjoint equations with (8) we observe that the outputs and inputs have exchanged place. In the dual system (27), the adjoint flow field is forced by the outputs; the adjoint problem will then be used to identify flow fields yielding the largest output response (Dullerud & Paganini 1999).

3. Input-output analysis

In this section, the main input-output characteristics of our problem are analyzed in order to identify the modes to retain in a low-order flow model. We introduce the concepts of Gramians and balancing using the operators defined in the previous section. For a more detailed presentation of systems theory we refer to Kailath (1980) and Curtain & Zwart (1995). The analysis amounts to computing the eigenmodes of three operators; $\mathcal{L}_c\mathcal{L}_c^*$, $\mathcal{L}_o^*\mathcal{L}_o$ and $\mathcal{L}_c^*\mathcal{L}_o^*\mathcal{L}_o\mathcal{L}_c$. The three sets of modes correspond to flow structures that are the most easily influenced by the input (controllable modes), to the states that produce the largest output energy (observable modes) and to the most relevant states for the input-output behavior (balanced modes). For the sake of clarity, we will

show numerical results obtained using only the first input $\mathcal{B}_1$ and the first output $\mathcal{C}_1$ *i.e.* single-input and single-output system (SISO). We will return to the multi-input multi-output (MIMO) state-space system with input vector $\mathbf{f}$ and output vector $\mathbf{y}$ in section 4. The three sets of eigenmodes mentioned above can be computed numerically for high-order systems by using the following two approximations:

(i) *The time-stepper:* As mentioned above, solutions of Navier–Stokes system (8) in input-output form are obtained numerically using a forward time-stepper, which approximates the action of evolution operator $\mathcal{T}$. An adjoint time-stepper is used for computing solutions of the associated adjoint system (27) and the action of the adjoint evolution operator $\mathcal{T}^*$. The numerical code employed is described in Appendix C. In the simulations presented, we have used 768 collocation points in the streamwise direction x and 101 points in the wall-normal direction y, with a computational box of dimensions $L_x = 1000$ and $L_y = 30$ (see figure 1). The discretized system has thus $m \approx 10^5$ degrees of freedom.

(ii) *The snapshot method:* The controllable and observable modes introduced below are computed using the snapshot method introduced by Sirovich (1987). Recently Rowley (2005) extended this method to obtain balanced modes. The snapshot technique is described in Appendix B. For the results presented, the flow structures are computed by collecting 1600 snapshots of the forward simulation using each input as initial condition and 1600 snapshots of the adjoint simulation using each output as initial condition. The snapshots were taken with equal spacing in the time-interval $[0, 4000]$.

3.1. *Controllable modes*

We begin our input-output analysis by searching for flow states that are most easily triggered by a given input. This issue is related to the concept of controllability, which, in general, quantifies the possibility of steering the flow between two arbitrary states. A commonly adopted interpretation of controllability is illustrated by the following optimal control problem: What is the minimum input energy $\|\mathbf{f}\|^2_{L_2}$ in the time span $t \in (-\infty, 0]$ required to bring the state (if possible) from zero to the given initial condition $\boldsymbol{u}(\boldsymbol{x}, 0) = \boldsymbol{u}_0$?

Assuming $\boldsymbol{u}_0$ has an unit norm, it can be shown (Lewis & Syrmos 1995; Dullerud & Paganini 1999) that the optimal input is given by

$$\mathbf{f} = \mathcal{L}_c^* \mathcal{P}^{-1} \boldsymbol{u}_0, \tag{28}$$

where $\mathcal{P}$ is the controllability Gramian defined as

$$\mathcal{P} = \mathcal{L}_c \mathcal{L}_c^* = \int_{-\infty}^{0} \mathcal{T}(-t)\mathcal{B}\mathcal{B}^*\mathcal{T}^*(-t)\mathrm{d}t = \int_{0}^{\infty} \mathcal{T}(t)\mathcal{B}\mathcal{B}^*\mathcal{T}^*(t)\mathrm{d}t. \tag{29}$$

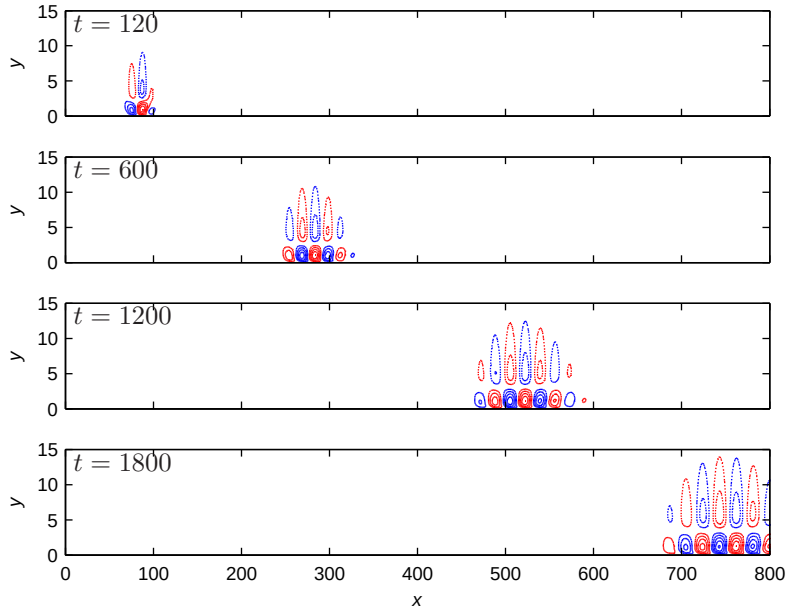

FIGURE 3. Instantaneous snapshots of the streamwise disturbance component at $t = 120, 600, 1200$ and 1800.

In the first equality the expressions (16) and (26a) have been used. Using equation (28) the minimum input energy is given by

$$\|\mathbf{f}\|_{L^2}^2 = \int_\Omega \boldsymbol{u}_0^T \mathcal{P}^{-1} \boldsymbol{u}_0 \mathrm{d}x\mathrm{d}y. \tag{30}$$

The controllability Gramian $\mathcal{P}$ provides a means to rank different states according to how easily they can be influenced by an input. In particular, the most easily influenced, or most controllable, flow structures are the eigenfunctions of $\mathcal{P}$ associated to the largest eigenvalues of,

$$\mathcal{P}\boldsymbol{\phi}_i^c = \lambda_i^c \boldsymbol{\phi}_i^c. \tag{31}$$

The superscript ^{c} stands for controllable modes. Note that by definition of $\mathcal{P}$ the eigenvalues are real and positive and the eigenfunctions mutually orthogonal. If $\lambda_i^c \ll 1$, the corresponding eigenfunction $\boldsymbol{\phi}_i^c$ requires very large energy to be excited by the input since $(\lambda_i^c)^{-1}$ is proportional to $\|\mathbf{f}\|_{L_2}$. The mode is then referred to as nearly uncontrollable[1].

For linear systems the controllability Gramian corresponds to the covariance of the state response to an impulse in time. Therefore, the controllable modes can be regarded as proper orthogonal decomposition (POD) modes (Bagheri

[1]Our use of controllability and observability corresponds to *approximate* controllability and observability in the context of partial differential equations (Curtain & Zwart 1995).

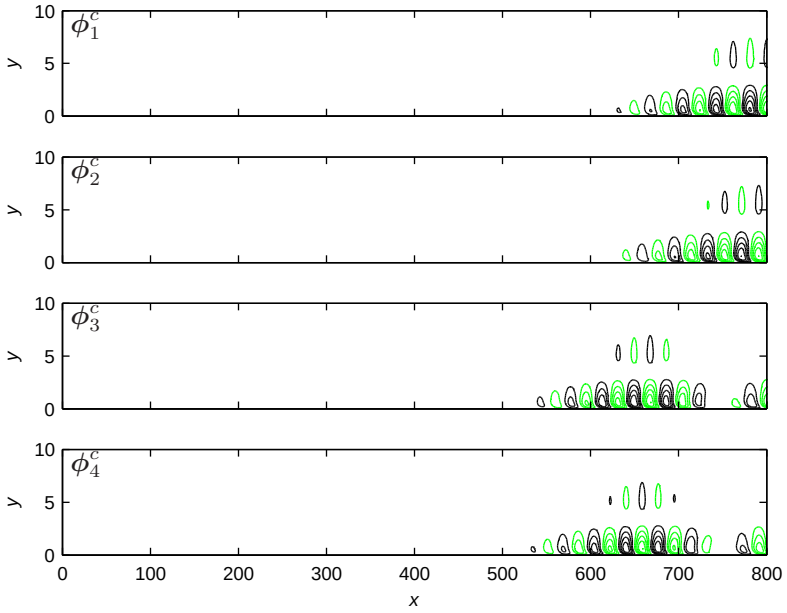

FIGURE 4. The streamwise component of four most controllable modes $\boldsymbol{\phi}_i^c$.

et al. 2008; Ilak & Rowley 2008). Traditionally, the interpretation of these modes is that they represent decorrelated energy-ranked flow states. For example, the first POD mode $\boldsymbol{\phi}_1^c$ is the most energetic structure in the flow containing $\lambda_1^c / \sum_{i=1}^{\infty} \lambda_i^c \times 100$ percent of the total flow energy. These modes can be conveniently obtained by collecting r snapshots of the flow at discrete times $t_1, \ldots, t_r$ and solving a $r \times r$ eigenvalue problem (Sirovich 1987).

The controllable modes can thus be computed from the response of the flow to an impulse, $\delta(0)$,

$$\boldsymbol{u}(\boldsymbol{x}, t_j) = \mathcal{T}(t_j)\mathcal{B}_1. \tag{32}$$

The impulse response can be used to build the Gramian and to compute the most controllable modes as shown in Appendix B. Figure 3 shows the streamwise velocity component of the instantaneous velocity field after an impulse from $\mathcal{B}_1$ at four different times. The generation and convection of a wavepacket with a dominant spatial wavenumber and a propagation speed of about $0.4U_\infty$ can be observed. The wavepacket grows in amplitude and size in the x-direction until it reaches the beginning of the fringe region at $x = 800$. As it enters this region, the disturbance is eventually damped by the fringe forcing reproducing the effect of an outflow. The input-output system (8) is thus asymptotically stable.

The u-component of the four most controllable modes $\boldsymbol{\phi}_i^c$ with respect to $\mathcal{B}_1$ are shown in figure 4, while the corresponding eigenvalues λ_i^c are displayed

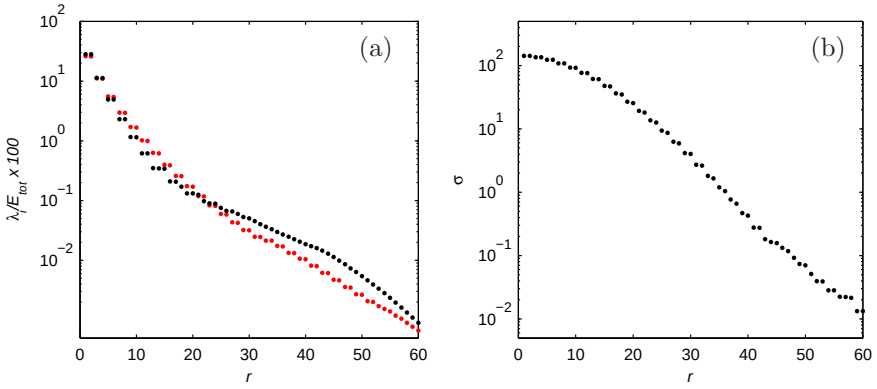

FIGURE 5. (a) The normalized eigenvalues λ_i^c (red symbols) and λ_i^o (black symbols) associated with controllable modes and observable modes respectively. (b) The Hankel singular values σ_i corresponding to the balanced modes.

in figure 5a with red symbols. The first 20 controllable modes contain 99% of the flow energy, meaning that a significant part of the controllable subspace is spanned by 20 modes. Note that the flow structures that are the most easily influenced by the input $\mathcal{B}_1$ are located downstream in the domain, where the energy of the response to forcing is the largest. In other words, low energy is needed at location $\mathcal{B}_1$ to force large structures downstream owing to the amplification provided by the intrinsic flow dynamics. Moreover, the eigenvalues shown in figure 5 come in pairs. The corresponding velocity fields (see the first and the second mode in figure 4) have the same wavepacket structure 90 degrees out of phase. These modes represent traveling structures (see also Rempfer & Fasel 1994).

3.2. *Observable modes*

For a given sensor it is important to determine whether the relevant flow instabilities can be detected, and if so, to which accuracy. The flow fields which can be most easily detected are called the most observable modes. As in the case of the controllability Gramian, the observability problem can also be cast as an optimization problem. We wish to find the initial conditions producing the largest output energy. The output energy generated by the initial condition $\boldsymbol{u}_0$, assumed of unit norm, is given by

$$\|\mathbf{y}\|_{L_2}^2 = \langle \mathcal{L}_o \boldsymbol{u}_0, \mathcal{L}_o \boldsymbol{u}_0 \rangle_{L_2} = \langle \boldsymbol{u}_0, \mathcal{L}_o^* \mathcal{L}_o \boldsymbol{u}_0 \rangle_{\mathbb{X}} = \int_\Omega \boldsymbol{u}_0^T \underbrace{\mathcal{L}_o^* \mathcal{L}_o}_{\mathcal{Q}} \boldsymbol{u}_0 \mathrm{d}x\mathrm{d}y \qquad (33)$$

where $\mathcal{Q}$ is called the observability Gramian. Using equations (17) and (26b) we obtain the following expression for $\mathcal{Q}$

$$\mathcal{Q} = \mathcal{L}_o^* \mathcal{L}_o = \int_0^\infty \mathcal{T}^*(t)\mathcal{C}^*\mathcal{C}\mathcal{T}(t)\mathrm{d}t. \tag{34}$$

The observability Gramian provides a means to rank states according to their contribution to the output. The most observable state $\boldsymbol{\phi}_1^o$ is given by the eigenfunction of the operator $\mathcal{Q}$ corresponding to the largest eigenvalue of,

$$\mathcal{Q}\boldsymbol{\phi}_i^o = \lambda_i^o \boldsymbol{\phi}_i^o. \tag{35}$$

The superscript ^{o} stands for observable modes. Note that $\mathcal{Q}$ is a self-adjoint operator so that its eigenvalues are real and positive and its eigenfunctions mutually orthogonal. The most observable mode, $\boldsymbol{\phi}_1^o$, contributes $\lambda_1^o / \sum_{j=0}^\infty \lambda_j^o \times 100$ percent to the total sensor energy, the second most observable mode, $\boldsymbol{\phi}_2^o$, contributes $\lambda_2^o / \sum_{j=0}^\infty \lambda_j^o \times 100$ percent and so on. In particular, if $\lambda_i^o = 0$, the corresponding mode $\boldsymbol{\phi}_i^o$ does not make a contribution to sensor output, and is called an unobservable mode. Note that the observable modes can regarded as POD modes of the adjoint system.

From the definition of $\mathcal{Q}$ in (34) it follows that the observable modes pertaining a given output can be determined from the impulse response of one adjoint simulation (see Appendix B). The results of this simulation, $\mathcal{T}^*(t)\mathcal{C}^*$, can then be used to build the second order correlation of the flow field, $\mathcal{T}^*(t)\mathcal{C}^*\mathcal{C}\mathcal{T}(t)$, and thus the Gramian. The eigenvalue problem (35) is solved by using the snapshots method as explained above for the case of the controllable modes. Here we present results for the first output $\mathcal{C}_1$ only. Figure 6 shows the instantaneous adjoint field at four different times

$$\boldsymbol{p}(\boldsymbol{x}, t_j) = \mathcal{T}^*(t_j)\mathcal{C}_1^*, \tag{36}$$

after an impulse from the first output, *i.e.* $\mathcal{C}_1^*\delta(0)$. The triggered wavepacket travels backward in time in the upstream direction with upstream tilted structures. The adjoint solution can be regarded as the sensitivity of the output $\mathcal{C}_1$ with respect to linear perturbations to the underlying base flow. In other words, the flow structures excited by $\mathcal{C}_1^*$ and shown in figure 6, are also the structures to which the sensor $\mathcal{C}_1$ is most sensitive. In this context, the negative time can be interpreted as the delay between the time these structures are present and the instant they can be measured.

The u-component of the four most observable modes $\boldsymbol{\phi}_i^o$ with respect to $\mathcal{C}_1$ are shown in figure 7, while the associated eigenvalues are reported in figure 5a (black symbols). From the latter figure, we observe that the leading 20 modes are responsible for nearly the entire output energy. The flow structures in figure 7 are initial conditions that contribute with the most energy to the sensor output. These modes are real-valued functions and therefore two of them are needed to describe traveling flow structures, which explains the appearance of pairs of eigenvalues in figure 5a. The are two further noteworthy remarks:

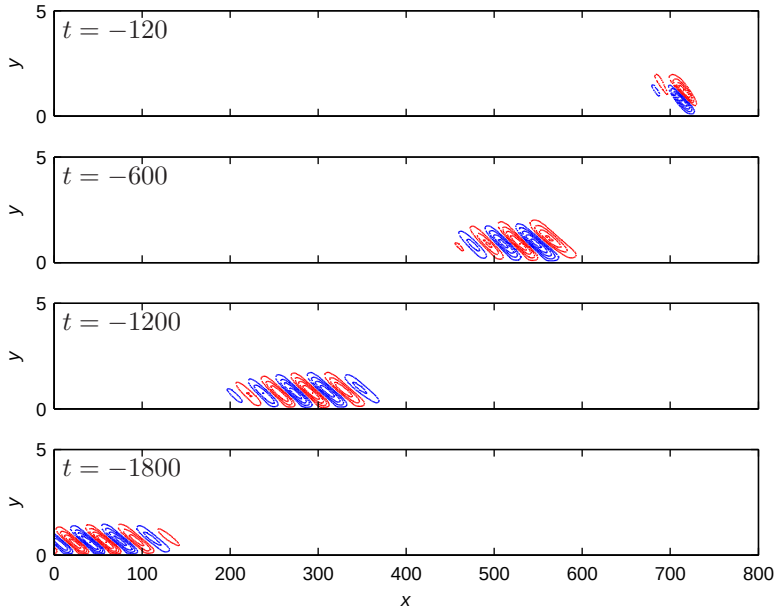

FIGURE 6. Instantaneous snapshots of the streamwise disturbance component at $t = -120, -600, -1200$ and -1800 of the adjoint equations.

(i) The spatial support of the observable modes is far upstream, where the sensitivity of the flow is the largest. Hence, the most observable structures are spatially disconnected from the most controllable modes. This spatial separation is also observed between the global eigenmodes of the linearized Navier–Stokes equations ($\mathcal{A}$) and eigenmodes of the adjoint Navier–Stokes ($\mathcal{A}^*$), where it is associated to streamwise non-normality of the system (Chomaz 2005).

(ii) The most observable structures are tilted in the upstream direction, "leaning" against the shear layer and are similar to the linear optimal disturbances computed by Åkervik *et al.* (2008). The optimal disturbance is the initial condition maximizing the perturbation energy over the entire domain Ω at a fixed time $t = T$. On the other hand, observable modes maximize the time integral of the perturbation energy in the region defined by the output $\mathcal{C}_1$. Choosing the sensor location in correspondence to the largest flow response leads therefore to the similarity between linear optimals and observable modes. As noticed by Butler & Farrell (1992), the upstream tilting of the optimal initial conditions can be attributed to the wall-normal non-normality of the governing operator; perturbations extract energy from the mean shear by transporting momentum down the the mean velocity gradient (the so-called Orr mechanism).

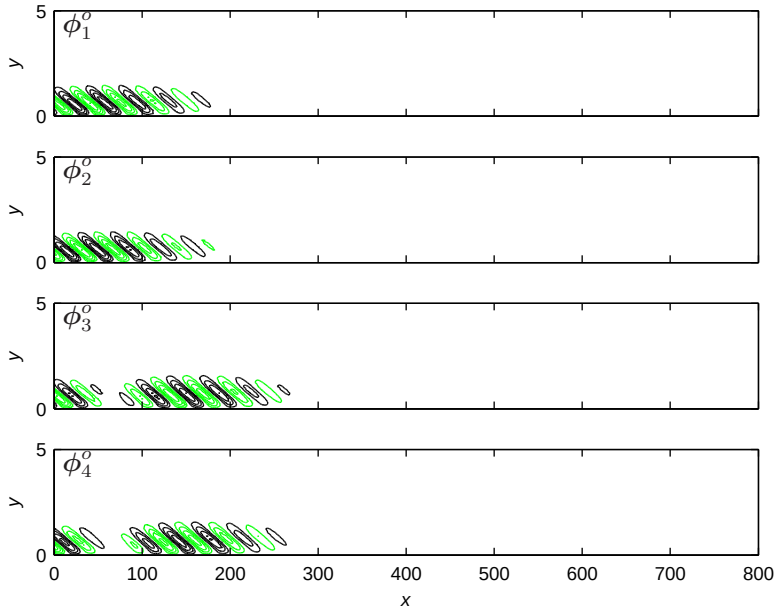

FIGURE 7. The streamwise velocity component of the four most observable modes $\boldsymbol{\phi}_i^o$.

3.3. *Balanced modes*

So far we have identified modes that either characterize the response to forcing or the sensitivity of an output. In this section we present the balanced modes (Moore 1981), which take into account both the response behavior and the output sensitivity. Similar to the previous section, we wish to excite the largest output energy. However, rather than identifying dangerous initial conditions using the mapping $\mathcal{L}_o$ as in equation (33), we look directly for input signals which produce the largest output energy via the input-output mapping $\mathcal{L}_o\mathcal{L}_c$ given in (19).

The output energy generated by the input $\mathbf{f}$, assumed of unit norm, is given at time t by

$$\|\mathbf{y}\|_{L_2}^2 = \langle \mathcal{H}\mathbf{f}, \mathcal{H}\mathbf{f}\rangle_{L_2} = \langle \mathbf{f}, \mathcal{H}^*\mathcal{H}\mathbf{f}\rangle_{L_2} = \int_0^t \mathbf{f}^T \mathcal{H}^*\mathcal{H}\mathbf{f}\mathrm{d}t. \tag{37}$$

If we let the sequence of input vectors $\mathbf{f}_i$ with unit norm represent the eigenfunctions of $\mathcal{H}^*\mathcal{H}$, *i.e.*

$$\mathcal{H}^*\mathcal{H}\mathbf{f}_i = \sigma_i^2 \mathbf{f}_i \tag{38}$$

then the output energy is given by the square of the so called Hankel singular values (HSV) σ_i. The most dangerous input vector $\mathbf{f}_1$ with $\|\mathbf{f}_1\|_{L_2} = 1$ thus results in an output signal which has been amplified by σ_1^2. Note that $\sigma_1 \geq \sigma_2 \geq \ldots$, so the eigenmodes of the input-output map are ranked according to

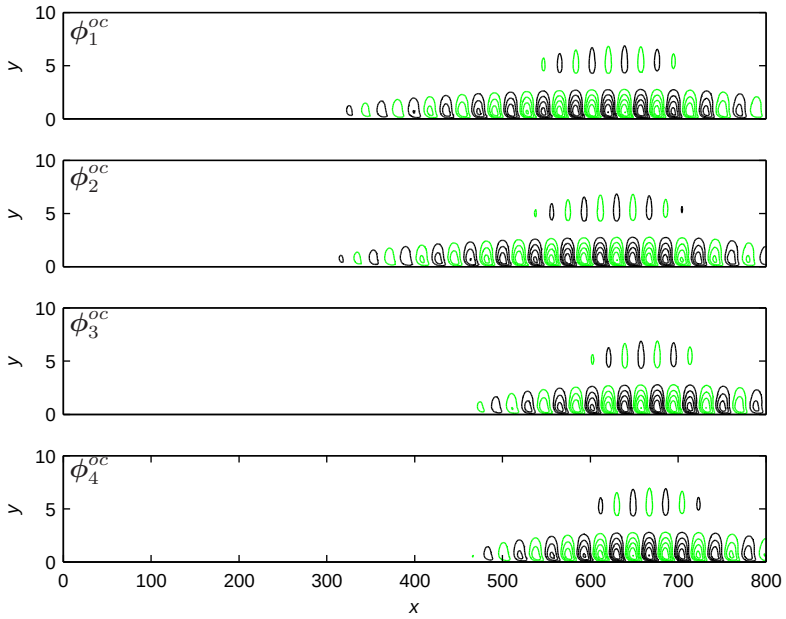

FIGURE 8. The streamwise velocity component of four first balanced modes $\boldsymbol{\phi}_i^{oc}$.

how much the input signal is amplified as it is filtered by the linear system and by the output.

Using the controllability operator $\mathcal{L}_c$ we obtain the flow structure associated with the forcing $\mathbf{f}_i$,

$$\boldsymbol{\phi}_i^{oc} = \frac{1}{\sqrt{\sigma_i}}\mathcal{L}_c\mathbf{f}_i. \tag{39}$$

Notice that $\sigma^{-1/2}$ is a convenient normalization factor. The modes are denoted by the superscript ^{oc}, which indicates that these modes are both observable and controllable. The sequence of functions $\boldsymbol{\phi}_i^{oc}$ are called the balanced modes and as we show next, they diagonalize the observability Gramian. Computing the output energy for $\mathbf{f}_i$ and using (39), we obtain

$$\int_0^t \mathbf{f}_i^T\mathcal{H}^*\mathcal{H}\mathbf{f}_i\mathrm{d}t \quad = \sqrt{\sigma_i}\langle\mathbf{f}_i, \mathcal{L}_c^*\mathcal{Q}\boldsymbol{\phi}_i^{oc}\rangle_{L_2} = \sigma_i\langle\boldsymbol{\phi}_i^{oc}, \mathcal{Q}\boldsymbol{\phi}_i^{oc}\rangle_{\mathbb{X}} = \sigma_i^2, \tag{40}$$

where the definitions $\mathcal{H} = \mathcal{L}_o\mathcal{L}_c$, $\mathcal{H}^* = \mathcal{L}_c^*\mathcal{L}_o^*$ and $\mathcal{Q} = \mathcal{L}_o^*\mathcal{L}_o$ are used. A diagonal observability Gramian implies that these modes can be regarded as orthogonal if this Gramian is used as inner product weight matrix. With respect to inner product defined in (20a) however, these modes are not orthogonal.

A sequence of functions $\boldsymbol{\psi}_i^{oc}$, referred to as the adjoint balanced modes, which is bi-orthogonal to $\boldsymbol{\phi}_i^{oc}$ according to

$$\langle \boldsymbol{\psi}_i^{oc}, \boldsymbol{\phi}_j^{oc} \rangle_{\mathbb{X}} = \delta_{i,j}, \tag{41}$$

is needed to project our system in the basis given by the balanced modes. The derivation is analogous to $\boldsymbol{\phi}_i^{oc}$ but now we consider instead the left eigenvectors, $\mathbf{s}_i$, of the input-output map $\mathcal{H}^*\mathcal{H}$, *i.e.*

$$\mathcal{H}\mathcal{H}^*\mathbf{s}_i = \mathbf{s}_i\sigma_i^2. \tag{42}$$

The adjoint balanced modes are then given by

$$\boldsymbol{\psi}_i^{oc} = \frac{1}{\sqrt{\sigma_i}}\mathcal{L}_o^*\mathbf{s}_i. \tag{43}$$

It is possible to show by the same procedure used in (40) that these modes diagonalize the controllability Gramian,

$$\langle \boldsymbol{\psi}_i^{oc}, \mathcal{P}\boldsymbol{\psi}_i^{oc} \rangle_{\mathbb{X}} = \sigma_i. \tag{44}$$

Furthermore, the diagonal elements are also equal to the HSV. The term balancing now becomes clear; using $\boldsymbol{\phi}_i^{oc}$ and $\boldsymbol{\psi}_i^{oc}$ the controllability and observability Gramians become diagonal and equal to the HSV. In other words, the observability and controllability properties are balanced. This is useful for performing model reduction as it allows us to discard modes which are both difficult to measure and difficult to excite by the inputs.

To compute these modes, it is convenient to show that $\boldsymbol{\phi}_i^{oc}$ are the eigenmodes of $\mathcal{P}\mathcal{Q}$; multiplying (38) with $\mathcal{L}_c$ yields

$$\mathcal{L}_c\mathcal{H}^*\mathcal{H}\mathbf{f}_i = \mathcal{P}\mathcal{Q}\boldsymbol{\phi}_i^{oc} = \sigma_i^2\boldsymbol{\phi}_i^{oc}. \tag{45}$$

The computation of the balanced modes and of their associated adjoints can again be accomplished using a time-stepper and the snapshot method described in Appendix B. In this case one combines the sequence of snapshots collected from the solution of the forward problem (8) with a sequence of snapshots collected from the adjoint system (27). In this way we can approximate the eigenvalue problem (45) to obtain the balanced modes (Rowley 2005). The u-component of four first balanced modes $\boldsymbol{\phi}_i^{oc}$ with respect to $\mathcal{B}_1$ and $\mathcal{C}_1$ are shown in figure 8 and the corresponding adjoint modes $\boldsymbol{\psi}_i^{oc}$ in figure 9. The Hankel Singular values σ_i are shown in figure 5b. As in the case of the observability and controllability eigenvalues λ_i^c and λ_i^o, the singular values come in pairs, indicating that the leading balanced modes are traveling structures. The same observation was made by (Ilak & Rowley 2008) for channel flow.

From figures 8 and 9 we observe that the leading balanced modes appear also as wavepackets but they are somewhat more spatially extended than the controllable POD modes (figure 4). Similarly, the adjoint balanced modes have a larger spatial support than the observable modes (figure 7). As noticed by Ilak & Rowley (2008) and Ahuja *et al.* (2007), we can account for both controllability and observability through the non-orthogonality of the balanced modes. In the two previous sections we observed that for an input $\mathcal{B}_1$ located upstream and

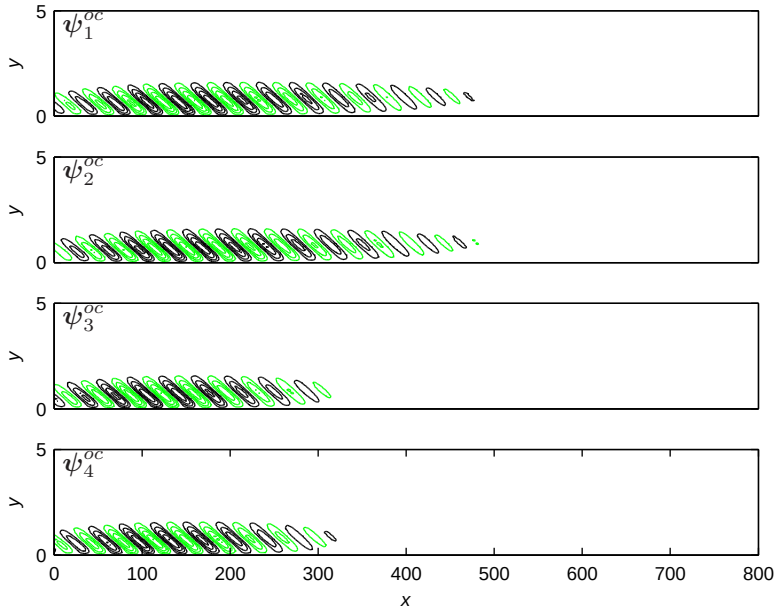

FIGURE 9. The streamwise velocity component of the adjoint balanced modes $\boldsymbol{\psi}_i^{oc}$.

an output $\mathcal{C}_1$ located downstream, the associated controllable and observable modes are spatially located in different part of the domain. The controllable subspace and the observable subspace are thus separated in the streamwise direction. This is a consequence of the convective nature of the instabilities arising in the Blasius flow where disturbances grow in amplitude as they are convected in the downstream direction. Essentially, this separation implies that the distribution of both the input and the output cannot be captured by an orthogonal projection onto the leading modes of only one subspace. Conversely, in a bi-orthogonal projection the adjoint balanced modes account for the output sensitivity and the direct balanced modes for the most energetic structures.

4. Model reduction

Since the disturbances are represented by an input and the objective consists of minimizing an output signal, capturing the input-output behavior of the system — described by the mapping $\mathcal{L}_o\mathcal{L}_c$ — is sufficient for the design of optimal and robust control schemes. The flow structures that are neither controllable nor observable are redundant for the input-output behavior. Moreover, the states that are nearly uncontrollable and nearly unobservable can be discarded since they have a very weak influence on the input-output behavior. A systematic approach of approximating the system given by (1) with a finite-dimensional

model, which preserves the main input-output behavior is called balanced truncation (Moore 1981). As we show below, balanced truncation amounts to a projection of state-space system (8) on the leading balanced modes.

We now return to the multi-input multi-output (MIMO) state-space system with input vector f and output vector y. The measurement noise acts on the output signal and affects the perturbation dynamics only in the closed loop-system and is hence not included in the analysis.

4.1. *Galerkin projection*

Assuming that the balanced modes form a complete basis in $\mathbb{X}$ any flow field $\boldsymbol{u}(\boldsymbol{x},t)$ can be approximated by

$$\boldsymbol{u}^r(\boldsymbol{x},t)=\sum_{j=1}^{r} q_j(t)\boldsymbol{\phi}_j^{oc}(\boldsymbol{x}), \tag{46}$$

where $q_j=\langle \boldsymbol{u},\boldsymbol{\psi}_j^{oc}\rangle_{\mathbb{X}}$ are the expansion coefficients. Inserting the above expansion into (8) and taking the inner product with the adjoint balanced modes $\boldsymbol{\psi}_i^{oc}$, the following r-dimensional state-space form is obtained,

$$\begin{aligned}
\dot{q} &= Aq+B_1\mathsf{w}+B_2\mathsf{u} && \text{(47a)}\\
\mathsf{v} &= C_1q+l\mathsf{u} && \text{(47b)}\\
\mathsf{z} &= C_2q+\alpha g\,. && \text{(47c)}
\end{aligned}$$

This system is referred to as the reduced-order model (ROM). Note that since the balanced modes satisfy the boundary conditions and are divergence-free the pressure gradient term vanishes after projection. The entries of the matrix A, column vector B_1 and row vector C_1 are

$$\begin{aligned}
A_{i,j} &= \langle \boldsymbol{\psi}_i^{oc},\mathcal{A}\boldsymbol{\phi}_j^{oc}\rangle_{\mathbb{X}} && \text{(48a)}\\
B_{1,j} &= \langle \boldsymbol{\psi}_j^{oc},\mathcal{B}_1\rangle_{\mathbb{X}} && \text{(48b)}\\
C_{1,j} &= \mathcal{C}_1\boldsymbol{\phi}_j^{oc} && \text{(48c)}
\end{aligned}$$

for $i,j=1,\ldots,r$. The components of the row vectors C_2 and B_2 are obtained in the same manner as for B_1 and C_1. The evolution operator associated with (47) is

$$T(t)=e^{At}=\sum_{j=0}^{\infty}\frac{(At)^j}{j!}. \tag{49}$$

Notice that the balanced modes are computed accounting for all the inputs (except the measurement noise) and outputs and the Galerkin projection (47) is performed only once. The projection of $\mathcal{A}$ on the balanced modes can be approximated by the finite-difference method using the time-stepper, *i.e.*

$$\mathcal{A}\boldsymbol{\phi}_i^{oc}\approx\frac{\mathcal{T}(\delta t)\boldsymbol{\phi}_i^{oc}-\boldsymbol{\phi}_i^{oc}}{\delta t}. \tag{50}$$

For the results presented, δt was chosen to be 10^{-4} after a convergence study.

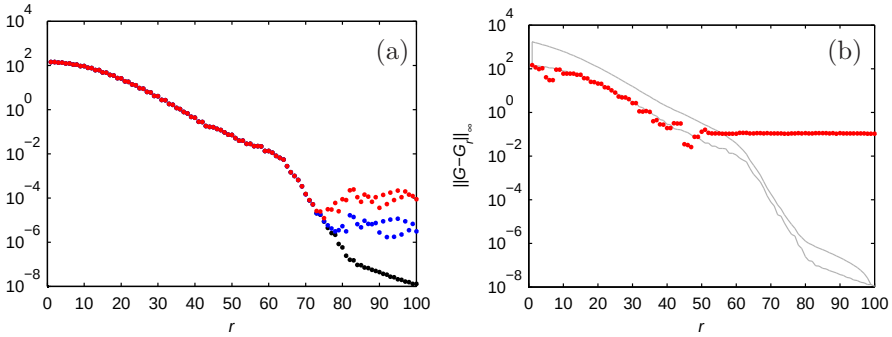

FIGURE 10. (a) The Hankel singular values (black symbols) are compared to the diagonal entries of the controllability and observability Gramians associated with the balanced reduced-order system. (b) The $\mathcal{H}_\infty$ model reduction error. The upper and lower theoretical bounds are depicted with gray lines and the actual model reduction error is show with red symbols.

To validate the properties of the snapshot-based balanced truncation, we construct the reduced-model (47) and compute its controllability and observability Gramians. The projected system is balanced if and only if its Gramians are diagonal and equal to the HSV. We found that the first 70×70 elements of both Gramians are diagonal. In figure 10 we compare the leading 100 diagonal elements with the HSV. The first 70 modes are observed to be bi-orthogonal to each other down to numerical accuracy. However, for higher modes as the numerical round-off errors increase, the bi-orthogonality condition is gradually lost and off-diagonal elements are observed in both Gramians. By increasing the numerical resolution and the number of snapshots it is possible to increase the number of balanced modes. However, — as noticed by (Moore 1981) — the ratio σ_1/σ_i serves as a condition number for $\boldsymbol{\phi}_1^{oc}$, and therefore the balanced modes corresponding to very small HSV can be ill-conditioned independently of the numerical approximations.

4.1.1. *Performance of reduced-order model*

In this section the input-output behavior of reduced-order model (47) is compared to the full Navier–Stokes system (8). We begin by comparing the impulse response from all inputs to all outputs. In figure (11) three signals $\mathcal{B}_1 \to \mathcal{C}_1$, $\mathcal{B}_1 \to \mathcal{C}_2$ and $\mathcal{B}_2 \to \mathcal{C}_1$ are shown with black lines. The response of $\mathcal{C}_2$ to forcing in $\mathcal{B}_2$ is zero, since disturbances traveling upstream are quickly damped. These impulse responses were obtained by using the time-stepper with $\sim 10^5$ degrees of freedom. The impulse responses of the reduced-order model (47) with $r = 50$ given by $\mathbf{y}(t) = Ce^{At}B$ are shown with red dashed lines. We observe that reduced-model registers the same signal as the full model from all inputs to all outputs. The wavepacket triggered by the impulse of $\mathcal{B}_1$ reaches

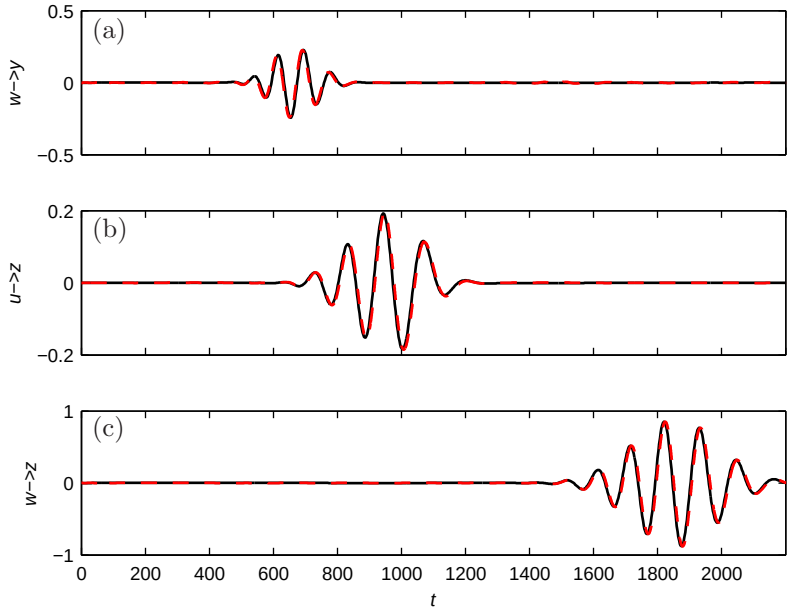

FIGURE 11. The impulse response from $\mathcal{B}_1 \rightarrow \mathcal{C}_2$ (a), $\mathcal{B}_2 \rightarrow \mathcal{C}_1$ (b) and $\mathcal{B}_1 c \rightarrow \mathcal{C}_1$ (c). The black solid line represents direct numerical simulations with 10^5 degrees of freedom and the red dashed line the balanced reduced-model with 50 degrees of freedom.

the first sensor $\mathcal{C}_2$ after 600 time units and the second sensor $\mathcal{C}_1$ after 1500 time units. The wavepacket triggered from the actuator reaches the second sensor after 600 time units.

The frequency response of the full system and of the reduced order model are compared next. The frequency response is related to the Laplace transform of the impulse response. To see this relation, we insert the complex forcing e^{st} in the formal solution (15) with zero initial condition and obtain

$$\mathbf{y}(t) = \int_0^\infty \mathcal{C}\mathcal{T}(t-\tau)\mathcal{B}Ie^{s\tau}\mathrm{d}\tau = \underbrace{\int_0^\infty \mathcal{C}\mathcal{T}(\tau)\mathcal{B}Ie^{s\tau}\mathrm{d}\tau}_{\mathcal{R}(s)} Ie^{st} = \mathcal{R}Ie^{st}. \qquad (51)$$

In the relation above, I is the unit vector of size 3. We can identify the transfer matrix $\mathcal{R}$ of size 2×3 as the Laplace transform of the impulse response from $\mathcal{B} \rightarrow \mathcal{C}$. Due to the linear nature of the equations an input e^{st} will generate an output with the same frequency but with a phase shift $\phi = \mathrm{Arg}\{\mathcal{R}\}$ and a different amplitude $|\mathcal{R}(s)|$. Since $\mathcal{R}(s)$ is a rectangular matrix, the amplitude is defined as

$$|\mathcal{R}(s)| = \sigma_1, \qquad (52)$$

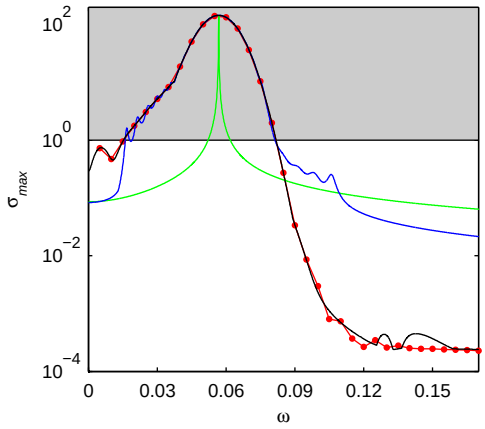

FIGURE 12. (a) The largest singular value of the transfer function $|\mathcal{R}(i\omega)|$ from all input to all outputs computed using the time-stepper is shown with red symbols. The largest response is for $\omega = 0.06$ with a peak value of 144.6. The frequencies in the grey domain are amplified. The frequency response of the reduced model with rank 2 (green), 50 (blue) and 80 (black).

where σ_1 is the largest singular value of $\mathcal{R}(s)$. The transfer function of the reduced-model is similarly defined as

$$R(s) = \int_0^\infty Ce^{A\tau}BIe^{s\tau}\mathrm{d}\tau. \tag{53}$$

The amplitudes of the transfer functions with $s = i\omega$, *i.e.* the frequency response, are displayed in figure 12 for reduced-order models of order $r = 2, 50$ and 80 and for the full model of order 10^5. Note that we do not have an explicit expression of $\mathcal{R}(i\omega)$. The frequency response is obtained from the numerical simulations by forcing from each input with constant frequency ω and extracting the time periodic signal from the output once the initial transients have died out.

From figure 12 we observe that the reduced-order model of order 2 captures the most important aspect of the input-output behavior, which is the response of the most dangerous frequency, *i.e.* the peak response of the full model. The model with 50 modes is able to estimate the gains of all the amplified frequencies, but fails to capture the damped low and high frequencies. Adding 30 additional modes results in a model that preserves the input-output behavior correctly for all frequencies. Note that there are no isolated eigenvalues in the spectrum of the spatially developing Blasius flow (Ehrenstein & Gallaire 2005; Åkervik *et al.* 2008) and therefore the frequency response is rather smooth with no peaks. Low-pass filters of this form cannot be represented with only a few degrees of freedom.

Finally, the model reduction error is computed and compared to the theoretical bounds given by the Hankel singular values. An attractive feature of balanced truncation is the existence of error bounds (note that this error bound is obtained *a priori* to Galerkin projection),

$$\sigma_{r+1} < \|\mathcal{R} - R\|_\infty \leq 2 \sum_{j=r+1}^{n} \sigma_j. \tag{54}$$

The infinity norm of the transfer function equals the peak value of the frequency response. Estimating the model reduction error (54) amounts to the calculation of the difference of the peak values of the reduced-order and the Navier–Stokes system. The error norm for the balanced truncation model is shown in figure 10b with red symbols. The peak value for the Navier–Stokes system is 144.60 which is gradually approached by the reduced-order model until it saturates at a peak value of 144.50. The error norm remains within or lower than the bounds given by the HSV for the first 50 modes. Note that an error which is lower than the theoretical bounds can be explained by the fact that the frequency response of the full system is also numerically approximated.

A thorough comparison between reduced order models obtained with POD modes and balanced modes can be found in Ilak & Rowley (2008) for the case of channel flow and in Bagheri *et al.* (2008) for the Ginzburg-Landau equation. The latter work also included global eigenmodes of the linearized operator in the comparison. For globally unstable flows it may be convenient to use the global eigenmodes as projection basis (Åkervik *et al.* 2007) for model reduction since the response to any input is dominated by the unstable eigenmodes asymptotically.

5. Feedback control

We will now develop a reduced-order feedback controller, which will have the same dimension as the reduced-order model (*e.g.* $r = 50$). The closed-loop behavior and the objective function z will be investigated and compared to the uncontrolled flat-plate boundary layer.

5.1. $\mathcal{H}_2$ — *framework*

The main idea of linear feedback control is shown in figure 13. As stated in the introduction our objective is to find a control signal $\mathsf{u}(t)$ such that in the presence of disturbances w, g the perturbation energy represented by the state variable $\boldsymbol{u}(\boldsymbol{x}, t)$ is minimized downstream at the location defined by the sensor $\mathcal{C}_1$. This is the $\mathcal{H}_2$ control problem.

In the previous section we showed that our reduced model (47) is able to capture the input-output behavior of the Navier–Stokes system (8). During the control design process we can assume that the reduced-model is the plant that we wish to control. Once we have determined the control law for this approximating model, we will apply it to the full Navier–Stokes system. We refer to (Anderson & Moore 1990; Zhou *et al.* 2002; Bagheri *et al.* 2008) for

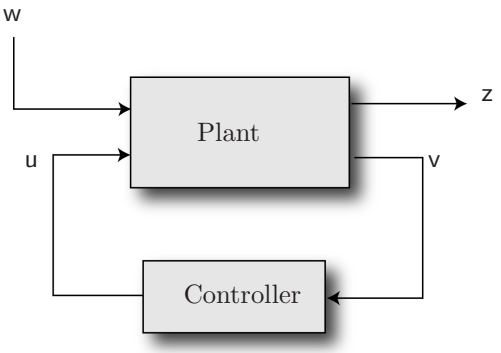

FIGURE 13. The closed-loop system. The plant represent the input-output system given by equation (8) subject to external disturbances w. The controller of order 50 forces the Navier–Stokes equations with the input signal u based on the noisy measurements v so that the effect of w on the output signal z is minimized.

further details on the $\mathcal{H}_2$ control algorithm, as we will only outline the main steps.

Following the notation introduced for the reduced-model (47), the objective function (7) becomes

$$\|\mathsf{z}\|_{L_2}^2 = \|C_1 q\|_{L_2}^2 + l^2 \|\mathsf{u}\|_{L_2}^2 = \int_0^t q^T C_1^T C_1 q + l^2 \mathsf{u}^T \mathsf{u} \mathrm{d}\tau. \tag{55}$$

The determination of the control signal is based only on the measurements from the sensor $\mathcal{C}_2$. However, for linear systems — due to the separation principle (Zhou *et al.* 2002) — the feedback control law can be determined assuming that the complete velocity field is known. The forcing needed to reproduce the flow only from wall measurements can be computed independently. Hence, the control design of the $\mathcal{H}_2$-control is performed in the following three steps:

(i) Compute the control feedback gain K by solving a Riccati equation (see Appendix D), so that the control signal is of feedback type, *i.e.*

$$\mathsf{u} = Kq. \tag{56}$$

This leads to a new system (compared to (47)),

$$\dot{q} = (A + B_2 K)q + B_1 \mathsf{w}, \tag{57a}$$

$$\mathsf{z} = C_1 q. \tag{57b}$$

It is expected that the above perturbated operator $A + B_2 K$ has dynamics that results in a smaller amplitude of the output signal z than for the unperturbated operator A in (47).

(ii) Compute the estimation feedback gain L by also solving a Riccati equation (see Appendix D), so that the observer

$$\dot{\hat{q}} = (A + LC_2)\hat{q} + L\mathsf{v} \tag{58a}$$

is asymptotically stable, *i.e.* $\|q - \hat{q}\| \to 0$ as $t \to \infty$. This implies that the estimated state $\hat{q}$ based on the measurements v approaches the true state q exponentially fast.

(iii) The closed-loop controller (figure 13) is finally obtained as

$$\dot{\hat{q}}(t) = (A + B_2K + LC_2)\hat{q}(t) - L\mathsf{v}, \tag{59a}$$

$$\mathsf{u} = K\hat{q}. \tag{59b}$$

Given the measurements signal v from the physical flow, the reduced-order controller provides an optimal control signal u proportional to the estimated flow $\hat{q}$.

To apply feedback control in the numerical simulations, an augmented state-space system with state $[\boldsymbol{u}, \hat{q}]^T$ is considered: its dynamics is given by (8) and (59), inputs $[\mathsf{w}, \mathsf{g}]$ and with the single output z:

$$\begin{pmatrix} \dot{\boldsymbol{u}} \\ \dot{\hat{q}} \end{pmatrix} = \begin{pmatrix} \mathcal{A} & \mathcal{B}_2K \\ -LC_2 & A + B_2K + LC_2 \end{pmatrix} \begin{pmatrix} \boldsymbol{u} \\ \hat{q} \end{pmatrix} + \begin{pmatrix} \mathcal{B}_1 & 0 \\ 0 & -L \end{pmatrix} \begin{pmatrix} \mathsf{w} \\ \mathsf{g} \end{pmatrix}, \tag{60a}$$

$$\mathsf{z} = \mathcal{C}_1\boldsymbol{u} \tag{60b}$$

where $\boldsymbol{u}$ is constrained to be divergence-free, $\nabla \cdot \boldsymbol{u} = 0$. This system is referred to as the closed-loop system. Note that the feedback gain K and estimation gain L have the dimension of the reduced model, resulting in a fast online controller.

The spatio-temporal evolution of the perturbations governed by the closed-loop system is obtained by solving the system (60) numerically using the time-stepper described in Appendix C and the small reduced-system in (59) simultaneously. The latter system is solved using a standard Crank-Nicholson scheme.

5.2. *Performance of closed-loop system*

We will now investigate the performance of the closed-loop system (60). In particular, the output z of the closed-loop — with optimal control signal u — and of the linearized Navier–Stokes equations without control are considered in the case of stochastic and harmonic forcing in w.

Three controllers are investigated: (i) cheap control/low noise contamination with $l = 0.1$ and $\alpha = 0.1$, (ii) expensive control/high noise contamination with $l = 10$ and $\alpha = 10$ and (iii) an intermediate case with $l = 2$ and $\alpha = 0.1$.

Note that the purpose of the measurement noise g is to account for uncertainties in the sensor measurements during the control design. When evaluating the closed-loop performance — solving the controlled Navier–Stokes equations — the system is only forced with w and not with g.

The performance of the control in case (i) is examined first. In figure 14 the input and output signals are shown. The gray region indicates the time when

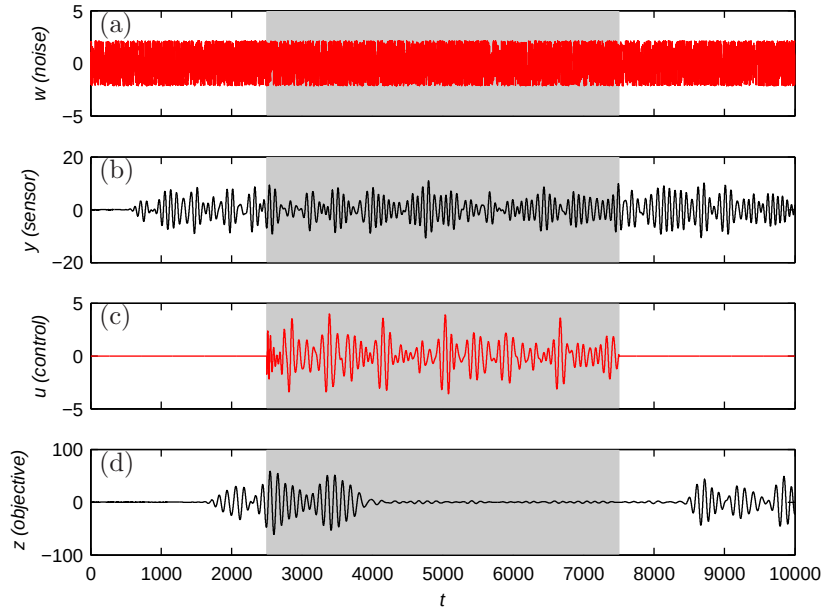

FIGURE 14. Input and output signals of the closed-loop system. The the random forcing w (a), measurements signal v (b), control signal u (c) and the objective function z (d) is shown. The cheap controller is active between $t \in [2500, 7500]$ marked with the gray area.

the control is active. As disturbance signal $\mathsf{w}(t)$ we choose white noise; the corresponding response of the sensor $\mathbf{y}(t)$ in figure 14b confirms the amplification and filtering of the signal as it traverses the unstable domain. The disturbances reach the second sensor (figure 14d) after about 1500 time units where they have been amplified by one order of magnitude. The control is activated at time $t = 2500$, the actuator immediately begins to force the system with a control signal (figure 14c) based on the output $\mathbf{y}$, and after a delay of another 1500 time units, the stabilizing effect of the control signal on the output z is clear. When the control is deactivated (at $t = 7500$) the disturbances start to grow again.

The wall-normal maximum of the rms-values of the streamwise velocity component in cases with and without control are shown in figure 15. The rms-value grows exponentially downstream in the uncontrolled case until the fringe region at $x = 800$. The rms of the controlled perturbation grows only until it reaches the actuator position where it immediately begins to decay. At the location of the objective function $\mathcal{C}_1$ ($x = 750$), the amplitude of the perturbations is one order of magnitude smaller than in the uncontrolled case for the cheapest controller.

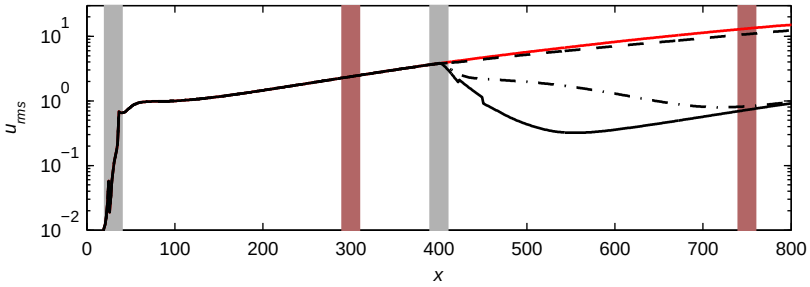

FIGURE 15. The rms-values of the uncontrolled system (red line), cheap controller (solid black), intermediate controller (dashed-dotted line) and expensive controller (dashed line). The gray bar represent the size (defined as 99% of the spatial support) and location of the two inputs, whereas the red bars correspond to the two outputs.

The rms values in the case of the expensive (case ii) and intermediate control (case iii) are shown with dashed and dashed-dotted lines respectively. The expensive control is very conservative as the measurement signals are highly corrupted and the control effort limited; it results only in a small damping of the disturbances. The intermediate controller (case iii) is more cautious in reducing the perturbation energy just downstream of the actuator when compared to the cheap controller. It is interesting to note, however, that at the location where the objective function is measured, the disturbance amplitude has decreased nearly as much as with the cheap controller, although the total perturbation energy is much larger over the entire domain.

In figure 16 the frequency response from $\mathsf{w} \rightarrow \mathsf{z}$ of the uncontrolled Navier–Stokes equations (8) (shown in red) is compared to that pertaining the three controllers under consideration. The black line corresponds to cheap control, green line to intermediate control and blue line to expensive control. The two former controllers suppress the most dangerous frequencies close to $\omega = 0.6$. Note that compared to the uncontrolled model, the highly damped frequencies $\omega > 0.11$ have larger gain in amplitudes. This behavior is often observed in closed-loop physical systems and is related to the "water-bed" effect, *i.e.* when certain frequencies are suppressed, the response at other frequencies is amplified.

6. Conclusions

Model-based feedback control of the instabilities arising in a spatially inhomogeneous boundary layer flow is studied. To build a reduced-order model of the problem, where the application of standard tools from control theory become computationally feasible also for fluid flow systems, the main features of the flow

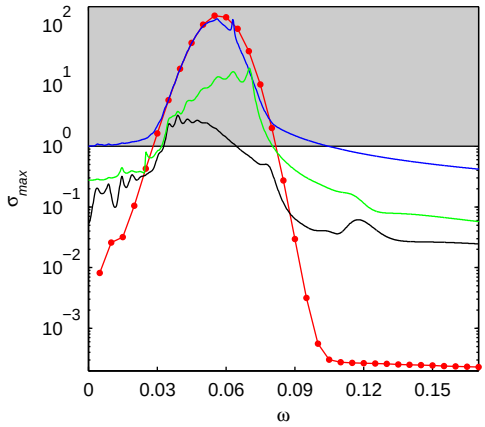

FIGURE 16. Comparison of the frequency response of open-loop (red) and closed loop system. The cheap, intermediate and expensive controllers are represented by the black, green and blue lines respectively.

behavior are investigated in an input-output framework. The observable, controllable and balanced modes of the system have been identified. The location and structure of these modes reflect the location of sensors/actuators and the perturbation dynamics, i.e the observable modes are located upstream, where the sensitivity to initial conditions is the largest. The controllable modes, conversely, are located downstream, where the response to the forcing is largest. The analysis presented here can be closely related to stability analysis using global modes and optimal disturbances, except that inputs and outputs are taken into account. The quantity one wishes to optimize for is now defined by a sensor output, while perturbations are introduced by the inputs considered in the model. Furthermore, in view of the control application, the formulation of the control objective function as an output is particularly attractive in this input-output setting, since this behavior is well-captured by the reduced-order model.

Model reduction is achieved by projecting the governing equations on the leading balanced modes of the system. We show that the input-output behavior of the flat-plate boundary layer can be captured accurately with a reduced-order model based on these modes. Finally, the model was used to apply feedback control based on measurements from one upstream sensor and an actuator further downstream. The perturbations growth could be reduced efficiently using the $\mathcal{H}_2$ optimal feedback controller.

It is also important to note that the approach followed here requires only the use of a time-stepper, a numerical code solving the Navier–Stokes equations, and avoids the use of the large matrices defining the operators governing the input-output behavior. In addition, the present formulation accounts naturally

for localized sensors and actuators and therefore, it can be directly applied to different flow configurations.

Acknowledgements

The authors like to thank Espen Åkervik, Milos Ilak and Antonios Monokrousos for fruitful discussions. This work partially was sponsored by the Air Force Office of Scientific Research, through the European Office EOARD, under grant/contract number FA8655-07-1-3053.

Appendix A. Derivation of adjoint operators

A.1. *The adjoint operator $\mathcal{T}^*$, $\mathcal{B}^*$, $\mathcal{C}^*$ and $\mathcal{A}^*$*

For a bounded linear operator between two Hilbert spaces, $\mathcal{L} : \mathbb{X}_1 \rightarrow \mathbb{X}_2$, the adjoint operator $\mathcal{L}^*$ satisfies

$$\langle \mathcal{L}\boldsymbol{q}, \boldsymbol{p} \rangle_{\mathbb{X}_2} = \langle \boldsymbol{q}, \mathcal{L}^*\boldsymbol{p} \rangle_{\mathbb{X}_1} \quad \text{for all} \quad \boldsymbol{q} \in \mathbb{X}_1, \boldsymbol{p} \in \mathbb{X}_2. \tag{61}$$

We begin with deriving the adjoint operator of $\mathcal{B}$, using the identity

$$\langle \mathcal{B}\mathbf{f}, \boldsymbol{u} \rangle_{\mathbb{X}} = \langle \mathbf{f}, \mathcal{B}^*\boldsymbol{u} \rangle_{\mathbb{U}}. \tag{62}$$

The left-hand side is equivalent to

$$\int_\Omega (\mathcal{B}\mathbf{f})^T \boldsymbol{u} \mathrm{d}x\mathrm{d}y \quad = \quad \int_\Omega \mathbf{f}^T \mathcal{B}^T \boldsymbol{u} \mathrm{d}x\mathrm{d}y = \langle \mathbf{f}, \int_\Omega B^T \boldsymbol{u} \mathrm{d}x\mathrm{d}y \rangle_{\mathbb{U}}\,; \tag{63}$$

using (62) we identify

$$\mathcal{B}^*\boldsymbol{u} = \int_\Omega \mathcal{B}^T \boldsymbol{u} \mathrm{d}x\mathrm{d}y. \tag{64}$$

The adjoint of the output operator can be derived in an analogous manner by using the identity

$$\langle \mathcal{C}\boldsymbol{u}, \mathbf{y} \rangle_{\mathbb{Y}} = \langle \boldsymbol{u}, \mathcal{C}^*\mathbf{y} \rangle_{\mathbb{X}}. \tag{65}$$

The left-hand side can be written

$$\langle \mathcal{C}\boldsymbol{u}, \mathbf{y} \rangle_{\mathbb{Y}} \quad = \quad (\mathcal{C}\boldsymbol{u})^T \mathbf{y} = \int_\Omega (\hat{\mathcal{C}}\boldsymbol{u})^T \mathbf{y} = \int_\Omega \boldsymbol{u}^T \hat{\mathcal{C}}^T \mathbf{y} = \langle \boldsymbol{u}, \hat{\mathcal{C}}^T \mathbf{y} \rangle_{\mathbb{X}} \tag{66}$$

where $\hat{\mathcal{C}}$ is the integrand in (13). We can now identify the adjoint output operator as

$$\mathcal{C}^*\mathbf{y} = \hat{\mathcal{C}}^T \mathbf{y} \tag{67}$$

The evolution operator $\mathcal{T}$ was defined in (14). The adjoint of $\mathcal{T}$ satisfies

$$\langle \mathcal{T}\boldsymbol{u}, \boldsymbol{p} \rangle_{\mathbb{X}} = \langle \boldsymbol{u}, \mathcal{T}^*\boldsymbol{p} \rangle_{\mathbb{X}}. \tag{68}$$

We begin with taking the inner product of $\boldsymbol{p}$ and σ with the unforced ($\boldsymbol{f} = 0$) Navier–Stokes equations 1a and 1b, respectively. By integrating over

the time domain and applying integration by parts we obtain

$$\begin{aligned} 0 &= \int_0^t \int_\Omega \left(\boldsymbol{p}^T [\frac{\partial \boldsymbol{u}}{\partial t} - \mathcal{A}\boldsymbol{u} - \nabla p] + \sigma(\nabla \cdot \boldsymbol{u}) \right) \mathrm{d}x\mathrm{d}y\mathrm{d}t \\ &= \underbrace{\int_0^t \int_\Omega \left(-\boldsymbol{u}^T (\frac{\partial \boldsymbol{p}}{\partial t} + \mathcal{A}^* \boldsymbol{p} + \nabla\sigma) - p(\nabla \cdot \boldsymbol{p}) \right) \mathrm{d}x\mathrm{d}y\mathrm{d}t}_{1} + \underbrace{\int_0^t [B.C.]_\Omega \mathrm{d}t}_{2} \\ &\quad + \underbrace{\int_\Omega \boldsymbol{u}(t)^T \boldsymbol{p}(t) \mathrm{d}x\mathrm{d}y - \int_\Omega \boldsymbol{u}(0)^T \boldsymbol{p}(0) \mathrm{d}x\mathrm{d}y}_{3} \end{aligned} \tag{69}$$

By requiring the first two terms to be zero we obtain the adjoint Navier–Stokes equations with boundary conditions. They will be considered after the boundary terms in time denoted by 3 in (69). We thus require that

$$\int_\Omega \boldsymbol{u}(t)^T \boldsymbol{p}(t) \mathrm{d}x\mathrm{d}y = \int_\Omega \boldsymbol{u}(0)^T \boldsymbol{p}(0) \mathrm{d}x\mathrm{d}y. \tag{70}$$

The left hand side can be rewritten as

$$\begin{aligned} &\int_\Omega (\mathcal{T}(t)\boldsymbol{u}(0))^T \boldsymbol{p}(t) \mathrm{d}x\mathrm{d}y = \langle \mathcal{T}(t)\boldsymbol{u}(0), \boldsymbol{p}(t) \rangle_{\mathbb{X}} \\ &= \langle \boldsymbol{u}(0), \mathcal{T}^* \boldsymbol{p}(t) \rangle_{\mathbb{X}} = \int_\Omega \boldsymbol{u}(0)^T \mathcal{T}^* \boldsymbol{p}(t)\,, \end{aligned}$$

where we can identify the action of the adjoint evolution operator

$$\mathcal{T}^* \boldsymbol{p}(t) = \boldsymbol{p}(0). \tag{71}$$

Now we proceed with deriving the adjoint equations associated with $\mathcal{T}^*$. The spatial boundary terms given by the second term in (69) are

$$\begin{aligned} \int_0^t [B.C.]_\Omega \mathrm{d}t &= \int_0^T \left[\sigma u + u^* p + U \boldsymbol{u}^T \boldsymbol{p} + \boldsymbol{p}^T \frac{\partial \boldsymbol{u}}{\partial x} - \boldsymbol{u}^T \frac{\partial \boldsymbol{p}}{\partial x} \right]_0^{L_x} \\ &\quad + \left[\sigma v + v^* p + V \boldsymbol{u}^T \boldsymbol{p} + \boldsymbol{p}^T \frac{\partial \boldsymbol{u}}{\partial y} - \boldsymbol{u}^T \frac{\partial \boldsymbol{p}}{\partial y} \right]_0^{L_y} \mathrm{d}t = 0. \end{aligned}$$

If boundary conditions (3) on $\boldsymbol{u}$ are used and if we demand the that $\boldsymbol{p} = [u^*, v^*]$, σ^*, and p satisfies

$$[\sigma, p]_{x=0} = [\sigma, p]_{x=L_x}, \tag{72a}$$

$$[u^*, v^*]_{x=0} = [u^*, v^*]_{x=L_x}, \tag{72b}$$

$$[u^*, v^*]_{y=0} = [u^*, v^*]_{y=L_y} = 0. \tag{72c}$$

we observe that the boundary terms vanish.

Finally the first term in (69) define the adjoint Navier–Stokes equations if we demand that $\boldsymbol{p}$ satisfies the

$$-\dot{\boldsymbol{p}} = \mathcal{A}^* \boldsymbol{p} + \nabla\sigma \tag{73a}$$

$$0 = \nabla \cdot \boldsymbol{p} \tag{73b}$$

with $\mathcal{A}^*$ as given by equation (22). The above equations together with boundary conditions (72b) and (72c) determine the behavior of adjoint flow field $\boldsymbol{p}$.

A.2. *The adjoint operators $\mathcal{L}_c^*$ and $\mathcal{L}_o^*$*

The adjoint controllability operator is derived using the identity

$$\langle \mathcal{L}_c \mathbf{f}, \boldsymbol{u}_0 \rangle_{\mathbb{X}} = \langle \mathbf{f}, \mathcal{L}_c^* \boldsymbol{u}_0 \rangle_{L_2(-\infty,0)}. \tag{74}$$

We expand the left hand side,

$$\begin{aligned}\langle \mathcal{L}_c \mathbf{f}, \boldsymbol{u}_0 \rangle_{\mathbb{X}} &= \int_\Omega \int_{-\infty}^0 (\mathcal{T}(-t)\mathcal{B}\mathbf{f}(t))^T \boldsymbol{u}_0 \mathrm{d}t\mathrm{d}x\mathrm{d}y \\ &= \int_{-\infty}^0 \mathbf{f}^T(t)(\mathcal{B}^*\mathcal{T}^*(-t))\boldsymbol{u}_0 \mathrm{d}t \\ &= \langle \mathbf{f}(t), \mathcal{B}^*\mathcal{T}^*(-t)\boldsymbol{u}_0 \rangle_{L_2(-\infty,0)}.\end{aligned}$$

In the first equality the definitions of $\mathcal{B}^*$ and $\mathcal{T}^*$ from expressions (64) and (68) were used. We can now identify

$$\mathcal{L}_c^*(-t)\boldsymbol{u}_0 = \mathcal{B}^*\mathcal{T}^*(-t)\boldsymbol{u}_0\,. \tag{75}$$

In a similar fashion the adjoint observability operator is defined by

$$\langle \mathcal{L}_o \boldsymbol{u}, \mathbf{y} \rangle_{L_2(0,\infty)} = \langle \boldsymbol{u}, \mathcal{L}_o^* \mathbf{y} \rangle_{\mathbb{X}}. \tag{76}$$

Expanding the left-hand side results in

$$\begin{aligned}\langle \mathcal{L}_o \boldsymbol{u}, \mathbf{y} \rangle_{L_2(0,\infty)} &= \int_0^\infty (\mathcal{C}\mathcal{T}(t)\boldsymbol{u}(t))^T \mathbf{y} \mathrm{d}t \\ &= \int_0^\infty \int_\Omega (\hat{\mathcal{C}}\mathcal{T}(t)\boldsymbol{u}(t))^T \mathbf{y} \mathrm{d}x\mathrm{d}y\mathrm{d}t \\ &= \int_0^\infty \int_\Omega \boldsymbol{u}^T (\mathcal{T}^*(t)\mathcal{C}^*\mathbf{y}(t))^T \mathrm{d}x\mathrm{d}y\mathrm{d}t \\ &= \langle \boldsymbol{u}, \int_0^\infty \mathcal{T}^*\mathcal{C}^*\mathbf{y}\mathrm{d}t \rangle_{\mathbb{X}}\,,\end{aligned}$$

where $\hat{\mathcal{C}}$ is the integrand in (13). We can identify the adjoint operator as

$$\mathcal{L}_o^*(t)\mathbf{y}(t) = \int_0^\infty \mathcal{T}^*(t)\mathcal{C}^*\mathbf{y}(t)\ \mathrm{d}t. \tag{77}$$

Appendix B. The snapshot method

We will show how to approximate the eigenvalue problems (35),(31) and (45) in order to compute the observable, controllable and balanced modes.

B.1. *Approximate Gramians*

We begin with considering the eigenvalue problem,

$$\mathcal{P}\boldsymbol{\phi}_i^c = \lambda_i^c \boldsymbol{\phi}_i^c. \tag{78}$$

The first step is to rewrite the controllability Gramian $\mathcal{P}$ as a covariance operator. To achieve this we define the 2×1 vector $\bar{\boldsymbol{u}}$ containing the impulse response of the inputs, *i.e.*

$$\bar{\boldsymbol{u}} = [\boldsymbol{u}_1, \boldsymbol{u}_2] = [\mathcal{T}\mathcal{B}_1, \mathcal{T}\mathcal{B}_2]. \tag{79}$$

Furthermore, we use equation (64) and (68) to rewrite the action of $\mathcal{B}^*\mathcal{T}^*$ on $\boldsymbol{\phi}_i^c$ as

$$\mathcal{B}^*\mathcal{T}^*\boldsymbol{\phi}_i^c = \int_\Omega (\mathcal{T}\mathcal{B})^T \boldsymbol{\phi}_i^c \mathrm{d}x\mathrm{d}y = \int_\Omega \bar{\boldsymbol{u}}^T \boldsymbol{\phi}_i^c \mathrm{d}x\mathrm{d}y. \tag{80}$$

The controllability Gramian can now be written as a covariance of the impulse response $\bar{\boldsymbol{u}}$,

$$\mathcal{P} = \int_0^\infty \mathcal{T}(t)\mathcal{B}\mathcal{B}^*\mathcal{T}^*(t)\mathrm{d}t = \int_0^\infty \bar{\boldsymbol{u}} \int_\Omega \bar{\boldsymbol{u}}^T \, \mathrm{d}x\mathrm{d}y\mathrm{d}t. \tag{81}$$

We discretize $\mathcal{P}$ in space using n grid/collocation points and in time using m grid-points. If the variable $\bar{\boldsymbol{u}}(\boldsymbol{x}, t)$ evaluated at the grid-points (*i.e.* a $n \times 2m$ matrix) is multiplied with the square root of the quadrature coefficients δ_{t_j} and $\delta_{\boldsymbol{x}_j}$, of time and space integrals respectively, we get

$$X = \begin{bmatrix} \boldsymbol{u}_1(\boldsymbol{x}_1, t_1)\sqrt{\delta_{t_1}\delta_{\boldsymbol{x}_1}} & \dots & \boldsymbol{u}_1(\boldsymbol{x}_1, t_m)\sqrt{\delta_{t_n}\delta_{\boldsymbol{x}_1}} & \dots & \boldsymbol{u}_2(\boldsymbol{x}_1, t_m)\sqrt{\delta_{t_n}\delta_{\boldsymbol{x}_1}} \\ \vdots & & \vdots & & \vdots \\ \boldsymbol{u}_1(\boldsymbol{x}_n, t_1)\sqrt{\delta_{t_1}\delta_{\boldsymbol{x}_n}} & \dots & \boldsymbol{u}_1(\boldsymbol{x}_n, t_m)\sqrt{\delta_{t_n}\delta_{\boldsymbol{x}_n}} & \dots & \boldsymbol{u}_2(\boldsymbol{x}_n, t_m)\sqrt{\delta_{t_n}\delta_{\boldsymbol{x}_n}} \end{bmatrix} \tag{82}$$

where each column of X is referred to as a snapshot. Note that the quadrature weights δ_{t_j} and $\delta_{\boldsymbol{x}_j}$ depend on the chosen quadrature rule. For instance in our case, $\delta_{\boldsymbol{x}_j}$ consist of the Chebyshev integral weight functions (Hanifi *et al.* 1996) in the wall-normal direction and a trapezoidal rule in the streamwise direction.

The expression (78) can now be approximated with $XX^T\hat{\boldsymbol{\phi}^c}_i$, which results in following $n \times n$ eigenvalue problem

$$XX^T\hat{\boldsymbol{\phi}^c}_i = \lambda_i^c \hat{\boldsymbol{\phi}^c}_i, \qquad i = 1, \dots, n \tag{83}$$

where $\hat{\boldsymbol{\phi}}_i^c$ is a column vector with $\boldsymbol{\phi}_i^c$ evaluated at the spatial grid points.

It is prohibitively expensive to diagonalize the matrix XX^T when $n \geq 10^5$. In the method of snapshots (Sirovich 1987), the modes $\hat{\boldsymbol{\phi}^c}_i$ can be approximated by diagonalizing the $2m \times 2m$ matrix X^TX instead. This is efficient when the product of the number of snapshots and the number of inputs is much smaller than the number of grid-points.

In the method of snapshots the modes, $\hat{\boldsymbol{\phi}^c}_i$ are expanded in snapshots, *i.e.* the columns of matrix X. The expansion can be formulated in matrix form as

$$\boldsymbol{\phi}_i^c = X\boldsymbol{a}_i \qquad\qquad i = 1, \dots, 2m, \tag{84}$$

with the column vector $\boldsymbol{a}_i$ containing the expansion coefficients.

The above expansion is inserted to the large eigenvalue problem (83) which results in the $2m \times 2m$ eigenvalue problem

$$X^T X \boldsymbol{a}_i = \lambda_i^c \boldsymbol{a}_i \qquad i = 1, \ldots, 2m. \tag{85}$$

The eigenvalues λ_i^c are the same as the original eigenvalue problem and the controllable modes are recovered from equation (84). The orthonormal set of controllable modes are given by

$$\hat{\boldsymbol{\phi}^c}_i = \frac{1}{\sqrt{\lambda_i}} X \boldsymbol{a}_i, \qquad \hat{\boldsymbol{\phi}^c}_i^T \hat{\boldsymbol{\phi}^c}_j = \delta_{ij}. \tag{86}$$

There are some important computational issues which should be commented at this point: (i) The Gramian 29 is defined as an infinite integral, which means that in order for the *approximate* Gramian XX^T to be a sufficiently good approximation, we should take snapshots for a long time. There are no restrictions on how to distribute the snapshots in time and it is prudent to store many snapshots when the flow energy is large. (ii) Due to numerical round–off errors, often not all modes are orthogonal. In our case with $2m = 3200$, the first 150 modes were orthogonal down to numerical accuracy (i.e $(\boldsymbol{\phi}_i^c)^T \boldsymbol{\phi}_i^c \approx 10^{-15}$), whereas for higher modes the orthogonality condition is gradually lost due to rounding errors. The ratio $\mu_i = \lambda_1/\lambda_i$ can be used as a condition number of the corresponding mode $\boldsymbol{\phi}_i^c$. Very large values of μ_c indicate poor orthogonality due to numerical inaccuracy.

The observable modes are computed in a similar manner, but now the snapshots are taken from impulse responses of the adjoint equations for each output, *i.e.* $\bar{\boldsymbol{p}} = [\boldsymbol{p}_1, \boldsymbol{p}_2]^T = [\mathcal{T}^* \hat{\mathcal{C}}_1^T, \mathcal{T}^* \hat{\mathcal{C}}_2^T]^T$ with $\hat{\mathcal{C}}$ as the integrand in (13). The approximate observability Gramian is

$$\mathcal{Q} = \int_0^\infty \mathcal{T}^* \mathcal{C}^* \mathcal{C} \mathcal{T} \mathrm{d}t = \int_0^\infty \bar{\boldsymbol{p}} \int_\Omega \bar{\boldsymbol{p}}^T \mathrm{d}x \mathrm{d}y \mathrm{d}t \approx Y Y^T, \tag{87}$$

where Y is the $n \times 2m$ matrix

$$Y = \begin{bmatrix} \boldsymbol{p}_1(\boldsymbol{x}_1, t_1)\sqrt{\delta_{t_1}\delta_{\boldsymbol{x}_1}} & \ldots & \boldsymbol{p}_1(\boldsymbol{x}_1, t_1)\sqrt{\delta_{t_1}\delta_{\boldsymbol{x}_n}} & \ldots & \boldsymbol{p}_2(x_1, t_m)\sqrt{\delta_{t_n}\delta_{\boldsymbol{x}_1}} \\ \vdots & & \vdots & & \vdots \\ \boldsymbol{p}_1(\boldsymbol{x}_n, t_1)\sqrt{\delta_{t_1}\delta_{\boldsymbol{x}_n}} & \ldots & \boldsymbol{p}_1(\boldsymbol{x}_n, t_1)\sqrt{\delta_{t_1}\delta_{\boldsymbol{x}_n}} & \ldots & \boldsymbol{p}_2(x_n, t_m)\sqrt{\delta_{t_n}\delta_{\boldsymbol{x}_n}} \end{bmatrix}. \tag{88}$$

The observable modes are computed in an analogous manner as the controllable modes with Y replacing X in equations (84)–(86).

B.2. *Snapshot-based balanced truncation*

To obtain the balanced modes, we must diagonalize the matrix $\mathcal{PQ}$, which can approximated using the matrices X and Y, i,e.

$$\mathcal{PQ}\boldsymbol{\phi}_i^{oc} \approx XX^T YY^T \hat{\boldsymbol{\phi}^{oc}}_i = \sigma_i^2 \hat{\boldsymbol{\phi}^{oc}}_i \tag{89}$$

We expand the balanced modes as linear combinations of the columns of X, with $\boldsymbol{a}_i = [a_1, \ldots, a_m]^T$ as the expansion coefficients. Inserting this expansion in (89), we get

$$0 = XX^TYY^TX\boldsymbol{a}_i - X\boldsymbol{a}_i\sigma_i^2 = X(X^TYY^TX\boldsymbol{a}_i - \boldsymbol{a}_i\sigma_i^2), \tag{90}$$

To solve the above problem we can equivalently diagonalize X^TYY^TX or form the singular value decomposition (SVD) of Y^TX. The latter decomposition is preferred since it is numerically more stable, *i.e.*

$$Y^TX\boldsymbol{b}_i = \sigma_i\boldsymbol{a}_i, \qquad i = 1, \ldots, 2m \tag{91}$$

The normalized balanced modes and the associated adjoint balanced modes are recovered from

$$\hat{\boldsymbol{\phi}^{oc}}_i = \frac{1}{\sqrt{\sigma_i}}X\boldsymbol{b}_i, \qquad \hat{\boldsymbol{\psi}^{oc}}_i = \frac{1}{\sqrt{\sigma_i}}Y\boldsymbol{a}_i \tag{92}$$

where $\hat{\boldsymbol{\psi}^{oc}}_i^T \hat{\boldsymbol{\phi}^{oc}}_j = \delta_{ji}$.

The method can be summarized in three steps; (i) compute the impulse response of each input, collect snapshots of the response and construct X (82) (ii) compute the adjoint impulse response of each output, collect snapshots of the response and construct Y (88) (iii) form the matrix Y^TX, compute its SVD and recover the balanced modes from (92). See Rowley (2005) for further details on the method.

Appendix C. Time-stepper

The time-stepper used in this work for both the forward and adjoint equations is a spectral code described in detail in Chevalier *et al.* (2007*b*).

If $f(x, y, t)$ is a velocity component then the discrete approximation is the Chebyshev-Fourier series

$$\mathsf{f}(t) = \sum_{l=0}^{n_y} T_l(y) \sum_{m=-n_x/2}^{n_x/2} e^{i\alpha_m x}\hat{u}_{lm} + c.c. \tag{93}$$

where T_l is the lth Chebyshev polynomial, $\alpha_l = 2m\pi L_x$ and $n_x = 768$ and $n_y = 101$ the number of collocation points in each direction. The coefficients $\hat{u}_{lm}$ are complex functions. The associated collocation grid is defined by $y_l = \cos(\pi l/n_y)$ and $x_m = m\alpha/n_x$. The discretized system of equations is projected onto a divergence-free space by transforming to $v-\eta$ formulation and integrated in time using a third-order semi-implicit scheme.

To retain periodic boundary conditions, which is necessary for the Fourier discretization, a fringe region is added at the end of the physical domain where a forcing is applied so that the flow smoothly changes from the outflow velocity of the physical domain to the desired inflow velocity. For the linearized equation the desired inflow condition is zero, so the fringe forcing is of the form $F = \lambda(x)\boldsymbol{u}$, where

$$\lambda(x) = -\lambda_{max}\left[S\left(\frac{x - x_{start}}{\Delta_{rise}}\right) - S\left(\frac{x - x_{end}}{\Delta_{fall}}\right)\right]. \tag{94}$$

Here $\lambda_{\max}$ is the maximum strength of the damping, x_{start} to x_{end} the spatial extent of the region where the damping function is non-zero and Δ_{rise} and Δ_{fall} the rise and fall distance of the damping function. The smooth "step" function $S(x)$ rises from zero for negative x to one for $x \geq 1$. We have used the following form for S, which has the advantage of having continuous derivatives of all orders,

$$S(x) = \begin{cases} 0\,, & x \leq 0\,, \\ 1/\left(1 + e^{(1/(x-1)+1/x)}\right), & 0 < x < 1\,, \\ 1\,, & x \geq 1\,. \end{cases} \tag{95}$$

Appendix D. Riccati equations

We briefly outline the full-information control and estimation problems and their solutions. The reader is directed to Anderson & Moore (1990); Lewis & Syrmos (1995); Bagheri *et al.* (2008) for derivations of the solutions.

The first step in the design of an $\mathcal{H}_2$-compensator involves the solution of an optimal control state-feedback problem. The full-information problem is to find a control $\mathsf{u}(t)$ as a linear function of the flow state $q(t)$ that minimizes the deterministic cost functional

$$J = \frac{1}{2}\int_0^\infty q^T C_1^T C_1 q + l^2 \mathsf{u}^T \mathsf{u}\; dt, \tag{96}$$

while satisfying the initial value problem

$$\dot{q} = Aq + B_2\mathsf{u}, \qquad\qquad q(t=0) = q_0. \tag{97}$$

The optimal control signal is given by

$$\mathsf{u}(t) = \underbrace{-\frac{1}{l^2}B_2^T X}_{K}\, q(t), \tag{98}$$

where X is a solution of the Riccati equation

$$0 = A^T X + XA - \frac{1}{l^2} X B_2 B_2^T X + C_1^T C_1 \tag{99}$$

The solution to this equation provides the optimal steady feedback gain via the relation (98).

The second step in the design of an $\mathcal{H}_2$-compensator involves the minimization of the estimation error $q_e = q - \hat{q}$ given by the estimator

$$\dot{q}_e = Aq_e + B_1 w + L(\mathsf{v} - \hat{\mathsf{v}}), \qquad \hat{q}(t=0) = 0 \tag{100}$$

$$\hat{\mathsf{v}} = C_1\hat{q} \tag{101}$$

$$\mathsf{v} = C_1 q + g\,, \tag{102}$$

where w and g are temporal white noise signals. The solution is the feedback gain L that minimizes the objective functional

$$J = \int_0^T q_e^T q_e. \tag{103}$$

The functional (103) can be minimized if L is chosen as

$$L = -\frac{1}{\alpha^2} P C_2^T. \tag{104}$$

where P is a solution of the Riccati equation,

$$0 = AP + PA^T - \frac{1}{\alpha^2} P C_2^T C_2 P + B_1 B_1^T. \tag{105}$$

References

Ahuja, S., Rowley, C. W., Kevrekidis, I. G. & Wei, M. 2007 Low-dimensional models for control of leading-edge vortices: Equilibria and linearized models. *AIAA Paper 2007-709, 45th AIAA Aerospace Sciences Meeting and Exhibit* .

Åkervik, E., Ehrenstein, U., Gallaire, F. & Henningson, D. 2008 Global two-dimensional stability measures of the flat plate boundary-layer flow. *Eur. J. Mech. B/Fluids* In press.

Åkervik, E., Hœpffner, J., Ehrenstein, U. & Henningson, D. S. 2007 Optimal growth, model reduction and control in a separated boundary-layer flow using global eigenmodes. *J. Fluid. Mech.* **579**, 305–314.

Anderson, B. & Moore, J. 1990 *Optimal control: Linear Quadratic Methods*. New York: Prentice Hall.

Bagheri, S., Hœpffner, J., Schmid, P. & Henningson, D. 2008 Input-output analysis and control design applied to a linear model of spatially developing flows. *Appl. Mech. Rev.* In press.

Barkley, D., Gomes, M. G. & Henderson, R. D. 2002 Three-dimensional instability in flow over a backward-facing step. *J. Fluid Mech.* **473**, 167–190.

Bewley, T., Temam, R. & Ziane, M. 2000 A general framework for robust control in fluid mechanics. *Physica D: Nonlinear Phenomena* **138**, 360–392.

Butler, K. & Farrell, B. F. 1992 Three-dimensional optimal perturbations in viscous shear flow. *Phys. Fluids A* **4**, 1637–1650.

Chevalier, M., Hœpffner, J., Åkervik, E. & Henningson, D. S. 2007*a* Linear feedback control and estimation applied to instabilities in spatially developing boundary layers. *J. Fluid Mech.* **588**, 163–187.

Chevalier, M., Schlatter, P., Lundbladh, A. & D.S., H. 2007*b* A pseudo spectral solver for incompressible boundary layer flows. *Technical Report, Trita-Mek* **7**.

Chomaz, J. M. 2005 Global instabilities in spatially developing flows: Non-normality and nonlinearity. *Ann. Rev. Fluid Mech.* **37**, 357–392.

Chorin, A. & Marsden, J. 1990 *A Mathematical introduction to fluid mechanics*. New York: Springer Verlag.

Curtain, R. & Zwart, H. 1995 *An introduction to infinite-dimensional linear systems theory*. New York: Springer Verlag.

Dullerud, E. & Paganini, F. 1999 *A course in robust control theory. A convex approach*. New York: Springer Verlag.

Ehrenstein, U. & Gallaire, F. 2005 On two-dimensional temporal modes in spatially evolving open flows: The flat-plate boundary layer. *J. Fluid Mech.* **536**, 209–218.

Gillies, E. A. 1998 Low-dimensional control of the circular cylinder wake. *J. Fluid Mech.* **371**, 157–178.

Hanifi, A., Schmid, P. & Henningson, D. 1996 Transient growth in compressible boundary layer flow. *Phys. Fluids* **8** (3), 826–837.

Högberg, M., Bewley, T. R. & Henningson, D. S. 2003 Linear feedback control and estimation of transition in plane channel flow. *J. Fluid Mech.* **481**, 149–175.

Ilak, M. & Rowley, C. W. 2008 Modeling of transitional channel flow using balanced proper orthogonal decomposition. *Phys. Fluids* **20**, 034103.

Kailath, T. 1980 *Linear Systems*. Englewood Cliffs: Prentice-Hall.

Kim, J. & Bewley, T. R. 2007 A linear systems approach to flow control. *Annu. Rev. Fluid Mech.* **39**, 383–417.

Lauga, E. & Bewley, T. R. 2003 The decay of stabilizability with reynolds number in a linear model of spatially developing flows. *Proc. R. Soc. Lond. A.* **459**, 2077–2095.

Lewis, F. L. & Syrmos, L. V. 1995 *Optimal Control*. New York: John Wiley & Sons.

Moore, B. 1981 Principal component analysis in linear systems: Controllability, observability, and model reduction. *Automatic Control, IEEE Transactions* **26** (1), 17–32.

Noack, B., Afanasiev, K., Morzynski, M., Tadmor, G. & Thiele, F. 2003 A hierarchy of low-dimensional models for the transient and post-transient cylinder wake. *J. Fluid Mech.* **497**, 335–363.

Nordström, J., Nordin, N. & Henningson, D. 1999 The fringe region technique and the fourier method used in the direct numerical simulation of spatially evolving viscous flows. *SIAM J. Sci. Comput.* **20** (4), 1365–1393.

Rempfer, D. & Fasel, H. 1994 Evolution of three-dimensional coheren structures in a flat-plate boundary layer. *J. Fluid. Mech.* **260**, 351–375.

Rowley, C. W. 2005 Model reduction for fluids using balanced proper orthogonal decomposition. *Int. J. Bifurc. Chaos* **15** (3), 997–1013.

Siegel, S. G., Seidel, J., Fagley, C., Luchtenburg, D. M., Cohen, K. & McLaughlin, T. 2008 Low dimensional modelling of a transient cylinder wake using double proper orthogonal decomposition. *J. Fluid Mech.* In press.

Sirovich, L. 1987 Turbulence and the dynamics of coherent structures i-iii. *Quart. Appl. Math.* **45**, 561–590.

Willcox, K. & Peraire, J. 2002 Balanced model reduction via the proper orthogonal decomposition. *AIAA J.* **40** (11), 2323–2330.

Zhou, K., Doyle, J. & Glover, K. 2002 *Robust and Optimal Control*. New Jersey: Prentice Hall.

Zhou, K., Salomon, G. & Wu, E. 1999 Balanced realization and model reduction for unstable systems. *Int. J. Robust Nonlinear Control* **9**, 183–198.

Paper 3

3

The global stability of the jet in crossflow

By Shervin Bagheri, Philipp Schlatter & Dan S. Henningson

Linné Flow Centre, Department of Mechanics
Royal Institute of Technology, S-100 44 Stockholm, Sweden

Internal report

The global stability of the jet in crossflow is investigated by numerical simulation. The Navier–Stokes equations are linearized around a fully three-dimensional steady-state solution, computed numerically using the Selective Frequency Damping (SFD) method. Using the Arnoldi method and a DNS code as a time-stepper the most unstable eigenmodes of the linearized system are computed. The flow is found globally linearly unstable for a velocity ratio $R = 3$, defined as ratio of the centerline jet velocity and crossflow. The temporal frequency of the obtained eigenmode is in good agreement with the dominant frequency observed in the nonlinear DNS simulations.

---

1. Introduction

In hydrodynamic stability theory, spatially developing flows can be categorized according to their response to forcing. Certain flows, such as the wake behind circular cylinder (Giannetti & Luchini 2007), flow over a cavity (Åkervik *et al.* 2007) and a backward-facing step (Barkley *et al.* 2002) are in specific parameter ranges insensitive to external forcing and may sustain synchronized periodic oscillations. Other flows such as co-flow mixing layers (Huerre & Monkewitz 1990) and boundary layers (Ehrenstein & Gallaire 2005) act as noise amplifiers and can be very sensitive to external forcing. In particular, constant-density free jets (Huerre & Monkewitz 1990) belong to the latter class whereas hot jets (Nichols *et al.* 2007) and swirling jets (Gallaire & Chomaz 2003) belong the former. In this paper we show that the jet in crossflow is able to sustain periodic oscillations. To the authors knowledge this is the first linear stability analysis of the viscous jet in crossflow and in particular of a flow configuration where all three spatial directions are inhomogeneous.

The jet in crossflow is ubiquitous in industrial applications, such as film cooling, fuel injection etc. The flow structures, mixing properties and dynamics has therefore been the subject of numerous experimental and computational studies. In general four main coherent structures (see *e.g.* Fric & Roshko (1994); Kelso *et al.* (1996); Smith & M.G. (1996); Yuan *et al.* (1999); Cortelezzi & Karagozian (2001); Muppidi & Mahesh (2007); Megerian *et al.* (2007) and references therein) characterize the jet in crossflow; (i) the counter-rotating

vortices pair which seem to originate in the near field and dominate the flow field far downstream; (ii) shear layer vortices which take the form of ring-like or loop-like shapes (iii) horseshoe vortices formed by the flat-wall boundary layer (iv) "wall-vortices/upright vortices" which lie above the flat wall and are vertically oriented shedding vortices.

Recent advanced in computational methods has enabled global stability analysis of flows with arbitrary complexity, *i.e.* flows that are not required to vary slowly in the streamwise direction. In particular, recent methods for computing steady-states and very large eigenvalue problems based on the minimal modifications of existing Navier–Stokes codes, have enabled the study of the disturbance dynamics of complex flows. Using the selective frequency damping (SFD) method introduced by (Åkervik *et al.* 2006) steady-state solution to the Navier–Stokes equations can be found for unstable flow configuration by including a simple forcing term. The eigenmodes of the linearized Navier–Stokes equations can also be computed by using a simulation code (Barkley *et al.* 2002) in combination with the Arnoldi method, for which the software library ARPACK (Lehoucq *et al.* 1998) is available.

The paper is organized as follows. Section 2 introduces the numerical setup together with the relevant parameters used in the present study. A short description of the flow structure taken from a direct numerical section is also given. Section 3 deals with the linear three-dimensional stability analysis. First, the method and the resulting velocity field pertaining to a steady state solution of the jet in crossflow are described, followed by an analysis of a linear impulse response developing on this steady state. The section ends with the numerical method based on a time-stepper approach to extract fully three-dimensional eigenmodes. Conclusions and an outlook are given in section 4.

2. Numerical method and discretization

2.1. *Flow configuration*

The stability of the jet in crossflow is analyzed via fully-resolved direct numerical simulation based on the incompressible Navier–Stokes equations. The computational domain employed here consists of a rectangular box containing the crossflow boundary layer under zero pressure gradient, starting at a finite Reynolds number $Re_{\delta_0^*}$ downstream of the leading edge. Here, the Reynolds number is based on the displacement thickness δ_0^* of the undisturbed laminar Blasius profile. The jet is then discharged via non-homogeneous boundary conditions of the wall-normal velocity component at the lower wall ($y = 0$) at a distance downstream of the inlet x_{jet}. The inflow condition of the jet is described in section 2.2 below.

The simulation code (see Chevalier *et al.* (2007)) employed for the simulations presented here uses spectral methods to solve the three-dimensional time-dependent incompressible Navier–Stokes equations over a flat plate. The streamwise, wall-normal and spanwise directions are denoted by x, y and z,

respectively, and the corresponding velocity vector is $\boldsymbol{u} = (u, v, w)^T$,

$$\frac{\partial \boldsymbol{u}}{\partial t} + (\boldsymbol{u} \cdot \nabla)\boldsymbol{u} = -\nabla p + \frac{1}{Re_{\delta_0^*}} \nabla^2 \boldsymbol{u} + F(\boldsymbol{u}) \ , \tag{1}$$

$$\nabla \cdot \boldsymbol{u} = 0 \ , \tag{2}$$

with the pressure p. The volume forcing $F(\boldsymbol{u})$ is described further below. The algorithm is based on Fourier discretization in the streamwise and spanwise directions, and the wall-normal direction is expanded in Chebyshev polynomials. For efficiency reasons, the nonlinear convection terms are evaluated pseudo-spectrally in physical space using fast Fourier transforms; the corresponding aliasing errors from the evaluation of the nonlinear terms are removed by the 3/2-rule in the wall-parallel x/z plane. In the wall-normal direction, it has been chosen to increase resolution instead rather than to use polynomial dealiasing. The time is advanced using a standard four-step low-storage third-order Runge–Kutta method for the nonlinear terms and volume force terms $F(\boldsymbol{u})$, and a second-order Crank–Nicholson method is employed for the linear terms. The code is fully parallelized for efficient use on both shared and distributed-memory systems.

To correctly account for the downstream growth of the boundary layer of the crossflow, a spatial technique is necessary. This requirement is combined with the periodic boundary conditions in the streamwise direction by adding a fringe region, similar to that described by Bertolotti *et al.* (1992), see also Nordström *et al.* (1999). In this region, located at the downstream end of the computational box, the flow is forced to a desired solution $\mathbf{v}$ through the forcing (Chevalier *et al.* 2007),

$$F(\boldsymbol{u}) = \lambda(x)(\mathbf{v} - \boldsymbol{u}) \ . \tag{3}$$

The desired in- and outflow velocity vector $\mathbf{v}$ may depend on the three spatial coordinates and time. It is smoothly changed from the laminar boundary-layer profile at the beginning of the fringe region to the prescribed inflow velocity vector. In the present case, this is chosen as the laminar Blasius boundary-layer profile, but may also contain desired inflow disturbances. In the spanwise direction, periodic boundary conditions are used, in accordance with the Fourier discretization in that direction.

All quantities are non-dimensionalized using the (constant) free-stream velocity U_∞, the viscosity ν and the displacement thickness at the inlet of the crossflow into the computational box δ_0^* ($x = 0$). The computational Reynolds number is thus $Re_{\delta_0^*} = U_\infty \delta_0^* / \nu$. For the undisturbed Blasius solution, the 99%-boundary-layer thickness $\delta_{99} \approx 2.85\delta^*$.

2.2. *Jet boundary conditions and simulation parameters*

The computational domain is a rectangular box containing the boundary layer of the crossflow. Due to the spectral discretization method employed, it is not directly possible to adapt the computational grid in such a way to include a discretized model of the jet nozzle in the flat plate. The jet discharging into

Parameter	Definition	Parabolic profile eq. (5)	Yuan *et al.* (1999)
$R(v_j)$	v_j/U_∞	3	4.3
$R(\bar{v}_j)$	$\bar{v}_j/U_\infty$	1	3.3
δ_0^*/D		0.33	0.17
δ_{nozzle}^*/D		0.39	0.22
D		3	5.7
$Re_{\delta_0^*}$	$U_\infty\delta_0^*/\nu$	165	184
Re_D	$U_\infty D/\nu$	500	1050
Box size	(x, y, z)	(75,20,30)	(72.4,45.6,51.3)

TABLE 1. Parameters and comparison with Yuan *et al.* (1999). Note that the latter reference employed a turbulent inflow profile. The numerical resolution is $(N_x, N_y, N_z) = (256, 201, 144)$ collocation points in physical space.

the crossflow boundary layer is therefore modelled by imposing inhomogeneous boundary conditions of the wall-normal v velocity component on the flat plate. This simplified model of course does not allow for any interaction of the crossflow with the nozzle (see *e.g.* Yuan *et al.* (1999)). However, the instabilities explored in the present study focus mainly on the interaction of the crossflow and the shear layer further away from the wall. At that position, the influence of the immediate nozzle interactions can be assumed to be small.

On the flat plate, homogeneous boundary conditions for the wall-parallel velocity components u and w are prescribed, corresponding to the no-slip boundary conditions. The main parameters of the jet are the position of the center of the jet orifice $(x_{\text{jet}}, z_{\text{jet}})$, the jet diameter D and the inflow ratio

$$R = \frac{v_{\text{jet}}}{U_\infty} \tag{4}$$

of the centerline velocity v_{jet} and the crossflow velocity U_∞.

The jet discharging into the crossflow is imposed by a wall-normal velocity

$$v(r, y = 0) = R(1 - r^2)e^{-(r/0.7)^4} , \tag{5}$$

with r being the distance from the jet center $(x_{\text{jet}}, z_{\text{jet}})$, normalized with the jet diameter D,

$$r = (2/D)\sqrt{(x - x_{\text{jet}})^2 + (z - z_{\text{jet}})^2} . \tag{6}$$

This inflow profile corresponds to a (laminar) parabolic velocity profile of the pipe flow, smoothened with a Gaussian function to allow for an efficient treatment with the spectral discretization of the simulation code. Note that the wall-normal velocity component v corresponds to the inflow ratio R in the jet center, and is less than $10^{-5}R$ for $D/2 > 1.276$. For the boundary condition given in equation (5) the relation between the bulk and the maximum velocity in the center of the jet is approximately 3.

Although physically the boundary layer is assumed to extend to an infinite distance from the wall, the discretization requires a finite domain. Therefore,

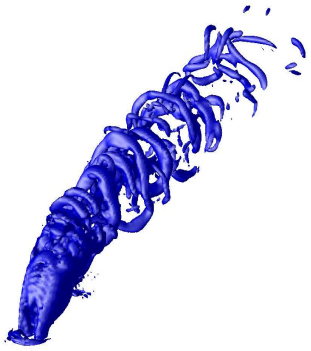

FIGURE 1. Snapshot of the velocity field in a fully-developed state at $t = 151$ based on the unsteady Navier–Stokes equations. The blue isocontours correspond to vortical structures visualized with the λ_2 criterion (Jeong & Hussain 1995) at a level $\lambda_2 = -0.11$.

an artificial boundary condition is applied in the free-stream at wall-normal position y_L via a Neumann condition

$$\left.\frac{\partial \boldsymbol{u}}{\partial y}\right|_{y=y_L} = \left.\frac{\partial \mathbf{v}}{\partial y}\right|_{y=y_L} . \tag{7}$$

Various physical and computational parameters of the present simulations are summarized in table 2.1 in comparison with the large-eddy simulations presented by Yuan *et al.* (1999) for a turbulent inflow profile. Note that for the present simulations the Reynolds number was chosen slightly lower, however, fully resolved DNS is used instead of applying a subgrid-scale model.

The computations presented here were performed with a resolution of $(N_x, N_y, N_z) = (256, 201, 144)$ grid points. Due to the dense distribution of the Chebyshev collocation points close to the wall and the strong wall-normal velocity component, the time step had to be chosen rather small $\Delta T \approx 3 \cdot 10^{-4}$. The simulations were run on a Linux cluster; one iteration took on 48 cores (clock rate 3GHz) approximately 3 seconds.

2.3. *Direct numerical simulation*

The simulation of the jet in crossflow is initiated from a laminar Blasius profile above the flat plate. At time $t \geq 0$, the inhomogeneous boundary condition (5) is imposed to release the jet into the computational domain. After approximately 50 non-dimensional time units, a statistically stationary state can be observed.

A snapshot at $t = 151$ of the flow development is shown in figure 1, where isocontours of the λ_2 vortex-identification criterion (Jeong & Hussain 1995) are

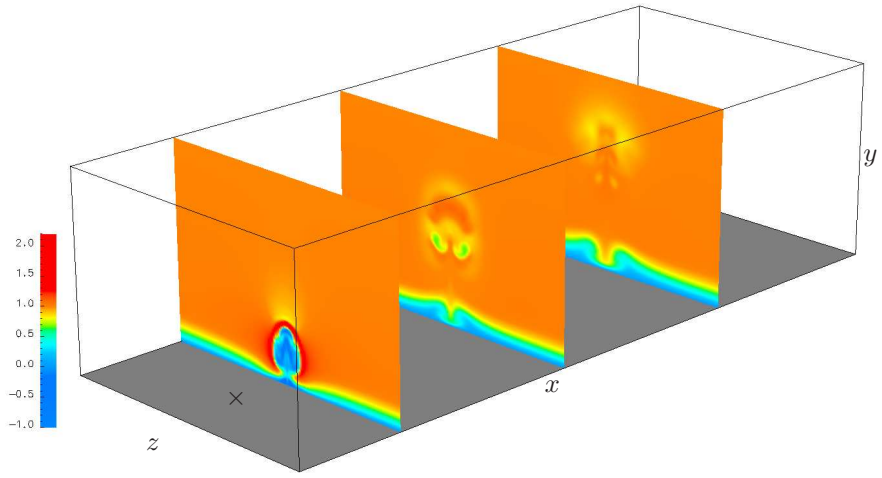

FIGURE 2. Crossplanes of the streamwise velocity component u pertaining to the unsteady DNS simulation at $t = 151$. The center of the jet nozzle is indicated by the cross $\times$. The streamwise location of the planes correspond to $x = 11.7, 32.3$ and 58.8, respectively.

displayed. Although both the boundary layer of the crossflow as well as the incoming flow pertaining to the jet are laminar, the resulting interaction results in a highly unsteady flow field. Vortical motion as depicted in figure 1 resulting from the interaction of the vorticity of both the jet profile and the boundary-layer shear layer are first advected nearly in vertical (y) direction, only slightly deflected in the streamwise direction. At the upstream edge of the jet body, where shear layer is the strongest, a flow instability is clearly developing and consequently leading to a breakup of the laminar flow into a sequence of finer-scale, half-ring shaped vortex rolls. As these structures convect downstream their direction gradually aligns with the free-stream and they dissipate due to viscous effects.

Careful inspection of the velocity fields of the unsteady direct simulations further reveal well-known distinct flow features as discussed in *e.g.* Fric & Roshko (1994): Wrapping around the jet nozzle, a number of horseshoe-shaped vortices, located essentially in the crossflow boundary layer, can be detected. In addition, the core of the discharged jet is composed of two large-scale counter-rotating vortices (see section 3 further down), on which the shear-layer vortices develop. These vortices are the most obvious structures in figure 1. On the other hand, the wake vortices connecting the crossflow boundary layer and the jet body, being reminiscent of the vortex street behind bluff bodies, are not

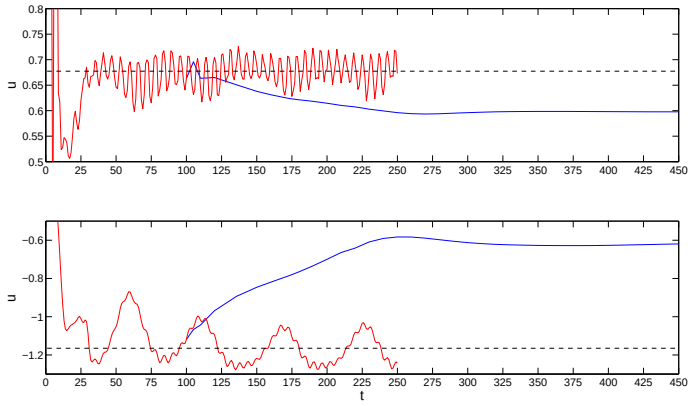

FIGURE 3. Time signals corresponding to the (streamwise) u-component of two probes in the flow field. In the upper graph the probe is located within the upper shear layer, whereas in lower diagram it is placed a short distance downstream of the orifice close to the wall. The red line represents the (unsteady) DNS simulation, whereas the blue line corresponds to the simulation stabilized with SFD, active for $t > 100$ (see section 3). The dashed lines indicate the time-averaged values of the DNS simulation.

visible in the present setup. As stated by Fric & Roshko (1994) these vortices appear preferably with higher inflow ratios. At lower R, the spanwise symmetry of the flow field is sustained as in the present case.

Another view of the unsteady DNS results is provided in figure 2 for the same time instant as figure 1. The modulation of the crossflow boundary layer downstream of the jet nozzle is clearly visible; namely the two legs of the horseshoe vortices transport fluid from the outer region closer to the wall, leading to a high-speed region in the symmetry plane $z = 0$. This region is widening as the boundary layer is growing in the downstream direction.

In figure 3 time signals of two probes in the flow are presented; one probe is located within the jet shear layer slightly upstream of the jet body at a distance from the wall $y = 3D$, and the other probe is positioned downstream of the jet orifice close to the wall. The time signals clearly show the transient phase up to $t \approx 50$ in which the flow field develops. Two distinct frequencies in both time series can be detected; in the jet shear layer a period $T_1 \approx 5.7$ can be estimated, whereas in the wake of the jet a much longer period of $T_2 \approx 60$ is present. The Strouhal number, defined as $St = D/(T\overline{v}_{jet})$, associated with the two frequencies is $St = .17$ and $St = 0.016$ respectively.

It is interesting to note that the velocity signal recorded by the second probe is negative $u \approx -1.1$. This indicates that shortly downstream of the jet nozzle an extended region of separated flow exists. The signal recorded in that region oscillates at a comparably low frequency. However, this separation bubble appears to only oscillate in a spanwise-symmetric manner, as the symmetry of the flow field in the near field of the jet nozzle is never broken. As mentioned above, with the present setup no upright wake vortices shed away from the jet body are to be detected.

On the other hand, the frequency measured in the jet shear layer corresponds to the incipient vortical structures caused by the presence of the inflowing jet. However, even in the shear layer the lower frequency present in the wake downstream of the nozzle is clearly felt, manifesting itself as a slow modulation of the probe signals. This indicates that the whole jet is oscillating with that long period T_2.

The direct simulations of the jet and the analysis of the corresponding velocity fields demonstrate that an accurate simulation of the flow case is possible. In particular, the results show that the modeling of the jet as an inhomogeneous boundary condition rather than the more costly discretization of the nozzle and the attached pipe is indeed able to reproduce the main characteristics of the flow case. The main dominant features and instabilities are all present in our data. However, the direct interaction of crossflow boundary layer and jet nozzle is certainly an important aspect if the aim of the study is to predict statistical quantities related to a specific setup of the problem (Reynolds number, inflow ratio *etc.* as *e.g.* discussed by Yuan *et al.* (1999)). On the other hand, the present study focuses on the stability of the jet-in-crossflow problem arising mainly from the shear-layer vortices located further away from the wall, for which the present setup is found to be adequate.

3. Linear stability analysis

In the present section we investigate the evolution of infinitesimal perturbations $\boldsymbol{u}'$ to a base flow $j\boldsymbol{u}$ which is a steady solution to Navier–Stokes equations (1). The governing equations of these perturbations are found by inserting $\boldsymbol{u} = \mathbf{U} + \epsilon\boldsymbol{u}'$ and $p = P + \epsilon p'$, where p' is the pressure perturbations, into (1) and neglecting the terms of order ϵ^2. The resulting linearized Navier–Stokes equations (LNS) are,

$$\frac{\partial \boldsymbol{u}'}{\partial t} + (\mathbf{U}\cdot\nabla)\boldsymbol{u}' + (\boldsymbol{u}'\cdot\nabla)\mathbf{U} = -\nabla p' + \frac{1}{Re_{\delta_0^*}}\nabla^2\boldsymbol{u}' + F(\mathbf{U},\boldsymbol{u}') \ , \quad (8)$$

$$\nabla\cdot\boldsymbol{u}' = 0 \ . \quad (9)$$

These equations are solved subject to the same boundary conditions in x, y and z as (1). Note that since the LNS describe the perturbation dynamics, the jet boundary condition is no longer imposed.

Discretizing the equations (8) in space and enforcing the incompressibility condition[1] the partial differential equation can be represented by the initial value problem

$$\frac{\partial \boldsymbol{u}}{\partial t} = A\boldsymbol{u}, \tag{10}$$

$$\boldsymbol{u}(t=0) = \boldsymbol{u}_0 \ . \tag{11}$$

The discretized and linearized Navier–Stokes equations including boundary conditions are represented by the action of the matrix A on $\boldsymbol{u}$. Note that the matrix A is never explicitly constructed and that the LNS are solved according to the description given in section 2. If the base flow is a steady solution, the equations (11) are autonomous and the eigenmodes of A are of the form

$$\boldsymbol{u}(x,t)' = e^{\lambda_j t}\phi_j(\boldsymbol{x}) \ , \tag{12}$$

where both the eigenvalues λ_j and eigenmodes ϕ_j are complex functions.

With the use of the DNS code described in section 2 the stability analysis is performed in two steps; we begin with computing a steady solution to equations (1) using the selective frequency damping method (Åkervik *et al.* 2006), then continue by computing the eigenmodes of A using the Arnoldi algorithm via the parallel ARPACK library (Lehoucq *et al.* 1998).

3.1. *Steady solution*

3.1.1. *Selective frequency damping (SFD)*

When a flow under consideration is either globally unstable or strongly convectively unstable, the computation of a steady-state solution $\overline{\boldsymbol{u}}$ of the Navier–Stokes equations (1) poses is a challenging task. Alternatively, the class of Newton iteration methods, which require heavy computational resources for large systems, might be applied. However, such methods rely on a specialized numerical code to perform the iteration; additionally, for large numbers of degrees of freedom the convergence of the Newton iteration is yet unclear. Therefore, to obtain a steady state to the jet in crossflow, another method termed selective frequency damping (SFD), recently proposed by (Åkervik *et al.* 2006) is employed. This method consists of the inclusion of an additional forcing term in the governing equations, which is effectively damping the most dangerous frequencies present in the flow and thus quenching the corresponding instability. The idea of SFD is to continuously force the velocity field towards a temporally low-pass filtered state, denoted $\hat{\boldsymbol{u}}$. Such a forcing is given by

$$-\chi(\boldsymbol{u} - \hat{\boldsymbol{u}}) \ , \tag{13}$$

with a model coefficient χ to be determined. A convenient way to compute a temporal low-pass filtered velocity field is obtained by using the differential

[1] This is equivalent to projecting the flow field on divergence-free subspace. In our case it is accomplished by transformation of the primitive variable to wall-normal velocity and vorticity.

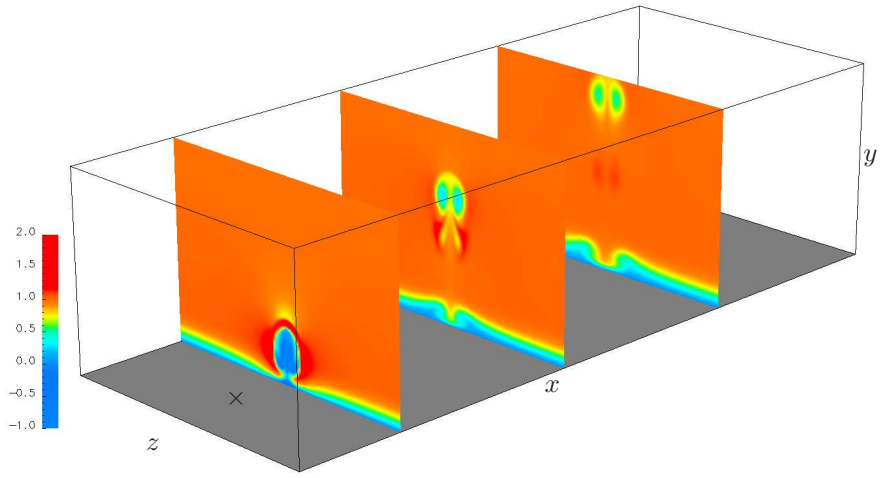

FIGURE 4. Crossplanes of the streamwise velocity component u pertaining to the steady state obtained by SFD. The center of the jet nozzle is indicated by the cross $\times$.

form of the exponential (causal) filter (Pruett *et al.* 2003),

$$\frac{\partial \hat{\boldsymbol{u}}}{\partial t} = \frac{1}{\Delta}(\boldsymbol{u} - \hat{\boldsymbol{u}}) \ , \tag{14}$$

with a filter width Δ, which has to be chosen in such a way that the lowest unstable frequencies are sufficiently dampened. Further details on the choice of the two model parameters χ and Δ are given in (Åkervik *et al.* 2006). For the present case, the damping factor was chosen to be $\chi = 1$, and the filter width was set to $\Delta = 2$. The associated period for which the transfer function of temporal filter (14) is (1/2) is given by $T_c = 2\pi\Delta \approx 12.6$; this value for the filter width is in good agreement with the measured period of the shear-layer vortices $T_1 \approx 5.7$.

figure 3 shows the filtering effect of SFD on the flow solution. The SFD run is started from the unsteady flow field at $t = 100$. The oscillations present in the flow are quickly damped. It is noteworthy that both the oscillations in the jet shear layer and the ones in the wake of the jet are equally quenched, although they are characterized by different frequencies. At later times the SFD solution clearly shows no oscillations anymore, and a steady state is gradually reached. Note that when the SFD has converged to a steady solution $\hat{\boldsymbol{u}}$ the forcing in equation (13) is zero, yielding a steady state solution to the unmodified Navier–Stokes equations (1).

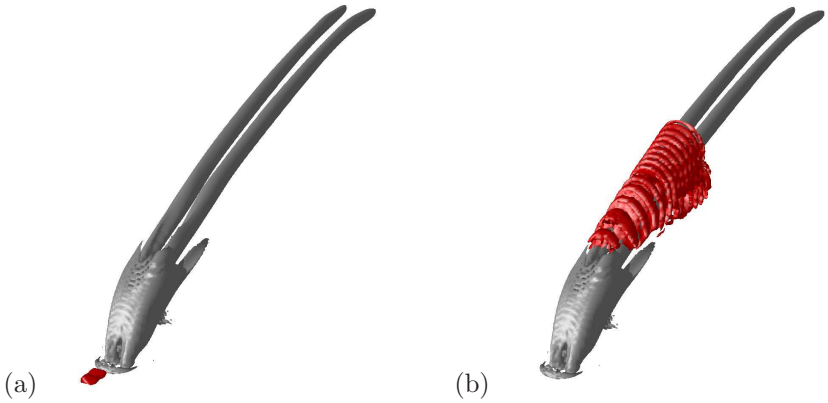

FIGURE 5. Numerical simulation of the linearized Navier–Stokes equations. The gray isocontours indicate the steady base flow. In (a) the red isocontours represent the initial perturbation upstream of the jet at $t = 0$. As the perturbation is convected downstream it travels on the shear layer and wraps around the CVP as shown $t = 24$ in (b).

3.1.2. *Steady state and the counter-rotating vortex pair*

The velocity fields pertaining to the steady state after convergence of the SFD method is displayed in figures 4 and 5 and can be compared to the corresponding visualizations of the unsteady DNS, figures 1 and 2.

Cross planes of the streamwise velocity component are given in figure 4. Compared to the unstabilized case there is little difference in the near-wall region, *i.e.* the structure of the horseshoe vortices and the subsequent impact of the jet onto the deformation of the boundary layer appears to not be time-dependent even in the unsteady case. On the other hand, the inner structure of the jet (planes 2 and 3 in figure 4) appears fairly different comparing the steady and instantaneous solution. In particular, the counter-rotating vortex pair is only clearly detectable in the SFD field. This indicates that the motions along the CVP are highly instationary.

A three-dimensional impression of the steady state obtained by SFD can be gained from figure 5(a), showing isocountours of the λ_2 criterion. Naturally, the unsteady development of vortices in the jet shear layer, clearly visible in the snapshot of the DNS in figure 1, is not present anymore in the steady state. Similarly, unsteady wake vortices do not develop.

On the other hand, the (steady) counter-rotating vortex pair (CVP) is evident as two distinct tubes of negative λ_2, deflected along the jet trajectory and slowly decaying in the streamwise direction. It is interesting to note that the CVP does not directly start at the jet nozzle, but rather becomes apparent

approximately at a wall-normal height of $3D$; closer to the wall there is a vortex sheet wrapped around. Physically, the appearance of the CVP can be explained by the accumulation of the azimuthal vorticity related to the discharging jet fluid, which is redirected in the direction of the jet trajectory due to the interaction with the crossflow (Fric & Roshko 1994).

Additionally, the steady state features the horseshoe shaped vortex forming around the jet nozzle. Due to this vortex, a small separated region is formed just upstream of the jet nozzle. Streamlines released close to the axis of the horseshoe vortex will be curved around the jet nozzle, and continue their swirly motion downstream of the jet exit, aligned with the streamwise direction; however not leaving the boundary layer. Moreover, a larger region with negative streamwise velocity is formed at the downstream edge of the nozzle related to entrainment of fluid from the crossflow into the jet.

The steady state obtained by SFD satisfies the steady Navier–Stokes equations,

$$(\overline{\boldsymbol{u}} \cdot \nabla)\overline{\boldsymbol{u}} = -\nabla \overline{p} + \frac{1}{Re_{\delta_0^*}} \nabla^2 \overline{\boldsymbol{u}} + F(\overline{\boldsymbol{u}}) \ , \tag{15}$$

$$\nabla \cdot \overline{\boldsymbol{u}} = 0 \ . \tag{16}$$

On the other hand, the unsteady fields from DNS can also be averaged in time to obtain the solution to the Reynolds-averaged Navier–Stokes (RANS) equations,

$$(\langle \boldsymbol{u} \rangle \cdot \nabla)\langle \boldsymbol{u} \rangle = -\nabla \langle p \rangle + \frac{1}{Re_{\delta_0^*}} \nabla^2 \langle \boldsymbol{u} \rangle + F(\langle \boldsymbol{u} \rangle) + \nabla \cdot \mathbf{T} \ , \tag{17}$$

$$\nabla \cdot \langle \boldsymbol{u} \rangle = 0 \ . \tag{18}$$

The Reynolds stresses $\mathbf{T}$ are defined based on the fluctuations around the mean $u_i = \langle u_i \rangle + u_i'$ as

$$T_{ij} = \langle u_i' u_j' \rangle \ . \tag{19}$$

It is obvious that $\overline{\boldsymbol{u}} \neq \langle \boldsymbol{u} \rangle$ since $\mathbf{T} \neq 0$ due to the unsteady formation of vortices in both the jet shear layer and the wake region. This difference is further exemplified in figure 3 in which the time signals of the probes pertaining to the (unsteady) DNS are clearly different than those obtained from the converged SFD solution. In particular, the solution of the RANS equations exhibits increased momentum diffusion due to the Reynolds stresses; in consequence, the jet trajectory obtained via SFD is reaching up to a greater wall-normal distance than the one related to the averaged solution, as can be seen by comparing figures 2 and 4.

We like to emphasize that the time-averaged mean flow is not an equilibrium point of the Navier–Stokes equations, in contrast to steady-state solutions or limit cycles. Therefore, it is not a suitable choice for a base flow, since the resulting critical bifurcation points obtained from the stability analysis might not reflect the actual instability transitions present in the flow.

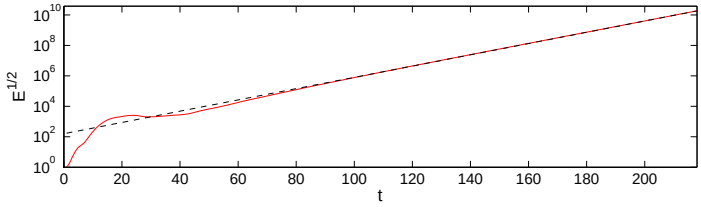

FIGURE 6. Comparison of the most unstable global eigenmode and the asymptotic evolution of perturbation. The energy of the disturbance is compared to the growth rate $\sigma = 0.08$ given by the global eigenvalue analysis.

3.2. *Linear impulse response*

The global stability or instability is defined as the long-time behaviour of the base flow to an initial impulse at $t = 0$. The spatially developing flow is said to be globally unstable if the response grows without bound as time goes to infinity. We introduce an initial pulse of a Gaussian-type function inside the boundary layer upstream of the jet nozzle, see figure 5(a). In figure 5(b) the response of the base flow to the impulse is shown after 24 time units. The initial condition has triggered a wavepacket which grows in amplitude as it is travels along the base flow. In figure 6(a) the temporal evolution of the perturbation energy extracted from the shear-layer vortex is shown with logarithmic vertical axis. After an initial transient growth, we observe the asymptotic exponential growth of the disturbance. The base flow is therefore deemed linearly globally unstable and according to linear theory the impulse response for $t \to \infty$ is dominated by the most unstable linear mode.

3.3. *Global stability analysis*

3.3.1. *Time-stepper technique*

In this section, we demonstrate how the global eigenmodes of the linearized Navier–Stokes equations given in equation (11) are computed using a "time-stepper" technique. We wish to solve the following eigenvalue problem

$$A\Phi = \Lambda\Phi \ , \tag{20}$$

where A represents the action of the linearized Navier–Stokes operator, the columns of Φ contain the global eigenmodes, $\Phi = [\phi_1, \ldots, \phi_n]$ and Λ is a diagonal matrix containing the eigenvalues of A, *i.e.* $\Lambda = \mathrm{diag}\{\lambda_1, \ldots, \lambda_n\}$. Even with iterative methods, such as the Arnoldi method, it is in general not possible to explicitly solve the eigenvalue problem (20). The reason is that the matrix A cannot be stored in memory due to its large dimension, which is on the order of $10^7 \times 10^7$ for the present numerical resolution.

Instead we make use of our DNS code and a time-stepper technique similar to that described by Barkley *et al.* (2002). First, we observe that the global

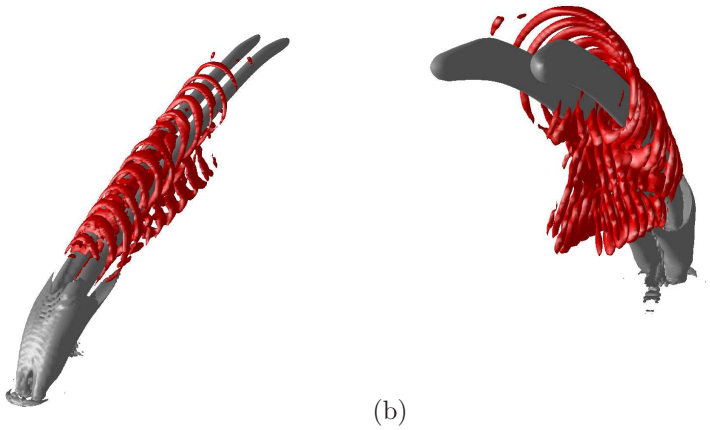

(a) (b)

FIGURE 7. The real part of the most unstable global eigenmode is shown with red and the base flow with gray isocontours of λ_2. The associated non-dimensional growth rates and frequencies are 0.08 and 1.1, respectively.

eigenmodes are invariant under the transformation e^{At} (for fixed time t)

$$e^{At}\Phi = \Phi\Sigma \ , \tag{21}$$

where $\Sigma = e^{\Lambda t}$. Second, we recognize that the action of the matrix exponential on the velocity field $\boldsymbol{u}(t)$

$$\boldsymbol{u}(t+\Delta t) = e^{A(t+\Delta t)}\boldsymbol{u}(t) \tag{22}$$

represents integrating the linearized Navier–Stokes equations over a time interval Δt. In the time-stepper approach we solve the eigenvalue problem (21) for Φ using an iterative method and recover the eigenvalues of A from

$$\Lambda = \frac{1}{\Delta t}\log(\Sigma) \ . \tag{23}$$

In general, the iterative technique is based on the orthogonal projection of the large matrix onto a lower dimensional subspace, which will result in a significantly smaller system that can be solved using direct methods. A particularly useful subspace is the Krylov subspace spanned by snapshots taken from the evolving flow field at every Δt

$$V = [\boldsymbol{u}(\boldsymbol{x},0), \boldsymbol{u}(\boldsymbol{x},\Delta t), \boldsymbol{u}(\boldsymbol{x},2\Delta t), \ldots, \boldsymbol{u}(\boldsymbol{x},(m-1)\Delta t)] \ , \tag{24}$$

where $\boldsymbol{u}(\boldsymbol{x},0)$ is an initial guess that contains at least one component in the direction of leading eigenmodes. Note that instead of collecting snapshots from one simulation of length $(m-1)\Delta t$ and then orthogonalizing the columns of V, we perform $m-1$ DNS simulations of length Δt in time and between each DNS simulation a snapshot is orthogonalized with all the previous snapshots

using the Gram-Schmidt method. The former method can yield a very ill-conditioned matrix V, since the columns of V all tend to approximate the dominant eigenmodes.

Once this Krylov subspace is constructed we solve the small $m \times m$ eigenvalue problem

$$e^{Ht} S = \Sigma S \ , \tag{25}$$

where columns of S contain the the eigenvectors of e^{Ht} and e^{Ht} is the projection of matrix exponential onto V,

$$e^{At} = V e^{Ht} V^T \ . \tag{26}$$

The global eigenmodes can then be recovered from $\Phi = VS$.

3.3.2. *Global eigenmodes*

We have used the parallel ARPACK software (Lehoucq *et al.* 1998) to solve equation (21), which implements an algorithmic variant of the Arnoldi process called the Implicitly Restarted Arnoldi Method (IRAM). The number of Krylov subspace was chosen as 12 and the integration time $\Delta t = 2$. Note that the choice of Δt should reflect the time scales of the physical structures in the flow. It should be small enough to allow for the eigenmodes associated with high frequencies to be captured (*i.e.* satisfying the Nyquist criterion). On the other hand if Δt is too small the consecutive column vectors of V are nearly parallel since the flow has not evolved significantly.

In figure 7 the eigenmode with the largest growth rate is shown with red isocontours of λ_2 together with the steady base flow in gray. The non-dimensional growth rate and Strouhal number of this dominant mode is $\sigma = 0.04$ and $St = .175$. The Strouhal number obtained from the global analysis is in good agreement with the one observed in our DNS simulation (see figure 3). Note that it is only in the neighbourhood of the critical point that the Strouhal number of the dominant global mode can be associated with the Strouhal number of the vortex shedding in the shear layer. This indicates that $R = 3$ is close to the critical point. The velocity ratio at which the onset of instability occurs is currently under investigation. In particular the recent experimental results of Megerian *et al.* (2007) indicate (for different flow parameters) that the onset to instability is close to $R = 3.5$ and that larger values of R yield a noise-amplifying behavior.

The mode in figure 7 takes the shape of a localized wave packet wrapped around the counter-rotating vortex pair. From the DNS simulation, we could observe a specific location where the periodic vortices where being shed away into the downstream direction. This region is located on the shear layer, approximately 2-3 jet diameters from the nozzle along the jet trajectory. Note that the global eigenmode is located further downstream on the trajectory, where the vortex loops traveling downstream are the largest. For other globally unstable flows, such as the cylinder wake (Giannetti & Luchini 2007) and hot jets (Nichols *et al.* 2007), a specific spatial region can be identified which

acts as a wavemaker providing a precise frequency-selection criterion. This is related to a region of local absolute instability (Huerre 2000). We are pursuing further investigations in order to find whether the jet spatially transitions from absolute to convective instability, *i.e.* the existence of a pocket of absolute instability near the jet inlet followed by a region of convective instability downstream of the jet trajectory.

4. Conclusions and outlook

The occurrence of self-sustained synchronized oscillations of a jet in crossflow has numerically been observed for a velocity ratio of $R = 3$ by means of global stability analysis. The steady state with three inhomogeneous spatial directions is significantly different from the temporally averaged velocity field, both in terms of flow structures and trajectory. The steady solution is thus an important step for determining the true physical mechanisms of the observed vortical structures in the flow, in contrast to the traditional approach which is based almost entirely on the mean velocity field. In this work, we have recovered the evolution of the jet shear-layer vortices from a global linear analysis. However, it is expected that weaker instabilities are also present which can be associated with the wake vortices behind the jet connecting it with the boundary layer or even other vortical structures observed in literature, such as "hanging vortices" formed in the skewed mixing layers on the lateral edges of the jet (Yuan *et al.* 1999). These vortical structures could be represented by global modes with smaller growth rates than the dominant mode presented in this paper. Furthermore, a more complete stability analysis is in progress in order to determine the critical velocity ratio for the onset to instability.

Acknowledgements

The authors acknowledge the Swedish research council (VR) for project funding and the Swedish National Infrastructure for Computing (SNIC) for providing computer time. We also thank Luca Brandt and Peter Schmid for fruitful discussions.

References

Åkervik, E., Brandt, L., Henningson, D. S., Hœpffner, J., Marxen, O. & Schlatter, P. 2006 Steady solutions of the Navier-Stokes equations by selective frequency damping. *Phys. Fluids* **18** (068102), 1–4.

Åkervik, E., Hœpffner, J., Ehrenstein, U. & Henningson, D. S. 2007 Optimal growth, model reduction and control in a separated boundary-layer flow using global eigenmodes. *J. Fluid. Mech.* **579**, 305–314.

Barkley, D., Gomes, M. G. & Henderson, R. D. 2002 Three-dimensional instability in flow over a backward-facing step. *J. Fluid Mech.* **473**, 167–190.

Bertolotti, F. P., Herbert, T. & Spalart, P. R. 1992 Linear and nonlinear stability of the Blasius boundary layer. *J. Fluid Mech.* **242**, 441–474.

Chevalier, M., Schlatter, P., Lundbladh, A. & Henningson, D. S. 2007 simson - A Pseudo-Spectral Solver for Incompressible Boundary Layer Flows. *Tech. Rep.* TRITA-MEK 2007:07, ISBN 978-91-7178-838-2. KTH Mechanics, Stockholm, Sweden.

Cortelezzi, L. & Karagozian, A. 2001 On the formation of counter-rotating vortex pair in transverse jets. *J. Fluid Mech.* **446**, 347–373.

Ehrenstein, U. & Gallaire, F. 2005 On two-dimensional temporal modes in spatially evolving open flows: The flat-plate boundary layer. *J. Fluid Mech.* **536**, 209–218.

Fric, T. F. & Roshko, A. 1994 Vortical structure in the wake of a transverse jet. *J. Fluid Mech.* **279**, 1–47.

Gallaire, F. & Chomaz, J. 2003 Mode selection in swirling jet experiments: a linear stability analysis. *J. Fluid Mech.* **494**, 223–253.

Giannetti, F. & Luchini, P. 2007 Structural sensitivity of the first instability of the cylinder wake. *J. Fluid Mech.* **581**, 167–197.

Huerre, P. 2000 Open shear flow instabilities. In *Perspectives in Fluid Dynamics*, pp. 159–229. Cambridge University Press.

Huerre, P. & Monkewitz, P. A. 1990 Local and global instabilities in spatially developing flows. *Ann. Rev. Fluid Mech.* **22**, 471–573.

Jeong, J. & Hussain, F. 1995 On the identification of a vortex. *J. Fluid Mech.* **285**, 69–94.

Kelso, R., Lim, T. & Perry, A. 1996 An experimental study of round jets in cross-flow. *J. Fluid Mech.* **306**, 111–144.

Lehoucq, R., Sorensen, D. & Yang, C. 1998 *ARPACK Users' guide: Solution of Large-Scale Eigenvalue problems with implicitly restarted Arnoldi methods*. Philadelphia: SIAM.

Megerian, S., Davitian, L., Alves, L. & Karagozian, A. 2007 Transverse-jet shear-layer instabilities. part 1. experimental studies. *J. Fluid Mech.* **593**, 93–129.

Muppidi, S. & Mahesh, K. 2007 Direct numerical simulation of round turbulent jets in crossflow. *J. Fluid Mech.* **574**, 59–84.

Nichols, J. W., Schmid, P. J. & Riley, J. J. 2007 Self-sustained oscillations in variable-density round jets. *J. Fluid Mech.* **582**, 341–376.

Nordström, J., Nordin, N. & Henningson, D. S. 1999 The fringe region technique

and the Fourier method used in the direct numerical simulation of spatially evolving viscous flows. *SIAM J. Sci. Comput.* **20** (4), 1365–1393.

Pruett, C. D., Gatski, T. B., Grosch, C. E. & Thacker, W. D. 2003 The temporally filtered Navier-Stokes equations: Properties of the residual stress. *Phys. Fluids* **15** (8), 2127–2140.

Smith, S. & M.G., M. 1996 Mixing, structure and scaling of the in crossflow. *J. Fluid Mech.* **357**, 83–122.

Yuan, L. L., Street, R. L. & Ferziger, J. H. 1999 Large-eddy simulation of a round jet in crossflow. *J. Fluid Mech.* **379**, 71–104.

Paper 4

4

The stabilizing effect of streaks on TS-waves: A parametric study

By Shervin Bagheri[*] & Ardeshir Hanifi[*†]

[*]Linné Flow Centre and Department of Mechanics
Royal Institute of Technology, S-100 44 Stockholm, Sweden

[†]Swedish Defence Research Agency, SE-164 90 Stockholm, Sweden

Physics of Fluids 19, 078103 (2007)

The stabilizing effect of finite amplitude streaks on the linear growth of unstable perturbations (TS and oblique waves) is numerically investigated by means of the nonlinear Parabolized Stability Equations. We have found that for stabilization of a TS-wave, there exists an "optimal" spanwise spacing of the streaks. These streaks reach their maximum amplitudes close to the first neutral point of the TS-wave and induce the largest distortion of the mean flow in the unstable region of the TS-wave. For a such distribution, the required streak amplitude for complete stabilization of a given TS-wave is considerably lower than for $\beta = 0.45$, which is the optimal for streak growth and used in previous studies. We have also observed a damping effect of streaks on the growth rate of oblique waves in Blasius boundary layer and for TS-waves in Falkner-Skan boundary layers.

1. Introduction

In boundary-layer flows, the transition from a laminar state to a turbulent one is usually caused by growth and breakdown of small amplitude perturbations. For a long time the common understanding has been that any kind of flow perturbation inside the boundary layer has a promoting effect on transition. However, a number of recent studies (Saric *et al.* 1998; Cossu & Brandt 2002; Fransson *et al.* 2005, 2006) has indicated that certain types of perturbations inside the boundary layer can postpone the laminar-turbulent transition. General feature of these perturbations seems to be a modification of mean velocity profile to a more stable one. In two-dimensional mean flows, these are streaky structures which create regions of alternating negative and positive streamwise velocity perturbations. Streaks are usually found inside the boundary layers subjected to high free-stream turbulence. A damping effect of moderate amplitude free-stream turbulence on Tollmien-Schlichting (TS) waves have been observed in some experiments (Boiko *et al.* 1994). Numerical investigations of Cossu & Brandt (2002) showed a clear stabilizing effect of streaks on growth

of TS waves in Blasius flow. They reported an increasing damping effect with increasing streak amplitude. These results were later verified by experimental works of Fransson *et al.* (2005) who, generated the streaks by means of small roughness elements. Recently Fransson *et al.* (2006) also showed that these streaks can truly delay the transition. Here, the transition was triggered by means of high amplitude two-dimensional disturbances generated through random suction and blowing at the wall. These new results have received great attention, *e.g.* Choi (2006). However, in all these studies, both experimental and numerical, a single spanwise spacing ($\beta = 0.45$) of streaks has been used, which corresponds to the most growing streaks. Therefore, we aim to investigate whether other distributions of streaks are more efficient for stabilizing TS-waves, so that a lower streak amplitude would be required for transition delay. This is important because the amplitude of the streaks should not exceed the threshold for secondary instability and instead promoting the transition to turbulence. The present work is based on a parametric study of the streak spacing. The feasibility of such a study, requires a relative fast computational method, such as the nonlinear Parabolized Stability Equations (PSE)(Bertolotti *et al.* 1992).

2. Numerical Procedure

We consider flow disturbances which are periodic in time t and spanwise direction z. These disturbances are decomposed in Fourier modes as

$$\mathbf{q}(\mathbf{x},t) = \sum_{m=-M}^{M} \sum_{n=-N}^{N} \tilde{\mathbf{q}}_{mn}(x,y) \exp(in\beta_0 z - im\omega_0 t).$$

Here,

$$\tilde{\mathbf{q}}_{mn} = \hat{\mathbf{q}}_{mn}(x,y) \exp(i \int \alpha_{mn} \mathrm{d}x) \tag{1}$$

is the amplitude function of the mode $(m\omega_0, n\beta_0)$ (referred to as (m,n)), where β_0 denotes the fundamental spanwise wavenumber, ω_0 the fundamental frequency and α is the complex-valued streamwise wavenumber. Further, x and y are the streamwise and wall-normal coordinates, respectively. The evolution of each mode is described by the nonlinear PSE as given *e.g.* Bertolotti *et al.* (1992). In addition, we use a scaling proposed by Ori & Henningson (2003) to modify the PSE to correctly describe the evolution of streaks. These equations are then discretized using a fourth-order compact scheme for the wall-normal derivatives and first- or second-order backward Euler for the streamwise derivatives. It is well known that original PSE suffer from numerical instability for small streamwise step-size. Here, we use the technique proposed by Andersson *et al.* (1998) to stabilize the numerical integration. As initial condition for the streak, we use optimal disturbances (Andersson *et al.* 1999) at the leading edge, which in a linear framework lead to the maximum perturbation energy at a certain downstream position. These are computed with a spectral code

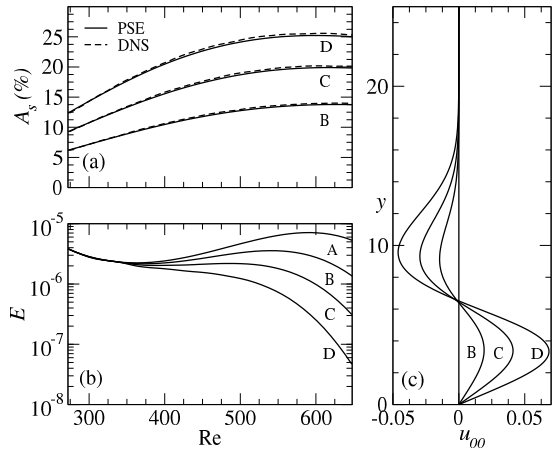

FIGURE 1. (a) Comparison of DNS and PSE simulations of the non-linear downstream development of three streaks with increasing amplitudes. (b) The evolution of the TS-wave in presence of streaks. (c) The mean-flow distortion at $\mathrm{Re} = 640$ caused by streaks.

used in Ori & Henningson (2003) based on an adjoint optimization technique described in Andersson *et al.* (1999).

The procedure of the simulations is as follows. An optimal disturbance is initiated close to the leading edge. Its linear downstream development is followed up to a specified streamwise position, where the nonlinear calculations begin by the assignment of an initial amplitude, defined as

$$A_s = \frac{1}{2}\left(\max_{y,z}\{u_s\} - \min_{y,z}\{u_s\}\right).$$

Here, u_s is the sum of the streamwise velocity component of all $(0, n)$-modes. At this location, a single exponential disturbance is initialized, (m, n)-mode, with an amplitude sufficiently low to insure its linear behavior. Unless otherwise stated, this location is upstream of the first neutral point of the exponential disturbances at $\mathrm{Re}_0 = \sqrt{x_0 U_e/\nu} = 250$, where U_e is the streamwise velocity at the edge of the boundary layer and ν the kinematic viscosity. The length scale used here is $\sqrt{\nu x_0/U_e}$. Usually, $20-30$ modes were sufficient to correctly describe the evolution of the disturbances.

3. Results

3.1. *Validation*

The results obtained using the procedure described above, is verified against the direct numerical simulations of Cossu & Brandt (2002). As in Cossu & Brandt (2002), we consider the instability of a TS-wave of frequency $F =$

$(\omega_0/\mathrm{Re}) \times 10^6 = 131.6$ in the presence of a set of streaks ($\beta_0/\mathrm{Re} = 6.36E-4$) with different amplitudes (figure 1a). The initial profiles of the streaks are optimized for maximum growth at Re = 707 and the nonlinear calculations begin at $\mathrm{Re}_0 = 272$. As reported in Cossu & Brandt (2002) and shown in figure 1b, the stabilizing effect on the TS-wave is observed for all streak amplitudes. Here, the following norm of the disturbance

$$E = \left(\int_0^\infty \mathbf{u} \cdot \mathbf{u}^* \, dy \right)^{1/2},$$

is used as a measure of the TS-wave size. In figure 1b, case A corresponds to zero streak amplitude. For moderate streak amplitudes (B,C) a damping of the growth of the TS-wave is observed, whereas for a sufficiently large streak amplitude (D) the TS-wave is completely stabilized. In figure 1c, the mean-flow distortion u_{00}, *i.e.* streamwise velocity component of the $(0,0)$-mode, is shown. This is induced by streaks and it modifies the velocity profile into a "fuller" shape close to the wall. This seems to be the main mechanism behind the stabilization effect of the streaks (Cossu & Brandt 2002).

3.2. *Effects of the spanwise wavenumber of the streak*

Previous studies (Cossu & Brandt 2002; Fransson *et al.* 2005, 2006) have solely been focusing on the effects of the streak amplitude. As the development of streaks also depends on its spanwise wavelength, it is of interest to investigate its effects on TS-wave instability. Therefore, we vary the spanwise wavenumber of streaks in the range $[0.1, 1]$. The initial profiles of these streaks are optimized for maximum growth at Re = 400. Assigning the same initial amplitude for each of them results in streaks with different maximum amplitudes. Since the stabilizing effect depends strongly on the streak amplitude, it is difficult to draw a definite conclusion about the significance of different values of β. Therefore, it seems reasonable to compare streaks with different β but same maximum amplitude. Here, for each streak we choose an appropriate initial amplitude such that the *maximum* amplitudes, A_s^*, of each of them is 10% of the free-stream velocity. To illustrate the effect of streak parameter β, we begin by investigating the stability of a two-dimensional TS-wave with frequency $F = 131.6$ in the presence of the two streaks shown in figure 2a. The streaks, A and B, have the spanwise wavenumbers, $\beta_A = 0.45$ and $\beta_B = 0.65$ respectively and fixed maximum amplitude, $A_s^* = 10\%$. In figure 2b, we show that in the absence of streaks the TS-wave (dotted line) grows exponentially (with a rate predicted by the linear theory) as it enters the unstable domain at branch I, the shaded domain, and decays as it is propagated downstream away from the domain. In the presence of streaks a damping effect is observed, which is larger for streak B (dashed line) than for streak A (solid line), despite the fact that streak A maintains a *larger* amplitude in the most part of the unstable domain of the TS-wave. Streak B, on the other hand, attains its maximum amplitude close to the location of branch I of the TS-wave, and then rapidly decays downstream. This can be explained if the distortion of the mean flow,

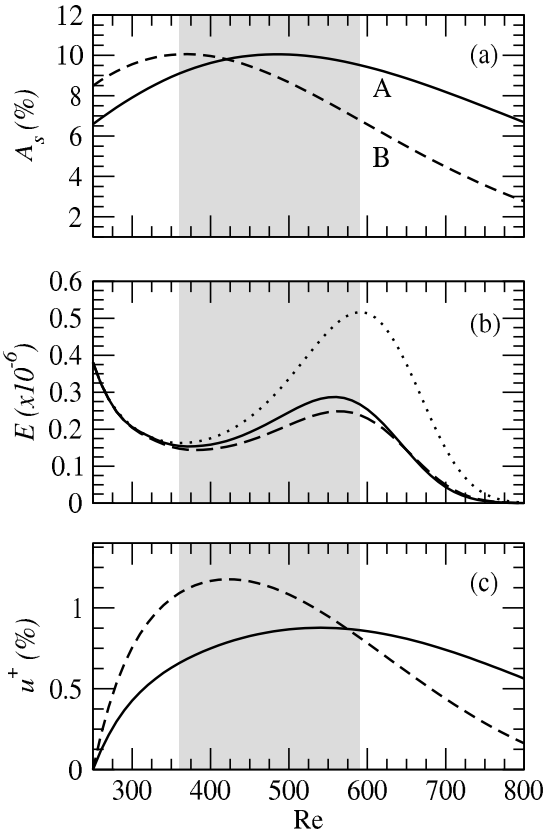

FIGURE 2. (a) Evolution of amplitudes of two streaks with $\beta = 0.45$ (solid) and $\beta = 0.65$ (dashed). (b) TS wave with $F = 131.6$ in absence (dotted) and presence (dashed,solid) of streaks. (c) The maximum value of the mean flow distortion caused by the streaks.

$(0, 0)$-mode, induced by these two streaks are compared. In figure 2c, the development of the maximum mean-flow distortion, *i.e.* $u^+ = \max_y\{u_{00}\}$, for streaks A and B is shown. It is apparent that streak B modifies the flow considerably more than streak A, between branch I and II, due to larger values of u^+. This is caused by the larger amplitude of streak B upstream of branch I.

As a measure of the amplification of the TS-waves, we compute the N-factor, defined as

$$N(x) = \ln(E(x)/E(x_I)).$$

In figure 3a, $N(x_{II})$ for the TS-wave with $F = 131.6$ is plotted as a function of the spanwise wavenumber of the streaks, β. Here the maximum streak amplitudes are kept constant, $A_s^* = 10\%$. As shown in figure 3a, $N(x_{II})$ attains

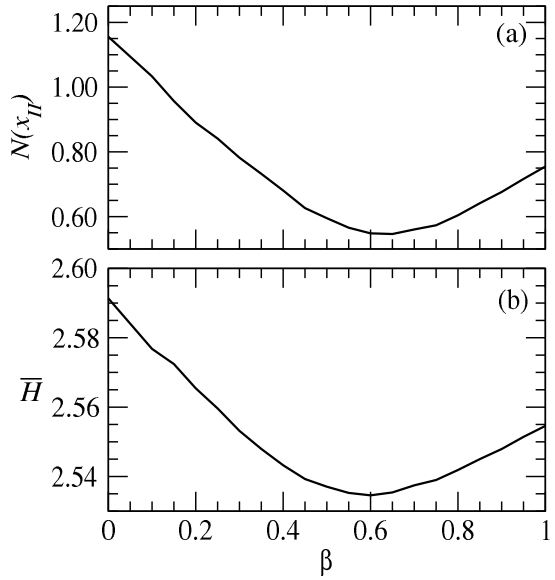

FIGURE 3. (a) The N-factor at branch II of the TS-wave ($F = 131.6$) as a function of the spanwise wavenumber of streaks. The maximum amplitudes of the streaks have been fixed at $A_s^* = 10\%$. (b) The averaged shape factor $\bar{H}$ as a function of the same set of streaks as in (a).

a minimum value for $\beta \approx 0.65$. This indicates that there exists an optimal streaky boundary layer, when the objective is to minimize the amplification of the TS-wave. It should be mentioned that, due to nonlinear effects, there is a slight upstream shift of the location of the A_s^* with increasing initial streak amplitude (see figure 1a). Therefore, the "optimal" β depends weakly on the streak amplitude. In order to relate the total modification of the mean flow caused by streaks, to their stabilization effects we compare the N-factor with the averaged shape factor $\bar{H}$. Here, $\bar{H}$ is averaged in the streamwise direction between branch I and II of the TS-wave. In figure 3b, $\bar{H}$ is plotted as a function of β. In the absence of streaks, the shape factor of a Blasuis profile is $\bar{H} = 2.59$, whereas in the presence of streaks $\bar{H}$ is smaller, indicating a fuller velocity profile. Furthermore, $\bar{H}$ attains a minimum value in the presence of streaks with $\beta = 0.6$, *i.e.* close to the β which minimizes the N-factor of the TS-wave (shown in figure 3a). This indicates that the commonly used streak with $\beta = 0.45$ is not the most efficient stabilizing streak. This value of β corresponds to the vortices generated at the leading edge which experience the largest linear growth (Andersson *et al.* 1999). We have performed the same parametric study of β for two other frequencies, $F = 170$ and 90. For both frequencies the N-factor, $N(x_{II})$, attains a minimum at approximately the spanwise wavenumber (0.9 and 0.45 respectively), for which the streamwise averaged shape-factor is

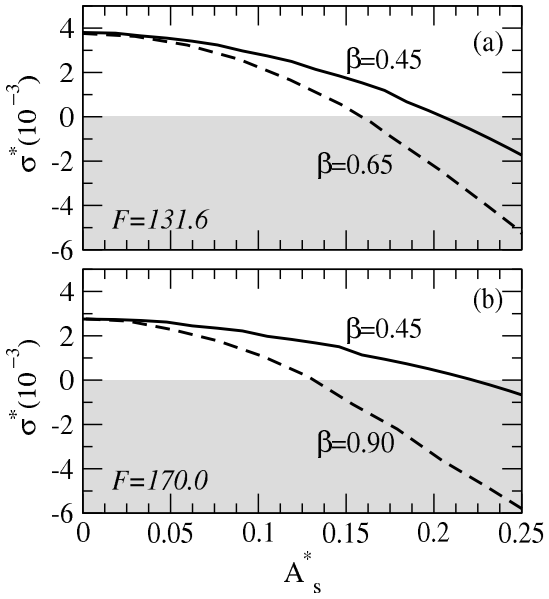

FIGURE 4. The maximum growth rate σ^* of TS-waves, $F = 131.6$ in (a) and $F = 170$ in (b), in the presence of streaks.

the smallest. Again, the streak which is the most efficient for stabilizing a TS-wave attains its maximum amplitude close to branch I of that TS-wave.

Now we aim at finding the minimum streak amplitude necessary for the complete stabilization of a TS-wave. We consider two different streaks: the optimal growing streak ($\beta = 0.45$) and a streak with $\beta = 0.65$, chosen such that the maximum streak amplitudes are close to branch I of the given TS wave. The maximum amplitudes are varied between $0-25\%$ and the maximum growth rates $\sigma^* = \max_x\{\sigma\}$ of the TS-wave are computed for each streak. The physical growth rates are calculated from the relation (Bertolotti *et al.* 1992) $\sigma = -\alpha_i + \frac{\partial}{\partial x}\ln(E)$. When $\sigma^* < 0$ the TS-wave is completely stabilized. For complete stabilization of a TS-wave with $F = 131.6$, the necessary amplitude of the streak with $\beta = 0.65$ is $A_s = 15\%$, whereas for $\beta = 0.45$ the corresponding amplitude is $A_s = 20\%$, see figure 4a. For $F = 170$, the necessary amplitude is reduced from $A_s = 22\%$ to $A_s = 0.12\%$, when β is increased from 0.45 to 0.9, see figure 4b. As the TS-wave frequency is decreased, the location of the branch I moves downstream and consequently streaks with smaller β are required to stabilize the flow.

3.3. *Stabilization of oblique waves*

The focus of previous investigations (Cossu & Brandt 2002; Fransson *et al.* 2005) has been on reducing the linear growth of two-dimensional TS-waves,

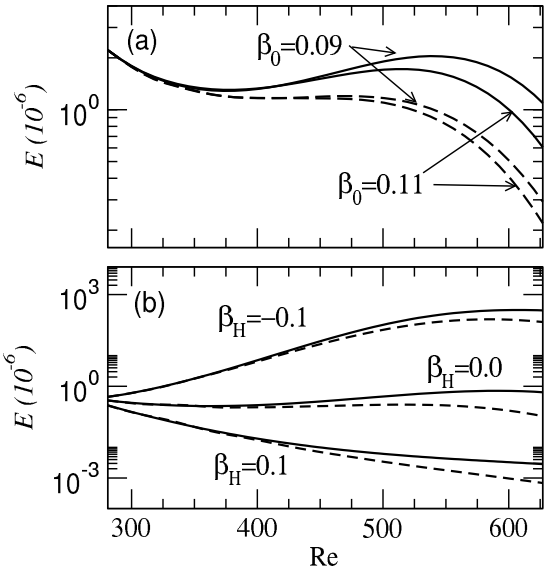

FIGURE 5. (a) The downstream development of oblique waves ($F = 131.6$) in the absence (solid) and the presence (dashed) of streaks. (b) The downstream development of a TS-wave ($F = 131.6$) in the absence (solid) and the presence (dashed) of streaks in boundary layer with adverse, zero and favorable pressure gradient.

as these disturbances are the first to become unstable in a Blasius boundary-layer. However, certain transition scenarios (Bertolotti *et al.* 1992), require the existence of oblique waves. Here, we choose two unstable oblique waves with frequency $F = 131.6$ and spanwise wavenumbers $\beta_0 = 0.09$ and 0.1123, respectively. For these values of β_0, a streak with a spanwise wavenumber $\beta = 0.45$ is initiated at $\mathrm{Re}_0 = 272$ as modes $(0, 5\beta_0)$ and $(0, 4\beta_0)$, respectively. The oblique disturbances are initiated as a pair of modes $(1, \pm 1)$ with sufficiently small amplitude to insure a linear behavior. The results are shown in figure 5a, where we compare the norm E of the oblique waves in the presence (dashed line) and the absence (solid line) of a streak with the maximum amplitude $A_s^* = 10\%$. Similar to TS-waves, the linear growth of the oblique waves is found to be damped when streaks are present.

3.4. *Effects of pressure gradient*

We have also investigated the effects of streaks on the linear growth of exponential disturbances in boundary-layer flows with pressure gradients. In particular, boundary layers with the free-stream velocities given as $U_e = U_\infty x^m$, $m = \beta_H/(2 - \beta_H)$, where β_H is the Hartree parameter. In figure 5b, the evolution of a TS-wave with frequency $F = 131.6$ in boundary layers with favorable

($\beta_H = 0.1$), zero ($\beta_H = 0$) and adverse pressure ($\beta_H = -0.1$) gradients are shown by the solid lines. By introducing a streak at $\mathrm{Re}_0 = 278$ with spanwise wavenumber $\beta = 0.45$ and amplitudes $A_s \approx 13 - 16\%$, the growth of TS-waves is damped (shown by dashed lines).

4. Conclusions

We have found that the stabilization effect of streaks on the linear growth of TS-waves in Blasius boundary layer, observed in previous studies, to also apply to three dimensional disturbances and Falkner-Skan boundary-layer flows. We have also found that by distributing the streaks "optimally" in the spanwise direction, it is possible to completely stabilize a TS-wave, with considerably lower streak amplitudes. For the TS-waves with high frequencies a reduction of the maximum streak amplitude of almost a factor two can be achieved. The streaks which most efficiently reduce the growth rate of a given disturbance attain their maximum amplitudes close to the branch I of that disturbance. These streaks generate a "fuller" velocity profile in the unstable domain of the TS-waves. By computing the streamwise averaged shape factor of the modified boundary layer, one can estimate the stabilization effect of streaks without actually calculating the interaction with the targeted TS (or oblique) waves. It should also be mentioned that the optimal growing streak, often associated with the spanwise wavenumber $\beta = 0.45$, is not the most efficient one to suppress TS-waves of all frequencies.

Acknowledgements

We wish to thank Luca Brandt, Carlo Cossu, Phillip Schlatter and Dan Henningson for their helpful comments.

References

Andersson, P., Berggren, M., andHenningson, D.S. 1999 Optimal disturbances and bypass transition in boundary layers. *Phys. Fluids* **11**, 134–150.

Andersson, P., Henningson, D.S. and Hanifi, A. 1998 On a stabilization procedure for the parabolic stability equations. *J. Eng. Math.* **33**, 311–332.

Bertolotti, F.P., Herbert, Th., and Spalart, P.R. 1992 Linear and nonlinear stability of the Blasius boundary layer. *J. Fluid Mech.* **242**, 441–474.

Boiko, A.V., Westin, K.J.A., Klingmann, B.G.B., Kozlov, V.V. and Alfredsson, P.H. 1994 Experiments in a boundary layer subjected to free stream turbulence. Part 2. The role of TS-waves in the transition process. *J. Fluid Mech.* **281**, 219–245.

Choi, K. 2006 The rough with the smooth. *Nature* **440**, 754.

Cossu C. and Brandt L. 2002 Stabilization of Tollmien-Schlichting waves by finite amplitude optimal streaks in the Blasius boundary layer. *Phys. Fluids* **14**, L57.

Fransson J.H.M., Brandt, L., Talamelli, A. and Cossu, C. 2005 Experimental study of the stabilization of Tollmien-Schlichting waves by finite amplitude streaks. *Phys. Fluids* **17**, 054110.

Fransson, J.H.M, Talamelli, A., Brandt, L. and Cossu, C. 2006 Delaying transition to turbulence by a passive mechanism. *Phys. Rev. Lett.* **96**, 064501.

Levin, O. and Henningson, D.S. 2003 Exponential vs algebraic growth and transition prediction in boundary layer flow. *Flow, Turbulence Combust* **70**, 183-210a.

Saric, W.S., Carillo R.B. Jr. and Reibert, M.S. 1998 Leading-edge roughness as a transition control mechanism. *AIAA Paper* **98**, 0781.